

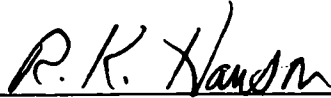
SHOCK-INDUCED COMBUSTION IN HIGH-SPEED WEDGE FLOWS

**A DISSERTATION
SUBMITTED TO THE DEPARTMENT OF MECHANICAL ENGINEERING
AND THE COMMITTEE ON GRADUATE STUDIES
OF STANFORD UNIVERSITY
IN PARTIAL FULFILLMENT OF THE REQUIREMENTS
FOR THE DEGREE OF
DOCTOR OF PHILOSOPHY**

**Christopher I. Morris
December 2001**

**© Copyright 2002 by Christopher I. Morris
All Rights Reserved**

I certify that I have read this dissertation and that in my opinion it is fully adequate, in scope and quality, as a dissertation for the degree of Doctor of Philosophy.



R. K. Hanson
(Principal Adviser)

I certify that I have read this dissertation and that in my opinion it is fully adequate, in scope and quality, as a dissertation for the degree of Doctor of Philosophy.



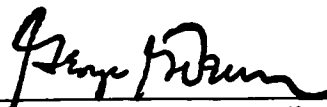
C. T. Bowman

I certify that I have read this dissertation and that in my opinion it is fully adequate, in scope and quality, as a dissertation for the degree of Doctor of Philosophy.



M. G. Mungal

Approved for the University Committee on Graduate Studies:



Dean of Graduate Studies

Abstract

Interest in shock-induced combustion has been revived in recent years due to the ongoing development of high-speed propulsion systems, such as SCRAMjets and ram accelerators. Oblique detonation waves (ODWs), which are essentially oblique shocks closely followed by a combustion front, have been proposed as a means of rapidly converting latent chemical energy into thrust for these applications. While the theory governing oblique detonation waves in the limit of very fast chemistry is relatively well understood, there is a comparative lack of understanding of ODW formation under non-equilibrium conditions. The purpose of this study is to improve understanding of these phenomena through modern experimental and numerical modeling methods. The computational results were generated by a dedicated multi-species, finite-rate chemistry CFD code developed by the author. In order to develop an appreciation for the accuracy of the model, the numerical results were compared to OH PLIF and schlieren imaging results obtained in the Stanford expansion tube facility.

Rankine-Hugoniot and shock polar theory clearly describes a number of flow regimes based on the frozen- and equilibrium-chemistry polar curves, and the wedge turning angle. Within one range of turning angles, solutions on both the frozen and equilibrium polars are possible. Within this regime, an actual supersonic, exothermic wedge flow will typically involve an initial frozen oblique shock attached to the tip of the wedge, which transitions to an oblique detonation wave as energy is released by combustion. The numerical model was used to investigate the critical role of the energy-release rate in governing the characteristics of the transition process. A series of 16 test cases was studied using the numerical model, for the same test gas mixture, freestream velocity and temperature throughout, but varying the wedge angle and freestream pressure in order to vary the energy release rate. Predicted characteristic ignition times, τ_{ign} , and equilibration times τ_{equil} , were computed for each case using calculated post shock conditions and constant density CHEMKIN-II calculations. A prediction normalized reaction parameter was also calculated from the ratio of these two timescales ($NRP = \tau_{\text{equil}}/\tau_{\text{ign}}$) for each case. The length of the domain studied in each case was scaled to $5 \times \tau_{\text{ign}}$. To summarize briefly, the results were qualitatively classified into three

categories. One category exhibited a slow, smooth increase in the oblique shock wave angle, but did not achieve the equilibrium detonation wave angle within the domain studied. The characteristic equilibration time in each of these cases was relatively long ($NRP > 1.0$). A second category of results exhibited a smooth transition from oblique shock to an equilibrium oblique detonation wave within the domain. In each case of this regime, the characteristic equilibration time was between roughly one-half to equal to the corresponding ignition time ($0.5 \lesssim NRP \lesssim 1.0$). A third category of results exhibited a rapid acceleration of the reaction front toward the shock, and a consequent discontinuous transition from oblique shock to detonation. The detonation wave initially formed at an angle greater than the equilibrium wave angle in each of these cases, but relaxed to the equilibrium value in the far field. Results in this regime each had an equilibration time significantly smaller than the corresponding ignition time ($NRP < 0.5$). It is important to note that these qualitative classifications held over the range of conditions studied in this work (stoichiometric H_2 -air, ignition times ranging from 0.1 – $10 \mu s$). Extension to a wider range of mixtures and conditions would require additional study.

Another study investigated whether an oblique detonation can be stabilized at wedge angles less than the nominal wedge angle which would generate an oblique Chapman-Jouguet (C-J) detonation. The investigation found that a solution essentially consisting of an oblique C-J detonation, followed by a Prandtl-Meyer expansion wave which turns the flow parallel to the wedge surface, is indeed possible. Finite-rate chemistry leads to significant overlap of the reaction zone and expansion wave in the near-field.

Wedge angles larger than the detachment point on the equilibrium polar result in an initial frozen shock attached to the wedge tip, followed by a locally detached detonation wave. The numerical model was used to investigate whether the detached detonation can remain stabilized on the wedge surface. The results confirmed that, if the energy release rate is sufficient to drive the reaction front into the shock and create a locally detached detonation, the detonation will inevitably propagate forward toward the wedge tip. Comparisons of the numerical model with experimental OH PLIF and schlieren flow visualization results in this regime also show generally good agreement.

Acknowledgments

I would like to acknowledge and thank a few of the people who helped in the completion of this work and contributed to my life at Stanford. Many thanks to my advisor, Professor Hanson, for his substantial patience, encouragement, guidance, and support during this period of my life. Thanks are also due to Professors Bowman, Mungal, and Mitchell for their valuable suggestions to this work. I am especially indebted to Michel Kamel and Adela Ben-Yakar, who worked with me throughout the design, development, and experimental history of the expansion tube facility. Dave Davidson and Frank Levy also provided special help and advice during our work at Stanford.

I would also like to acknowledge my many good friends at Stanford, wonderful people who made life there so personally satisfying: Michel Kamel, Adela Ben-Yakar, Eric Petersen, Ted and Heidi Furlong, Chad Sipperley, Brian Kirby, Emily Pidgeon, Charlie Hasselbrink, Bill Urban, Brian Luehrs, Richard Reitmeyer, Bill Hargus, Alex Glew, Ron Bates, Bob and Stacy Gleixner, Paul Kitabjian, Rick Gessman, and Brian Holloway. Finally, many thanks to my family for their love and encouragement.

Contents

1	Introduction	1
1.1	Motivation	1
1.2	Previous Work	3
1.2.1	Analytical Work	3
1.2.2	Experimental Studies	3
1.2.3	Numerical Studies	5
1.3	Focus of this Study	6
2	Theory of Oblique Shock and Detonation Waves in Wedge Flows	7
2.1	Simplified Rankine-Hugoniot Analysis	7
2.1.1	Flow Geometry	8
2.1.2	Conservation Laws	8
2.1.3	Jump Conditions	9
2.2	Shock Polar Theory	13
2.2.1	Solution Procedure	13
2.2.2	Inert Shock Polar Diagram	13
2.2.3	Exothermic Shock Polar Diagram	14
2.3	Real Thermochemistry Calculations	17
2.3.1	Vibrational Excitation	18
2.3.2	Equilibrium Chemistry Considerations	19
2.3.3	Effect on Hugoniot and Shock Polar Diagrams	22
2.4	Finite-Rate Chemistry and Energy Release Behind a Shock Wave	24
2.4.1	H ₂ -O ₂ Ignition and Energy Release	25
2.4.2	Finite-Rate Chemistry in a 1-D Normal Shock Flow	26
2.4.3	Extension to a Straight Oblique Detonation Wave	29
2.5	Finite-Rate Chemistry in Supersonic Wedge Flow	31

2.5.1	Generalized Description	31
2.5.2	Finite-Rate Chemistry CFD Calculations	34
2.5.3	Example CFD Calculations	36
3	Experimental Apparatus	41
3.1	Expansion Tube Facility	41
3.1.1	Expansion Tube Theory	42
3.1.2	Description of the Facility	44
3.1.3	Nonidealities in Expansion Tubes	47
3.1.4	Calculation of Test Flow Conditions	49
3.1.5	Observed Flow Nonidealities	51
3.2	Optical Diagnostics	53
3.2.1	Description of PLIF Imaging	53
3.2.2	Description of Imaging Set-up	54
4	Study of Oblique Detonation Waves in Wedge Flows	56
4.1	Numerical Study of Oblique Detonation Waves	56
4.1.1	Oblique Detonation Wave Formation when $\theta_{C-J} < \theta < \theta_{det,eq}$	56
4.1.2	Oblique Detonation Wave Formation when $0 < \theta < \theta_{C-J}$	72
4.1.3	Oblique Detonation Wave Formation when $\theta_{det,eq} < \theta < \theta_{det,fr}$	78
4.2	Comparison with Experimental Results	79
5	Conclusions	84
5.1	Summary	84
5.2	Recommendations for Future Work	86
A	Thermodynamic Model	88
B	Chemical Kinetics Mechanism for H₂/O₂ Combustion	93

List of Tables

3.1	Spectral analysis of oscillation phenomena on pitot pressure records. M_{S1} is the measured shock Mach number through the test gas in the driven section. c_2 is the post-shock test gas sound speed. c_3 is the sound speed of the expanded driver gas adjacent to the contact surface. Test gas: 5% CO ₂ + 95% N ₂	53
4.1	Summary of results for the 16 test cases studied. Predicted characteristic times τ_{ign} and τ_{equil} are determined from constant density ignition calculations of CHEMKIN-II using calculated post-shock conditions along the wedge surface. The results are ranked in order of decreasing predicted normalized reaction parameter, $NRP = \tau_{ign}/\tau_{equil}$. Peak shock angle is the peak value within the computational domain. . .	71
A.1	Molecular weight and heat of formation data for species used in this work (McBride et al., 1993).	89
A.2	Curve fit parameters for thermodynamic model of N ₂ , O ₂ , and H ₂ (McBride et al., 1993).	90
A.3	Curve fit parameters for thermodynamic model of OH, H ₂ O, and H (McBride et al., 1993).	91
A.4	Curve fit parameters for thermodynamic model of O, HO ₂ , and H ₂ O ₂ (McBride et al., 1993).	92
B.1	Chemical kinetics mechanism for H ₂ /O ₂ combustion, from Petersen and Hanson (1999). Species are N ₂ , O ₂ , H ₂ , H ₂ O, OH, H, O, HO ₂ , H ₂ O ₂ . All reactions are reversible. Except where noted, rate coefficients are computed via the Arrhenius expression: $k(T) = AT^n \exp(-E/RT)$. Units are in cal, mol, cm ³ , and s.	94

List of Figures

1.1	Oblique detonation wave engines (a) may have attractive advantages compared to SCRAMjet engines. Ram accelerators (b) utilize an oblique detonation wave stabilized on the projectile to provide thrust in the superdetonative regime ($V_{\text{projectile}} > V_{C-J}$)	2
1.2	Experimental data on oblique detonation waves and shock-induced combustion have been obtained by 3 methods: (a) direct projectile firings into a combustible gas mixture, (b) the two-layer, “oblique shock tube” experiment, (c) accelerating a flow of combustible gas over a fixed model.	4
2.1	Schematic of an attached oblique shock or detonation in supersonic flow around a wedge of angle θ . Normal and tangential velocity components before and after the shock wave are shown in the figure.	8
2.2	Rankine-Hugoniot diagram showing solutions for an inert shock ($\tilde{Q} = 0$), and for a shock with instantaneous energy release ($\tilde{Q} = 4.8$). A Rayleigh line corresponding to the Chapman-Jouguet velocity is shown.	10
2.3	Rankine-Hugoniot diagram showing solutions for an inert shock ($\tilde{Q} = 0$), and for a shock with instantaneous energy release ($\tilde{Q} = 4.8$). Rayleigh lines corresponding to both sub-detonative ($M_{1n} < M_{C-J}$) and super-detonative ($M_{1n} > M_{C-J}$) flow conditions are shown.	12
2.4	Example shock polar diagram for an inert gas with no energy release ($\tilde{Q} = 0$) at a fixed freestream Mach number ($M_1 = 8$) and specific heat ratio ($\gamma = 1.4$). Case (a): attached shock wave (SW) solutions possible for $\theta < \theta_{\text{det},0}$. Case (b): shock wave detaches when $\theta > \theta_{\text{det},0}$	15

2.5	<p>Example shock polar diagram showing solutions for both an inert gas (blue curve, $\tilde{Q} = 0$) and a gas with instantaneous energy release across the shock (red curve, $\tilde{Q} = 4.8$). Specific heat ratio and freestream Mach number are fixed ($\gamma = 1.4$, $M_1 = 8$). Case (a): hypothetical C-J oblique detonation wave followed by Prandtl-Meyer expansion fan for $0 < \theta < \theta_{C-J}$. Case (b): attached oblique detonation wave solution possible for $\theta_{C-J} < \theta < \theta_{det,q}$. Case (c): detonation detaches when $\theta_{det,q} < \theta < \theta_{det,0}$.</p>	16
2.6	<p>Example plot showing effect of freestream Mach number on the maximum ($\theta_{det,q}$) and minimum (θ_{C-J}) wedge turning angles which will permit an attached exothermic shock solution. Specific heat ratio and energy release are fixed ($\gamma = 1.4$, $\tilde{Q} = 4.8$)</p>	17
2.7	<p>Example plots showing effect of shock strength on equilibrium radical populations and temperature in shock-induced combustion. Upper panel: species mole fraction at equilibrium. Lower panel: corresponding post-shock temperature increase, $\Delta T = T_{2,eq} - T_{2,fr}$. Gas mixture: stoichiometric H₂-air (2 H₂ + O₂ + 3.76 N₂). $T_1 = 280$ K, $P_1 = 1.0$ atm.</p>	20
2.8	<p>Example plots showing effect of pressure on equilibrium radical populations and temperature in shock-induced combustion. Upper panel: species mole fraction at equilibrium. Lower panel: corresponding post-shock temperature increase, $\Delta T = T_{2,eq} - T_{2,fr}$. Gas mixture: stoichiometric H₂-air (2 H₂ + O₂ + 3.76 N₂). $T_1 = 280$ K, $V_{1n} = 2500$ m/s.</p>	21
2.9	<p>Example Rankine-Hugoniot diagram showing solutions for a frozen-chemistry shock, and for a shock with instantaneous equilibrium chemistry. Gas mixture: stoichiometric H₂-air (2 H₂ + O₂ + 3.76 N₂). $T_1 = 280$ K, $P_1 = 1.0$ atm. For comparison, equivalent constant-γ ($\gamma = 1.4$), and constant-\tilde{Q} ($\tilde{Q} = 0$ and $\tilde{Q} = 4.8$) curves are shown as dashed lines. $M_{C-J} = 5$ in both cases.</p>	22
2.10	<p>Example shock polar diagram showing solutions for a frozen-chemistry shock, and for a shock with instantaneous equilibrium chemistry. Gas mixture: stoichiometric H₂-air (2 H₂ + O₂ + 3.76 N₂). $T_1 = 280$ K, $P_1 = 1.0$ atm, $M_1 = 8$. For comparison, equivalent constant-γ ($\gamma = 1.4$), and constant-\tilde{Q} ($\tilde{Q} = 0$ and $\tilde{Q} = 4.8$) curves are shown as dashed lines. $M_{C-J} = 5$ in both cases.</p>	24

2.11	Example plot showing effect of freestream Mach number on the maximum ($\theta_{det,q}$) and minimum (θ_{C-J}) wedge turning angles which will permit an attached exothermic shock solution. Gas mixture: stoichiometric H ₂ -air (2 H ₂ + O ₂ + 3.76 N ₂). $T_1 = 280$ K, $P_1 = 1.0$ atm. For comparison, equivalent constant- γ ($\gamma = 1.4$), and constant- \bar{Q} ($\bar{Q} = 0$ and $\bar{Q} = 4.8$) curves are shown as dashed lines.	25
2.12	Example plots showing species (upper panel) and temperature (lower panel) history for the constant-volume ignition of stoichiometric H ₂ -air (2 H ₂ + O ₂ + 3.76 N ₂). Initial conditions: $T_{ini} = 1500$ K, $P_{ini} = 1.0$ atm. τ_{ign} defined as point (from $\tau = 0$) when $\Delta T = 0.01 \Delta T_{tot}$. τ_{equil} defined as point (from $\tau = \tau_{ign}$) when $\Delta T = 0.99 \Delta T_{tot}$	27
2.13	Schematic of 1-D reaction zone structure in a normal detonation wave.	28
2.14	Computed 1-D reaction zone structure in a normal C-J detonation wave. Gas mixture: stoichiometric H ₂ -air (2 H ₂ + O ₂ + 3.76 N ₂). $T_1 = 280$ K, $P_1 = 1.0$ atm, $u_1 = 1980$ m/s.	28
2.15	Example Rankine-Hugoniot diagram showing solutions for a frozen-chemistry shock, and for a shock with instantaneous equilibrium chemistry. Reaction zone points are computed for a 1-D C-J detonation wave. Time scale referenced on the diagram is particle time from passage through the shock. Gas mixture: stoichiometric H ₂ -air (2 H ₂ + O ₂ + 3.76 N ₂). $T_1 = 280$ K, $P_1 = 1.0$ atm.	30
2.16	Schematic of ZND reaction zone structure in a straight oblique detonation wave. . .	31
2.17	Example shock polar diagram showing solutions for a frozen-chemistry shock, and for a shock with instantaneous equilibrium chemistry. Reaction zone points are computed for a 1-D C-J oblique detonation wave at an angle of $\beta = 38.8^\circ$. Time scale referenced on the diagram is particle time from passage through the shock. Gas mixture: stoichiometric H ₂ -air (2 H ₂ + O ₂ + 3.76 N ₂). $T_1 = 280$ K, $P_1 = 1.0$ atm, $M_1 = 8$	32
2.18	Generalized description of possibilities for supersonic wedge flow with a combustible gas mixture. Note: Freestream Mach number $M_1 > M_{C-J}$, Wedge angle θ limited by $\theta_{C-J} < \theta < \theta_{det,eq}$. (a) Oblique shock (fr. solution), no reaction front (b) Oblique shock (fr. solution) followed by reaction front, transition to oblique detonation (eq. solution) (c) Oblique detonation (eq. solution)	33
2.19	(a) Schematic of computational grid aligned with the wedge surface. (b) Schematic of boundary conditions of the computational grid.	34

2.20	Converged CFD simulation of stoichiometric H ₂ -air (2 H ₂ + O ₂ + 3.76 N ₂) flow over a $\theta = 35^\circ$ wedge. $T_1 = 280$ K, $P_1 = 0.125$ atm, $M_1 = 8$. $\Delta x = 0.01$ mm, $\Delta y = 0.005$ mm. Upper panel: temperature contour plot. Lower panel: corresponding plot of shock wave angle as a function of grid x-coordinate.	36
2.21	Converged CFD simulation of stoichiometric H ₂ -air (2 H ₂ + O ₂ + 3.76 N ₂) flow over a $\theta = 35^\circ$ wedge. $T_1 = 280$ K, $P_1 = 0.125$ atm, $M_1 = 8$. $\Delta x = 0.03$ mm, $\Delta y = 0.015$ mm. Upper panel: temperature contour plot. Lower panel: corresponding plot of shock wave angle as a function of grid x-coordinate.	37
2.22	Converged CFD simulation of stoichiometric H ₂ -air (2 H ₂ + O ₂ + 3.76 N ₂) flow over a $\theta = 35^\circ$ wedge. $T_1 = 280$ K, $P_1 = 0.5$ atm, $M_1 = 8$. $\Delta x = 0.01$ mm, $\Delta y = 0.005$ mm. Upper panel: temperature contour plot. Lower panel: corresponding plot of shock wave angle as a function of grid x-coordinate.	38
2.23	Converged CFD simulation of stoichiometric H ₂ -air (2 H ₂ + O ₂ + 3.76 N ₂) flow over a $\theta = 35^\circ$ wedge. $T_1 = 280$ K, $P_1 = 0.125$ atm, $M_1 = 8$. $\Delta x = 0.1$ mm, $\Delta y = 0.05$ mm. Upper panel: temperature contour plot. Lower panel: corresponding plot of shock wave angle as a function of grid x-coordinate.	39
2.24	Converged CFD simulation of stoichiometric H ₂ -air (2 H ₂ + O ₂ + 3.76 N ₂) flow over a $\theta = 35^\circ$ wedge. $T_1 = 280$ K, $P_1 = 0.5$ atm, $M_1 = 8$. $\Delta x = 0.03$ mm, $\Delta y = 0.015$ mm. Upper panel: temperature contour plot. Lower panel: corresponding plot of shock wave angle as a function of grid x-coordinate.	40
3.1	X-t wave diagram and schematic of an expansion tube. Gas states are summarized as follows: 1 = initial condition of test gas in driven section, 4 = initial condition of driver gas, 3 = expanded driver gas, 2 = post-shock condition of the test gas, 5 = expanded test gas, 10 = initial condition of acceleration gas in expansion section, 20 = post-shock condition of acceleration gas.	42
3.2	Schematic of expansion tube facility and optical arrangement used for simultaneous OH PLIF and schlieren imaging of reactive flows.	45
3.3	Schematic of flow behind the shock wave in the expansion section. 10 = initial condition of acceleration gas in expansion section, 20s = immediate post-shock condition of acceleration gas, 20c = condition of acceleration gas near the contact surface, 5 = expanded test gas.	47
3.4	Example wall pressure and IR absorption records at $x = 102$ cm upstream from exit plane of the expansion tube. Test gas: 5% CO ₂ + 95% N ₂ . $P_{10} = 5.00$ mm Hg helium. $M_{\text{shock}} = 2.85$	50

3.5	Example pitot pressure record from $x = 2$ cm downstream of the exit plane of the expansion tube. Test gas: 5% CO ₂ + 95% N ₂ . $P_{10} = 5.00$ mm Hg helium. $M_{\text{shock}} = 2.85$	50
3.6	Comparison of measured helium flow-time data with viscid and inviscid predictions using measured expansion section shock speed. (a) Wall static pressure/IR absorption method at $x = 102$ cm upstream from exit plane of the expansion tube. (b) Pitot pressure method at $x = 2$ cm downstream of the exit plane of the expansion tube. Laminar boundary layer assumed for viscous correction. Test gas: 5% CO ₂ + 95% N ₂ . $P_{10} = 5.00$ mm Hg helium.	52
4.1	Example shock polar diagram showing solutions for a frozen shock, and for a shock with instantaneous equilibrium chemistry. Gas Mixture: H ₂ -air (2 H ₂ + O ₂ + 3.76 N ₂). $T_1 = 1000$ K, $P_1 = 1.0$ atm, $V_1 = 2500$ m/s.	57
4.2	Converged CFD simulation of stoichiometric H ₂ -air (2 H ₂ + O ₂ + 3.76 N ₂) flow over a $\theta = 40^\circ$ wedge. $T_1 = 280$ K, $P_1 = 0.1$ atm, $M_1 = 8$. $\Delta x = 0.02$ mm, $\Delta y = 0.01$ mm. Upper panel: temperature contour plot. Middle Panel: OH mole fraction contour plot. Lower panel: corresponding plot of shock wave angle as a function of grid x-coordinate.	60
4.3	Plots comparing the local shock wave angle (upper panel) to the ignition length behind the shock (lower panel), as a function of grid Y-coordinate. The CFD calculation is based on the same test conditions as Fig. 4.2 (stoichiometric H ₂ -air flow over a $\theta = 40^\circ$ wedge, $T_1 = 280$ K, $P_1 = 0.1$ atm, $M_1 = 8$).	61
4.4	Examination of two different subdomains of the flowfield at different grid resolutions: (a) the induction zone along the wedge surface, (b) the induction zone near the right boundary of the domain. Contours of OH mole fraction are shown, with the low- and high-temperature boundaries of the oblique shock shown via dashed lines. The CFD calculations are for the same test conditions as Fig. 4.2 (stoichiometric H ₂ -air flow over a $\theta = 40^\circ$ wedge, $T_1 = 280$ K, $P_1 = 0.1$ atm, $M_1 = 8$)	62
4.5	Converged CFD simulation of stoichiometric H ₂ -air (2 H ₂ + O ₂ + 3.76 N ₂) flow over a $\theta = 35^\circ$ wedge. $T_1 = 280$ K, $P_1 = 0.2$ atm, $M_1 = 8$. $\Delta x = 0.028$ mm, $\Delta y = 0.014$ mm. Upper panel: temperature contour plot. Middle Panel: OH mole fraction contour plot. Lower panel: corresponding plot of shock wave angle as a function of grid x-coordinate.	63

4.6	Examination of two different subdomains of the flowfield at different grid resolutions: (a) the induction zone along the wedge surface, (b) the induction zone near the right boundary of the domain. Contours of OH mole fraction are shown, with the low- and high-temperature boundaries of the oblique shock shown via dashed lines. The CFD calculations are based on the same test conditions as Fig. 4.5 (stoichiometric H ₂ -air flow over a $\theta = 35^\circ$ wedge, $T_1 = 280$ K, $P_1 = 0.2$ atm, $M_1 = 8$)	64
4.7	Converged CFD simulation of stoichiometric H ₂ -air (2 H ₂ + O ₂ + 3.76 N ₂) flow over a $\theta = 30^\circ$ wedge. $T_1 = 280$ K, $P_1 = 0.5$ atm, $M_1 = 8$. $\Delta x = 0.046$ mm, $\Delta y = 0.023$ mm. Upper panel: temperature contour plot. Middle Panel: OH mole fraction contour plot. Lower panel: corresponding plot of shock wave angle as a function of grid x-coordinate.	66
4.8	Examination of two different subdomains of the flowfield at different grid resolutions: (a) the induction zone along the wedge surface, (b) the induction zone near the right boundary of the domain. Contours of OH mole fraction are shown, with the low- and high-temperature boundaries of the oblique shock shown via dashed lines. The CFD calculations are based on the same test conditions as Fig. 4.7 (stoichiometric H ₂ -air flow over a $\theta = 30^\circ$ wedge, $T_1 = 280$ K, $P_1 = 0.5$ atm, $M_1 = 8$)	67
4.9	Pressure characteristics of third example case. Upper panel: pressure contour plot. Lower panel: Static pressure distribution as a function of grid x-coordinate at fixed $Y = 0.005$ mm (wedge surface) and $Y = 0.395$ mm. The CFD calculation is based on the same test conditions as Fig. 4.7 (stoichiometric H ₂ -air flow over a $\theta = 30^\circ$ wedge, $T_1 = 280$ K, $P_1 = 0.5$ atm, $M_1 = 8$), though the grid resolution is greater: $\Delta x = 0.02$ mm, $\Delta y = 0.01$ mm.	68
4.10	Results classified on a diagram comparing characteristic chemical timescales. Predicted characteristic times τ_{ign} and τ_{equil} are determined from constant density ignition calculations of CHEMKIN-II using calculated post-shock conditions along wedge surface. ■ = smooth transition to ODW, $\beta_{peak} < \beta_{eq}$ in domain; ▲ = smooth transition to ODW, $\beta_{peak} = \beta_{eq}$ in domain; ▼ = discontinuous transition to ODW, $\beta_{peak} > \beta_{eq}$ in domain.	70
4.11	Converged CFD simulation of stoichiometric H ₂ -air (2 H ₂ + O ₂ + 3.76 N ₂) flow over a $\theta = 15.03^\circ$ wedge. $T_1 = 1000$ K, $P_1 = 1.0$ atm, $V_1 = 2500$ m/s. Upper panel: temperature contour plot. Lower panel: corresponding plot of shock wave angle as a function of grid x-coordinate.	73

4.12	Converged CFD simulation of stoichiometric H ₂ -air (2 H ₂ + O ₂ + 3.76 N ₂) flow over a $\theta = 15.03^\circ$ wedge. $T_1 = 1000$ K, $P_1 = 1.0$ atm, $V_1 = 2500$ m/s. Upper panel: pressure contour plot. Lower panel: corresponding plot of pressure distribution as a function of grid x-coordinate at $Y = 15.07$ mm.	74
4.13	Converged CFD simulation of stoichiometric H ₂ -air (2 H ₂ + O ₂ + 3.76 N ₂) flow over a $\theta = 10^\circ$ wedge. $T_1 = 1000$ K, $P_1 = 1.0$ atm, $V_1 = 2500$ m/s. Upper panel: temperature contour plot. Lower panel: corresponding plot of shock wave angle as a function of grid x-coordinate.	75
4.14	Pressure contour plot of a converged CFD simulation of stoichiometric H ₂ -air (2 H ₂ + O ₂ + 3.76 N ₂) flow over a $\theta = 10^\circ$ wedge. $T_1 = 1000$ K, $P_1 = 1.0$ atm, $V_1 = 2500$ m/s.	76
4.15	Plots of flowfield properties as a function of grid x-coordinate at fixed $Y = 48.65$ mm and $Y = 97.65$ mm (from Figs. 4.13 and 4.14). Upper panel: Static pressure distribution. Lower panel: Vertical velocity component distribution	77
4.16	Temperature contour plots depict the time history of H ₂ -air (2 H ₂ + O ₂ + 3.76 N ₂) flow over a $\theta = 40^\circ$ wedge. $T_1 = 300$ K, $P_1 = 0.2$ atm, $V_1 = 2500$ m/s. The detachment point on the equilibrium polar curve for these conditions is $\theta_{det,eq} \simeq 32.6^\circ$	78
4.17	OH PLIF and schlieren images of shock-induced combustion on a 40° wedge for flow condition 1: (a) Overlaid PLIF and schlieren images of case A: 2 H ₂ + 1 O ₂ + 17 N ₂ , $T_1 = 292$ K, $P_1 = 0.12$ atm, $V_1 = 2130$ m/s ($M_1 = 5.85$) (b) Schlieren image of case B: 2 H ₂ + 1 O ₂ + 12 N ₂ , $T_1 = 282$ K, $P_1 = 0.12$ bar, $V_1 = 2130$ m/s ($M_1 = 5.85$) (c) Overlaid PLIF and schlieren images of case B. The total forebody length pictured in the images is 30.5 mm. The location of the pressure transducer is shown in blue. In both cases the two images were acquired nearly simultaneously ($\Delta t < 2 \mu s$).	80
4.18	Comparison of rotated experimental OH PLIF and schlieren imaging results (a) with the numerical model (b). Gas Mixture: 2 H ₂ + 1 O ₂ + 17 N ₂ . Freestream conditions: $P_1 = 0.12$ bar, $T_1 = 292$ K, $V_1 = 2130$ m/s ($M_1 = 5.85$). The OH PLIF result is overlaid on the schlieren image. The two images were acquired nearly simultaneously ($\Delta t < 2 \mu s$). The grey triangle in the upper-right corner of the experimental image blocks out the blank space generated by rotation of the original image.	81

4.19 Comparison of rotated experimental OH PLIF and schlieren imaging results (a) with the numerical model (b). Gas mixture: $2\text{H}_2 + 1\text{O}_2 + 12\text{N}_2$. Freestream conditions: $P_1 = 0.12\text{ bar}$, $T_1 = 282\text{ K}$, $V_1 = 2130\text{ m/s}$ ($M_1 = 5.85$). The OH PLIF result is overlaid on the schlieren image. The two images were acquired nearly simultaneously ($\Delta t < 2\ \mu\text{s}$). The grey triangle in the upper-right corner of the experimental image blocks out the blank space generated by rotation of the original image.

Chapter 1

Introduction

Interest in shock-induced combustion has been revived in recent years due to the ongoing development of high-speed propulsion systems, such as SCRAMjets and ram accelerators (Herzberg et al., 1988). Oblique detonation waves (ODWs), which are essentially oblique shocks closely followed by a combustion front, have been proposed as a means of rapidly converting latent chemical energy into thrust for these applications. However, while the theory governing oblique detonation waves in the limit of very fast chemistry is relatively well understood, there is a comparative lack of understanding of ODW formation under non-equilibrium conditions.

The purpose of this dissertation is to improve knowledge of these phenomena through modern experimental and numerical modeling methods. The study is primarily computational, though the numerical results are compared to experimental data in order to develop an appreciation for the accuracy of the model. The computational results are generated by a dedicated multi-species, finite-rate chemistry CFD code developed by the author. Experimental flow visualization data consist of OH planar laser-induced fluorescence (PLIF) and schlieren imaging of oblique shock-induced combustion flows in the Stanford expansion tube. This chapter outlines the motivations for this research, and discusses previous work in the field.

1.1 Motivation

Oblique shock-induced combustion and detonation waves have the potential to play a critical role in several future high-speed propulsion applications. One such application is the oblique detonation wave engine (ODWE) concept (Fig. 1.1a). In an ODWE the fuel is injected in the long, slender forebody of the engine and allowed to mix with the air. The combustible fuel/air mixture is then ignited by an oblique shock wave in the combustor. This decoupled approach to mixing and ignition

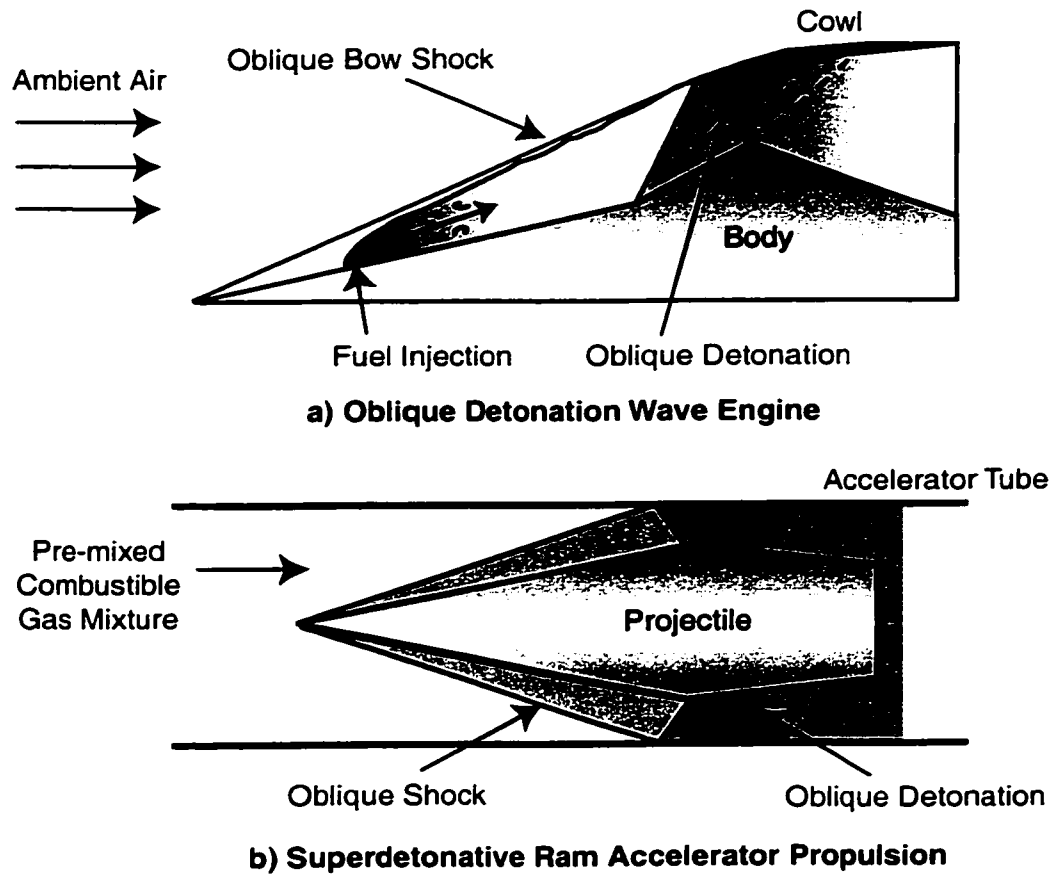


Figure 1.1: Oblique detonation wave engines (a) may have attractive advantages compared to SCRAMjet engines. Ram accelerators (b) utilize an oblique detonation wave stabilized on the projectile to provide thrust in the superdetonative regime ($V_{\text{projectile}} > V_{C-J}$)

is in contrast to the diffusive mixing/burning approach of a SCRAMjet. The potential advantages of the ODWE lie in the reduced inlet angle necessary, the use of the inlet length for fuel/air mixing, and in the shorter combustor length needed due to shock-ignition (Ashford and Emanuel, 1996; Dedebout et al., 1998). These advantages become especially significant at higher flight Mach numbers ($M > 10$).

Ram accelerators (Herzberg et al., 1988), a projectile propulsion strategy under development over the past 15 years, also employ oblique shocks to initiate combustion (Fig. 1.1b). In a ram accelerator, a projectile is injected at supersonic velocity into a long tube filled with a pre-mixed combustible gas mixture. A pattern of shock waves forms around the projectile, heating the ambient gas mixture to a temperature sufficient to cause auto-ignition in the aft section of the body. This combustion provides thrust to continuously accelerate the projectile down the length of the tube. At

projectile velocities sufficiently beyond the ambient gas Chapman-Jouguet (C-J) detonation velocity, an oblique detonation wave stabilized on the body becomes the preferred mode of operation.

1.2 Previous Work

We now turn to a discussion of previous analytical, experimental, and numerical work in this field. The two recent review articles of Shepherd (1994) and Powers (1994) are good sources of additional historical information.

1.2.1 Analytical Work

The main theory describing oblique detonation waves is the Rankine-Hugoniot analysis first developed in the 1950s and 1960s. Representative early studies are those of Sierstrunck et al. (1953) and Gross (1963). This analysis, described further in Chapters 2 of this dissertation, represents the oblique detonation wave as a fully coupled shock/reaction front with instantaneous energy release. The best review of this theory is that of Pratt et al. (1991).

More recently, there has also been some effort to incorporate reaction zone structure into oblique detonation wave theory. Perturbation methods have been applied successfully to model oblique detonation wave structure assuming both one-step irreversible (Powers and Stewart, 1992) and two-step irreversible (Powers and Gonthier, 1992) reactions. These methods have also been applied to the study of the response of oblique detonation waves to disturbances (Lasseigne and Hussaini, 1993). Shepherd (1994) has calculated the structure of a straight oblique detonation wave using numerical integration of a detailed H₂-air chemical kinetic mechanism.

1.2.2 Experimental Studies

Experimental data on shock-induced combustion phenomena at high-speed flow conditions have been obtained by three methods. A number of studies have obtained experimental flow visualization results by directly firing projectiles at high velocity into a test section filled with fuel-oxidizer (typically H₂/O₂) mixtures (Fig. 1.2a). This approach has the advantage of enabling a wide range of velocities (assuming a projectile launching system powerful enough) to be studied, and a variety of gas mixtures to be safely used. The earliest studies were performed by Ruegg and Dorsey (1962) and Behrens et al. (1965) in the early 1960s. Their work primarily focused on validating the technique and demonstrating the range of combustion phenomena, both steady and oscillatory, around spherical projectiles. The later work of Lehr (1972) similarly demonstrated shock-induced combustion around hemispherically blunted and conical projectiles. The oscillatory combustion modes,

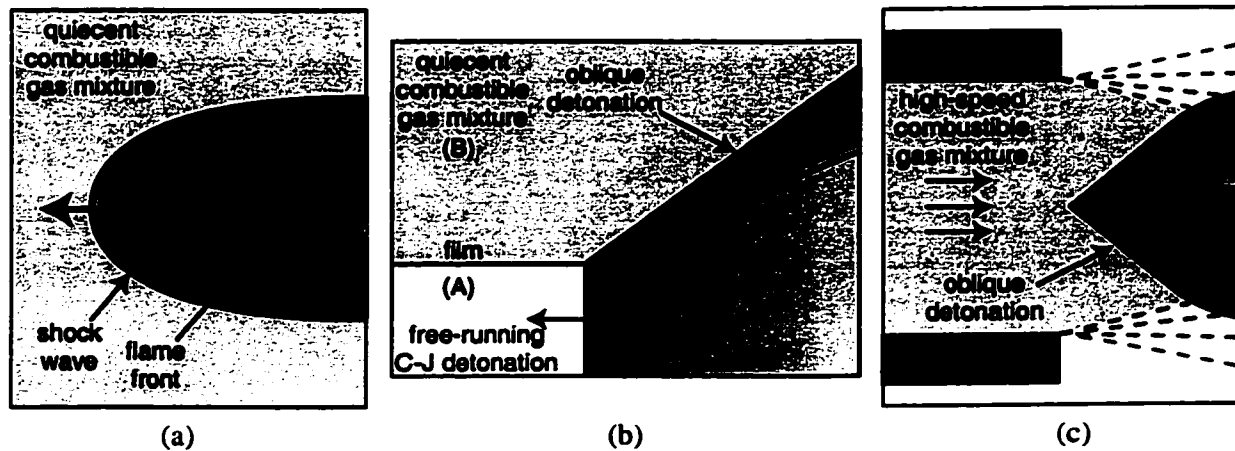


Figure 1.2: Experimental data on oblique detonation waves and shock-induced combustion have been obtained by 3 methods: (a) direct projectile firings into a combustible gas mixture, (b) the two-layer, “oblique shock tube” experiment, (c) accelerating a flow of combustible gas over a fixed model.

which occur when $V_{\text{projectile}} \lesssim V_{\text{C-J}}$, were studied in greater detail by McVey and Toong (1971) and by Alpert and Toong (1972), who also advanced a 1-dimensional wave interaction model to account for the observed unsteady interactions between the shock and reaction front.

More recently, a number of experiments using this approach have studied the stabilization of oblique detonation waves on projectiles. Higgins and Bruckner (1996) sought to determine the critical conditions needed to stabilize a detonation, and compared their data with the theories of Lee (1994) and Vasiljev (1994). Kaneshige and Shepherd (1996) also investigated the detonation initiation threshold at projectile velocities greater than the C-J speed. Both of these investigations utilized spherical projectiles.

Another approach is the two-layer, “oblique shock tube” experiment (Fig. 1.2b) first described by Dabora et al. (1965). In this method, two pre-mixed combustible gas mixtures are initially separated by a horizontal thin film. The mixtures are selected so that the C-J detonation velocity of the lower layer is greater than that of the upper layer. At the start of the experiment, a free-running, normal C-J detonation wave is initiated in the lower layer. The increased pressure behind the C-J detonation wave has the effect of driving the thin film into the upper layer at inclined angle, which can then produce oblique shock-induced combustion or an oblique detonation wave in the upper layer mixture. As may be deduced from this description, this approach produces results quite specific to oblique shock-induced combustion and detonation wave formation in wedge-type flows. However, the method enables a wide variety of mixtures, fill pressures, and velocities to be studied. Representative articles are those of Dabora et al. (1991) and Viguiet et al. (1994, 1997). These

studies were the first to systematically examine the effect of Mach number and mixture sensitivity on the transition from shock-induced combustion to oblique detonation waves.

The final approach is to fix a model of the projectile in the laboratory reference frame, and use a hypersonic test facility to generate a high-speed flow of combustible mixture around the body (Fig. 1.2c). This method allows for considerable instrumentation of the test body, and for a variety of geometries to be studied. The principal source of difficulty with this approach lies in safely generating a high-speed uniform stream of combustible gas mixture. Early experiments in oblique shock-induced combustion were performed by Gross and Chinitz (1960) and Rubins and Rhodes (1963) using Mach 3 supersonic wind tunnels. More recently, expansion tubes (Trimpi, 1962) have been applied to this problem by a number of researchers in order to attain higher freestream velocities. Expansion tubes also offer the advantage of directly accelerating a premixed combustible gas mixture, so that fuel/air mixing issues are avoided. Initial work in the early 1990s, performed by Srulijes et al. (1992), validated the use of expansion tubes for these problems. Simultaneous PLIF/schlieren imaging has been applied by Kamel et al. (1997) and Morris et al. (1998) to both blunt-body and wedge flows using this approach. A modified approach which injects hydrogen into the high-speed air stream generated by an expansion tube has also been recently developed by Srulijes et al. (1999).

1.2.3 Numerical Studies

The past two decades have witnessed dramatic advances in easily accessible computational power. This development has led to a large number of investigations utilizing computational fluid dynamics (CFD) solutions to study shock-induced combustion problems. Several studies have analyzed the steady and unsteady combustion modes produced by blunt projectiles. The numerical results are frequently compared with the direct-firing experiments, such as those of Lehr (1972), described previously. Representative studies are those of Wilson and MacCormack (1992), Matsuo and Fujiwara (1993a), Sussman (1994) and Yungster and Radhakrishnan (1996).

A number of numerical studies have also specifically addressed oblique detonation wave formation and stabilization in wedge and conical flows. Early Euler-level simulations of oblique detonation waves were performed in the late 1980s by Cambier et al. (1989). More detailed simulations by Li et al. (1994), Vlasenko and Sabelnikov (1994) and Papalexandris (2000) examined the near-field finite-rate chemistry structure which is described in more detail in Chapter 2. All found that oblique detonation waves could be stabilized under certain conditions, though in some cases more restrictive than predicted by standard shock polar theory. Matsuo and Fujiwara (1993b) and Lefebvre and Fujiwara (1995) studied oblique detonations in spherically blunted wedge and conical flows,

and also found that oblique detonation waves could be stabilized, though a nose tip radius below a certain value led to detached detonation fronts. Grissimer and Powers (1996) studied the stabilization conditions on a wedge body curved so that the resultant detonation wave was straight. Full Navier-Stokes simulations performed by Li et al. (1993) and Figueira da Silva and Deshaies (1998) examined ignition produced by viscous heating in, and shock-strengthening produced by, the leading-edge boundary layer produced at the tip of the wedge.

Relatively few studies have directly compared numerical simulations of wedge- or cone-induced oblique detonations to actual experimentally obtained flow visualization results. Viguier et al. (1996) compared detailed simulations, using an Euler code with full H₂-air chemistry, with oblique shock tube results. Generally good agreement was obtained, though it is evident that the non-constant film angle generated in the experiments produced combustion effects not observed in the numerical simulations. This is an area of this field in need of further study.

1.3 Focus of this Study

The goal of this study is to improve understanding of oblique shock-induced combustion and detonation waves through modern experimental and numerical modeling methods. Chapter two presents an overview of the existing theory of oblique detonations in wedge flows. A basic, calorically perfect gas Rankine-Hugoniot and shock polar analysis is provided first, followed by the extension of this theory to account for real thermochemistry effects, and finally finite-rate chemistry. Chapter three describes the flow facility and experimental apparatus used in obtaining the OH PLIF/schlieren flow visualization results. Chapter four presents the results of numerical simulations examining the transition from oblique shock-induced combustion to detonation waves in three different regimes on the shock polar diagram. The numerical results in one regime are also compared to OH PLIF/schlieren imaging results obtained in the laboratory. Chapter five presents conclusions and recommendations for future work.

Chapter 2

Theory of Oblique Shock and Detonation Waves in Wedge Flows

It is important to review the relevant theory of shock-induced combustion and oblique detonation waves. This chapter describes the theoretical background for these waves within the context of a wedge at zero angle of attack in supersonic flow. The first part of the chapter will concentrate on explaining the essential features of oblique shocks and detonation waves using a simplified Rankine-Hugoniot analysis, assuming a constant specific heat ratio, γ , and constant energy release, Q . This analysis essentially shows that the jump conditions across oblique waves are defined by the inflow velocity component normal to the wave. The role of the shock polar diagram as an aid to understanding these flows is also explained. We will then explore the effect of real thermochemistry on these solutions. Finally, the role of finite-rate chemistry will be discussed, first limited to normal and straight oblique shocks, then described more generally for a complete wedge-induced oblique shock and detonation flow.

2.1 Simplified Rankine-Hugoniot Analysis

We begin with a Rankine-Hugoniot analysis which relates the jump conditions across an oblique shock or detonation wave to the freestream properties. In order to simplify the derivation, we will initially assume a constant specific heat ratio, γ , for the gas. We will also assume that the energy release for a combustible gas mixture can be represented by a constant value, Q . Furthermore, we assume that this energy is released instantaneously across the shock wave; in doing so we are effectively ignoring the effects of finite-rate chemistry.

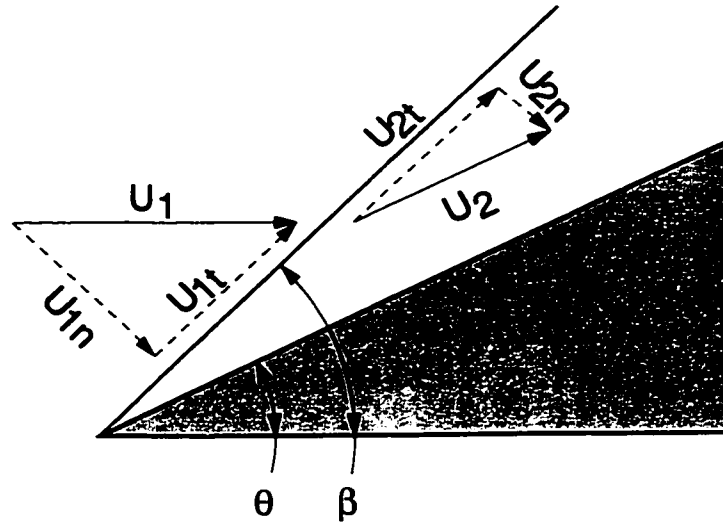


Figure 2.1: Schematic of an attached oblique shock or detonation in supersonic flow around a wedge of angle θ . Normal and tangential velocity components before and after the shock wave are shown in the figure.

2.1.1 Flow Geometry

As shown in Fig. (2.1), the velocity of the gas flow before and after the oblique shock or detonation wave can be broken into components normal and tangential to the wave. These components, in terms of the oblique wave angle β , and the flow turning angle θ , are

$$u_{1n} = u_1 \sin \beta, \quad u_{2n} = u_2 \sin(\beta - \theta) \quad (2.1)$$

$$u_{1t} = u_1 \cos \beta, \quad u_{2t} = u_2 \cos(\beta - \theta) \quad (2.2)$$

2.1.2 Conservation Laws

Using the normal and tangential coordinate system, we can write the conservation laws for a control volume around the wave on a specific mass basis as

Conservation of mass:

$$\rho_1 u_{1n} = \rho_2 u_{2n} \quad (2.3)$$

Conservation of normal momentum:

$$p_1 + \rho_1 u_{1n}^2 = p_2 + \rho_2 u_{2n}^2 \quad (2.4)$$

Conservation of tangential momentum:

$$(\rho_1 u_{1n}) u_{1t} = (\rho_2 u_{2n}) u_{2t} \quad (2.5)$$

or simplified via Eq. (2.3) as

$$u_{1t} = u_{2t} = u_t \quad (2.6)$$

Conservation of energy:

$$h_1 + (u_{1n}^2/2) = h_2 + (u_{2n}^2/2) \quad (2.7)$$

Note that in Eq. (2.7) we have written the enthalpy as a sum of the specific and chemical enthalpies. Throughout this analysis we will use the ideal gas equation of state: $p = \rho RT$. If we further assume that the gas is calorically perfect ($\gamma = c_p/c_v = \text{const.}$) and that the heat release can be written as Q units of heat per unit mass, then we can write

$$C_p T_1 + Q + (u_{1n}^2/2) = C_p T_2 + (u_{2n}^2/2) \quad (2.8)$$

2.1.3 Jump Conditions

By combining the geometric relations, Eqs. (2.1) and (2.2) with conservation of mass (2.3) and tangential momentum (2.6) we can define the specific volume ratio

$$X \equiv \frac{v_2}{v_1} = \frac{\rho_1}{\rho_2} = \frac{u_{2n}}{u_{1n}} = \frac{\tan(\beta - \theta)}{\tan \beta} \quad (2.9)$$

If we introduce the Mach number, $M \equiv u/\sqrt{\gamma RT}$ (where $M_{1n} = M_1 \sin \beta$, etc.), we can combine the conservation of mass and normal-momentum equations, Eqs. (2.3) and (2.4), as

$$\frac{p_2}{p_1} = 1 + \gamma M_{1n}^2 (1 - X) \quad (2.10)$$

This is one definition for the Rayleigh line, which is typically shown in a Rankine-Hugoniot diagram (Fig. 2.2). The example Rayleigh line shown in the figure is plotted using an inflow Mach number, M_{1n} , of 5. Note that the Rayleigh line is essentially a line of constant mass flux. An increase in the inflow velocity M_{1n} results in a steeper slope in the diagram.

The Hugoniot curve itself may be derived by using the normal-momentum equation to eliminate the velocity terms in the energy equation. We then use the ideal gas equation of state to convert from temperature to pressure and density, giving

$$\frac{p_2}{p_1} = \frac{1 + \bar{Q} + \frac{\gamma-1}{2\gamma}(1+X)}{X - \frac{\gamma-1}{2\gamma}(1+X)} \quad (2.11)$$

where the normalized heat release is defined as $\bar{Q} \equiv Q/C_p T_1$.

Combining Eqs. (2.10) and (2.11) we get a quadratic polynomial expression for \bar{Q} in terms of X . This equation can be rearranged to give

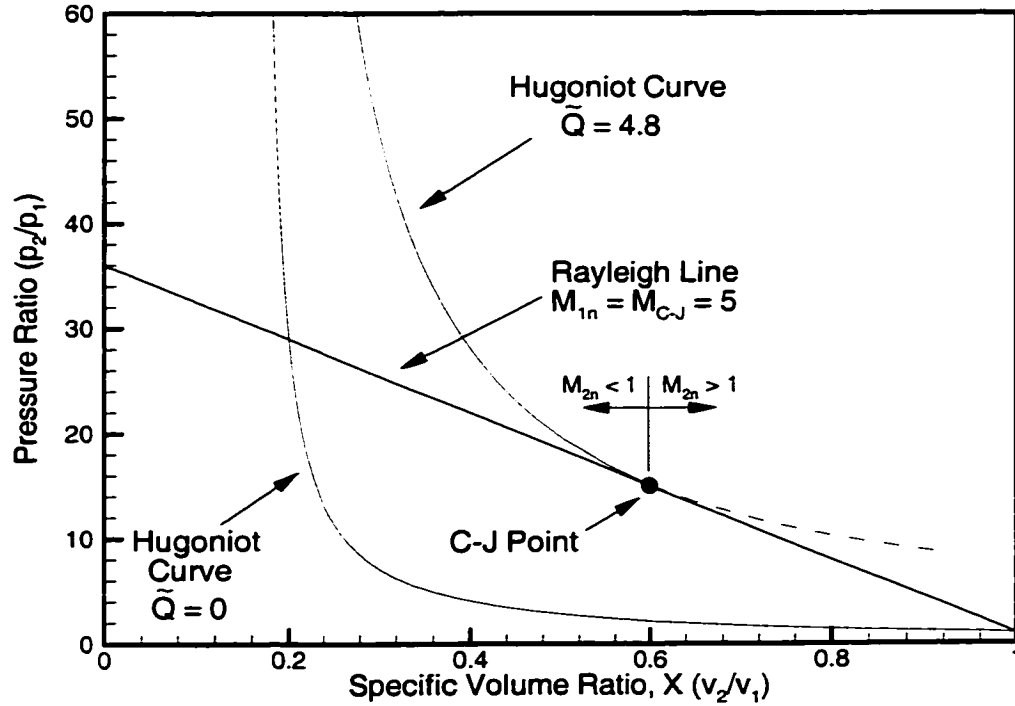


Figure 2.2: Rankine-Hugoniot diagram showing solutions for an inert shock ($\bar{Q} = 0$), and for a shock with instantaneous energy release ($\bar{Q} = 4.8$). A Rayleigh line corresponding to the Chapman-Jouguet velocity is shown.

$$X = \frac{1 + \gamma M_{in}^2 \pm \sqrt{(M_{in}^2 - 1)^2 - 2(\gamma + 1)M_{in}^2 \bar{Q}}}{(\gamma + 1)M_{in}^2} \quad (2.12)$$

These jump conditions are essentially identical to those for standard 1-D shocks, using the velocity component normal to the oblique wave as the relevant inflow velocity parameter. Note that there are two roots in Eqn. 2.12. For an inert gas with $\bar{Q} = 0$, the relation simplifies to a trivial solution ($X = 1$) for the positive root, and becomes

$$X = \frac{2 + (\gamma - 1)M_{in}^2}{(\gamma + 1)M_{in}^2} \quad (2.13)$$

for the negative root. This equation, along with Eqn. 2.11, is shown as the blue Hugoniot curve over a range of inflow Mach numbers in Fig. 2.2. The intersection point of the Rayleigh line with the relevant Hugoniot curve gives the unique gasdynamic solution for a shock wave at the given conditions of M_{in} , γ , and \bar{Q} .

Generally, both roots in Eqn. 2.12 are nontrivial when the discriminant $[(M_{1n}^2 - 1)^2 - 2(\gamma + 1)M_{1n}^2\bar{Q}]$ is positive. The special case when the discriminant is zero, known as the Chapman-Jouguet (C-J) point, is defined at a unique inflow Mach number for each particular positive value of \bar{Q} . The simplest form defines a particular \bar{Q} for a given $M_{1n} = M_{C-J}$

$$\bar{Q} = \frac{(M_{C-J}^2 - 1)^2}{2(\gamma + 1)M_{C-J}^2} \quad (2.14)$$

This expression is often useful for estimating the normalized energy release of a combustible gas mixture from C-J detonation velocity data. This equation can also be recast to yield a quadratic expression for the C-J Mach number in terms of γ and \bar{Q}

$$M_{C-J}^2 = 1 + (\gamma + 1)\bar{Q} \pm \sqrt{(1 + (\gamma + 1)\bar{Q})^2 - 1} \quad (2.15)$$

for the supersonic flows considered here, the positive root is the appropriate one. In the example case shown in Fig. 2.2 ($\gamma = 1.4$, $\bar{Q} = 4.8$) this results in $M_{C-J} = 5$.

A general expression for the normal component of the Mach number behind the wave, M_{2n} , is given by

$$M_{2n}^2 = \frac{M_{1n}^2 X}{1 + \gamma M_{1n}^2 (1 - X)} \quad (2.16)$$

If we substitute in for the Chapman-Jouguet values of M_{1n} and X ($M_{1n} = M_{C-J}$, $X = X_{C-J} = (1 + \gamma M_{C-J}^2)/[(\gamma + 1)M_{C-J}^2]$) we find that this expression algebraically reduces to unity. Thus, the C-J point has the unique property that the normal component of velocity of the post-shock gases (combustion products) is sonic with respect to the wave ($M_{2n} = 1$). This property means that acoustic disturbances behind the detonation are unable to influence the wave, and explains why a C-J detonation is able to freely propagate indefinitely without a piston or contact surface driving it forward. The energy needed to sustain the shock front is provided entirely by the latent energy release of the gas mixture.

The C-J point is critically important in oblique detonation wave theory because it defines the lower limit of inflow velocity which will permit a fully stabilized oblique detonation solution. Inflow Mach numbers less than the C-J speed ($M_{1n} < M_{C-J}$) result in a negative value for the discriminant in Eqn. 2.12. A real solution for Eqn. 2.12 is then impossible. This is more clearly seen when the Rayleigh line is plotted for a sub-detonative shock velocity in our example Rankine-Hugoniot diagram (Fig. 2.3). The Rayleigh line intersects with the inert Hugoniot curve, but does not intersect the Hugoniot solution for energy release ($\gamma = 1.4$, $\bar{Q} = 4.8$). Thus, there is no steady solution possible for this case. In physical terms, if we consider the C-J point as a balance between mechanical

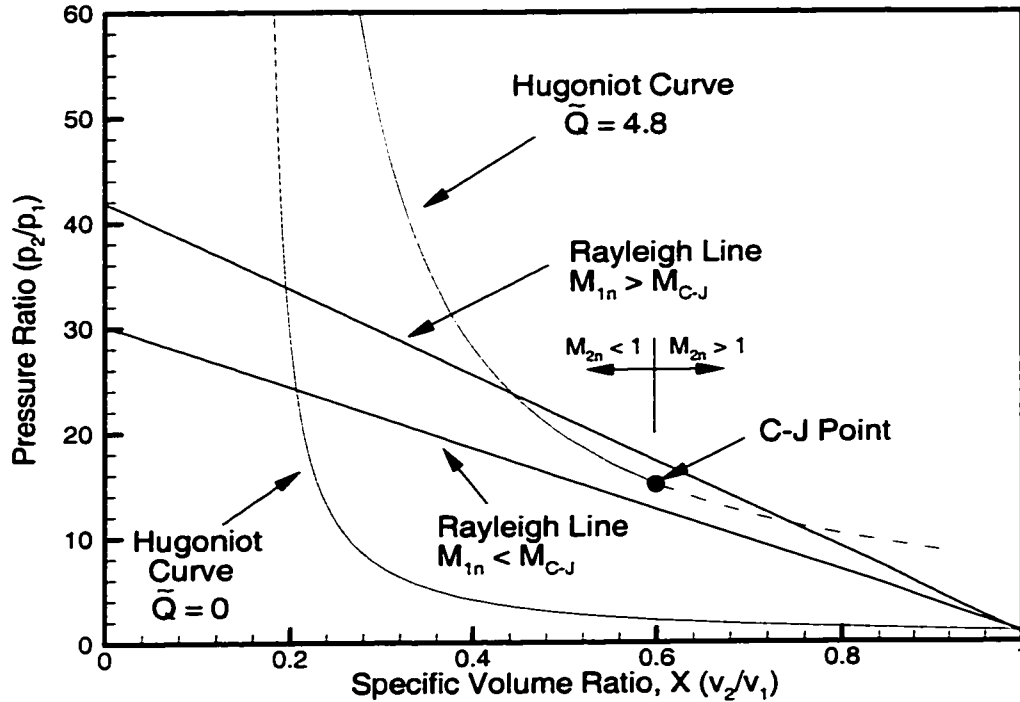


Figure 2.3: Rankine-Hugoniot diagram showing solutions for an inert shock ($\bar{Q} = 0$), and for a shock with instantaneous energy release ($\bar{Q} = 4.8$). Rayleigh lines corresponding to both sub-detonative ($M_{1n} < M_{C-J}$) and super-detonative ($M_{1n} > M_{C-J}$) flow conditions are shown.

inflow energy and chemical energy, this latter case may be thought of as a relative imbalance in favor of chemical energy. Thus, the amount of energy release across the shock is too great to keep the wave steady at inflow velocities less than the C-J speed.

Real solutions for Eqn. 2.12 are possible when the shock is super-detonative ($M_{1n} > M_{C-J}$). We then find two possible solutions to the equation; both are shown in the example case (assuming $\gamma = 1.4$, $\bar{Q} = 4.8$) of Fig. 2.3. The negative root is shown as the solid red line, whereas the positive root is shown as the dashed red line. Note that the Rayleigh line corresponding to $M_{1n} > M_{C-J}$ passes through both solution curves. The question then naturally arises as to which one applies in reality. It can be shown, using Eqn. 2.16, that M_{2n} is less than unity for the negative root, and greater than one for the positive root. Since a value of $M_{2n} > 1$ makes it impossible for the wedge to influence the oblique wave, from stability considerations the positive root may be ruled out. The only valid solution remaining for $M_{1n} > M_{C-J}$ is the negative root.

Note that Rayleigh lines intersects the red Hugoniot curve at a lower pressure ratio (p_2/p_1) and

a higher specific volume ratio (X) than the inert blue curve. Thus, the effect of energy release is to reduce the final pressure and density compared to an inert shock. The relative increase in specific volume is greater than the relative decrease in pressure, resulting in an increase in temperature.

2.2 Shock Polar Theory

Oblique shock and detonation flows are typically studied with the aid of a shock polar diagram. Shock polars relate a particular oblique shock characteristic (β , p_2/p_1 , etc.) to the wedge turning angle, θ . In this discussion, we will primarily limit ourselves to wave angle polars, β vs. θ . We first discuss the solution procedure for deriving the polar curve. The basic features of polar diagrams are then explained using an inert example case, before moving on to the more complicated effects of energy release on the diagram.

2.2.1 Solution Procedure

A particular shock polar curve is calculated for a fixed set of M_1 , γ , and \bar{Q} . One solution procedure is then as follows: First, identify a minimum inflow Mach number associated with a given curve. In the case of an inert shock solution ($\bar{Q} = 0$), this is simply $M_{1n,\min} = 1$. For $\bar{Q} > 0$, $M_{1n,\min} = M_{C-J}$, which may be found using Eqn. 2.15. If we then vary M_{1n} from the minimum value to M_1 , we may compute

$$\beta = \sin^{-1}(M_{1n}/M_1) \quad (2.17)$$

For each value of M_{1n} we calculate X from the negative root of Eqn. 2.12. Given β and X , we may then find θ by rearranging Eqn. 2.9 as

$$\theta = \beta - \tan^{-1}(X \tan(\beta)) \quad (2.18)$$

2.2.2 Inert Shock Polar Diagram

An example shock polar diagram for an inert gas with no energy release ($\bar{Q} = 0$) at a fixed freestream Mach number ($M_1 = 8$) and specific heat ratio ($\gamma = 1.4$) is shown in Fig. 2.4. Note that a solution only exists for a certain range of flow turning angles. The maximum flow turning angle for which a solution exists is termed the detachment point ($\theta_{\det,0}$ in the figure). Wedge turning angles less than $\theta_{\det,0}$ will lead to a straight oblique shock attached to the tip of the wedge. The flow behind the shock is uniform and everywhere parallel to the wedge surface. This situation is

pictured schematically in case (a) in the figure. Note also that, for $\theta < \theta_{\text{det},0}$, two solutions exist for each flow turning angle. The lower branch of the polar curve is termed “weak,” while the upper branch is called “strong.” The weak solution is typically characterized by a supersonic post-shock velocity ($M_2 > 1$), although there is a narrow region of the weak branch near the detachment point where the post-shock flow is subsonic ($M_2 < 1$). This region can be quite noticeable in modestly supersonic flows ($M_1 \sim 2$), but becomes vanishingly small at hypersonic Mach numbers (less than 0.2 degree difference in wave angle at $M_1 = 8$, $\gamma = 1.4$). See the classic text of Shapiro (1953) for explicit formulae and further details. For the purposes of our discussion here, we will assume the detachment point is essentially equivalent to the sonic transition point. In contrast, the post-shock Mach number for the strong solution is always less than unity ($M_2 < 1$). Generally, the weak solution is observed in nature unless a boundary condition, such as high back pressure caused by a downstream obstruction, forces the solution on to the strong branch.

If the wedge turning angle is increased beyond $\theta_{\text{det},0}$, the shock detaches away from the wedge (case (b) in the figure). This case is significantly more complex than in the attached shock case, and is similar to supersonic blunt body flows. It is characterized by a curved shock standing off from the tip of the wedge. The shock is initially normal ($\beta = 90^\circ$) in front of the wedge tip, and becomes progressively less steep moving away from that point. The shock standoff distance, and the overall size of the detached shock, is governed by the size of wedge itself. The flow between the curved shock and expansion corner is subsonic, and allows the wedge forebody lengthscale to influence the detached shock position. This is in contrast to attached shock flows, in which the post-shock velocity is supersonic and prevents information transfer along the wedge forebody. The detached shock solution can be thought of as passing through every point on the strong branch of the polar diagram, ranging from $\beta = 90^\circ$ to $\beta = \beta_{\text{det},0}$. The point at which $\beta = \beta_{\text{det},0}$ marks the limit of the $M = 1$ sonic line and expansion fan radiating from the wedge expansion corner. A nonuniform velocity field behind the detached shock turns the flow so that the slip condition is satisfied along the forebody.

2.2.3 Exothermic Shock Polar Diagram

An example shock polar diagram showing solutions for both an inert gas (blue curve, $\tilde{Q} = 0$) and a gas with instantaneous energy release across the shock (red curve, $\tilde{Q} = 4.8$) is shown in Fig. 2.5. The specific heat ratio and freestream Mach number are fixed ($\gamma = 1.4$, $M_1 = 8$). These values of γ and \tilde{Q} match those used in the Rankine-Hugoniot diagram in Fig. 2.2. As was the case in that figure, the C-J state is of critical significance to the exothermic $\tilde{Q} = 4.8$ curve on the shock polar diagram. The lower half of the curve is limited by the θ , β coordinates of the C-J point. Similar

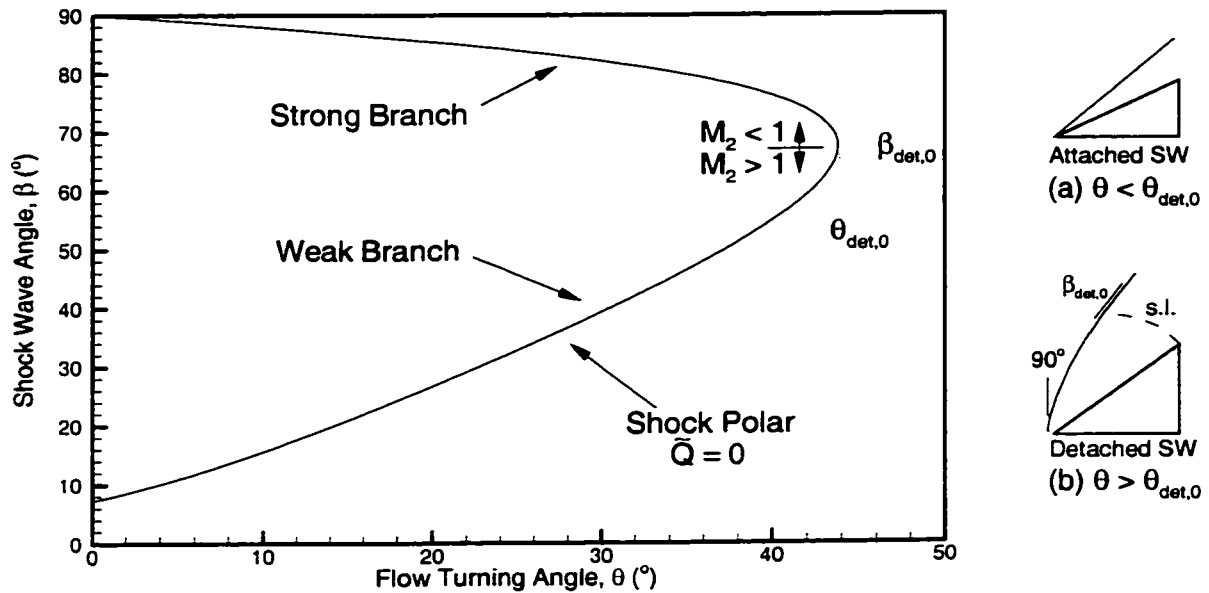


Figure 2.4: Example shock polar diagram for an inert gas with no energy release ($\bar{Q} = 0$) at a fixed freestream Mach number ($M_1 = 8$) and specific heat ratio ($\gamma = 1.4$). Case (a): attached shock wave (SW) solutions possible for $\theta < \theta_{det,0}$. Case (b): shock wave detaches when $\theta > \theta_{det,0}$.

to the inert polar curve, the exothermic curve has both a lower branch and upper branch. Note that the primary effect of energy release is to reduce the associated wedge turning angle, θ , compared to the inert solution at a given wave angle, β . This phenomenon may be understood by recalling that energy release reduces the final post-shock density, ρ_2 , from a corresponding inert shock (at fixed β , and hence M_{1n}). By conservation of mass, Eqn. 2.3, a reduction of ρ_2 must be accompanied by an increase in the post-shock velocity normal to the wave, u_{2n} . As shown in Fig. 2.1, an increase in u_{2n} will reduce the flow turning angle, θ , since u_{2t} is fixed.

As was the case for the inert case, the exothermic curve has a maximum wedge turning angle which will permit an attached shock solution. This detachment point, termed $\theta_{det,q}$, is at a lower flow turning angle than the detachment point on the inert curve, $\theta_{det,0}$. Thus an attached oblique exothermic shock (detonation) wave is only defined over the range $\theta_{C-J} < \theta < \theta_{det,q}$, in contrast to an inert oblique shock which is defined for $0 < \theta < \theta_{det,0}$. This behavior is shown schematically in cases (a), (b), and (c) in the right panel of Fig. 2.5. For comparison, both inert and exothermic shocks are shown in the figure. As shown in case (b), attached solutions are theoretically possible for both inert and exothermic shocks if $\theta_{C-J} < \theta < \theta_{det,q}$. If the wedge angle is decreased to a value below the C-J point ($0 < \theta < \theta_{C-J}$), then an attached solution is only possible for inert shocks

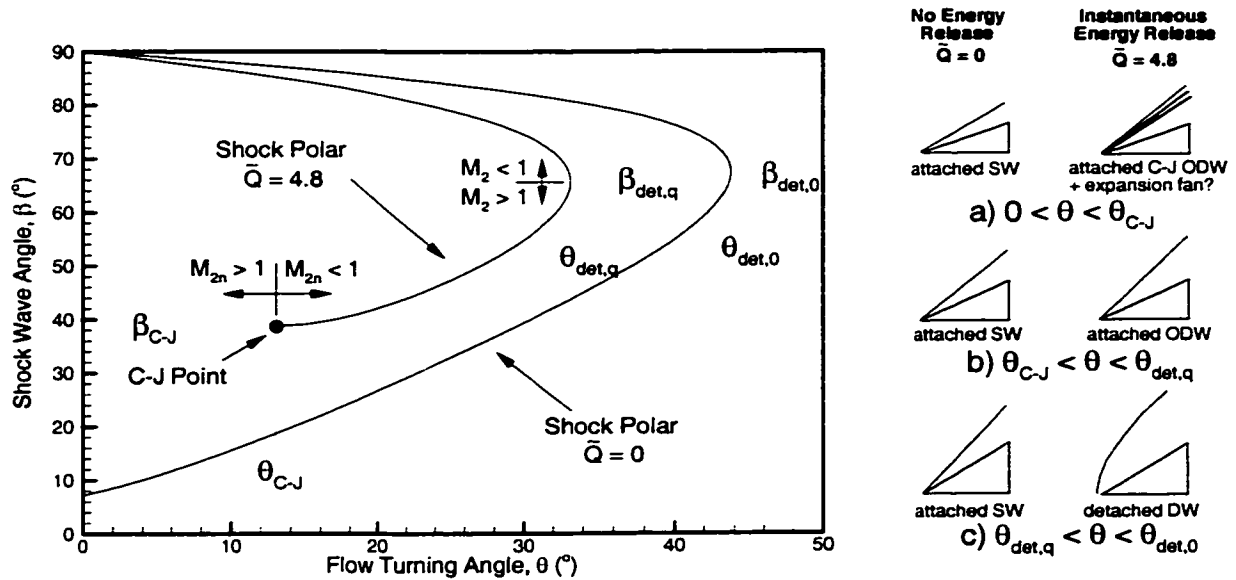


Figure 2.5: Example shock polar diagram showing solutions for both an inert gas (blue curve, $\bar{Q} = 0$) and a gas with instantaneous energy release across the shock (red curve, $\bar{Q} = 4.8$). Specific heat ratio and freestream Mach number are fixed ($\gamma = 1.4$, $M_1 = 8$). Case (a): hypothetical C-J oblique detonation wave followed by Prandtl-Meyer expansion fan for $0 < \theta < \theta_{C-J}$. Case (b): attached oblique detonation wave solution possible for $\theta_{C-J} < \theta < \theta_{det,q}$. Case (c): detonation detaches when $\theta_{det,q} < \theta < \theta_{det,0}$.

(case (b)). An attached exothermic shock in this regime would have an inflow velocity below the C-J speed. As shown in the previous section, this would result in an unstable wave which could not remain attached to the wedge. It has been speculated by some writers (Ashford and Emanuel, 1994; Shepherd, 1994) that an oblique C-J detonation at a wave angle of β_{C-J} , followed immediately by a steady Prandtl-Meyer expansion wave to turn the flow parallel to the wedge forebody, could be stabilized on a wedge at an angle less than θ_{C-J} . However, though this theory has grounds in 1-D detonation wave experiments in shock tubes, it has never been directly observed experimentally in 2-D wedge flows. Another regime (case (c)) is possible if the wedge angle is increased to a value in between the two detachment points on the diagram ($\theta_{det,q} < \theta < \theta_{det,0}$). Thus, although this case also allows attached solutions for inert shocks, an exothermic shock would detach away from the wedge tip in the same fashion as described for inert shock detachment. The detonation would start out as normal ($\beta = 90^\circ$) in front of the tip, and decay to a detachment value ($\beta = \beta_{det,q}$) in the far field as it encountered the expansion fan radiating from the wedge expansion corner. Again, a nonuniform velocity field behind the curved shock turns the flow so that the slip condition is maintained along the wedge forebody.

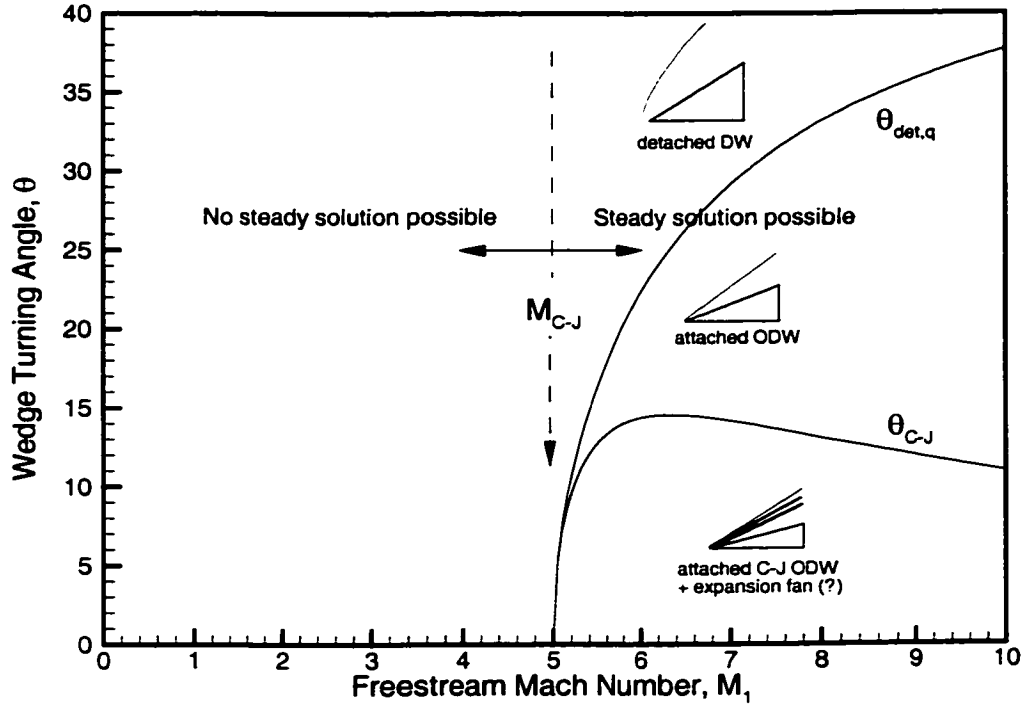


Figure 2.6: Example plot showing effect of freestream Mach number on the maximum ($\theta_{\text{det},q}$) and minimum (θ_{C-J}) wedge turning angles which will permit an attached exothermic shock solution. Specific heat ratio and energy release are fixed ($\gamma = 1.4$, $\bar{Q} = 4.8$)

Our discussion to this point has made clear that an exothermic shock or detonation wave can only be stabilized if the inflow velocity is greater than the C-J speed of the gas mixture. In oblique wedge flows, this naturally implies that the freestream velocity must also be greater than the C-J speed. An example plot showing the effect of freestream Mach number on the maximum and minimum wedge turning angles permitting an attached oblique detonation is shown in Fig. 2.6. It is evident from the figure that, although no attached solutions are possible when $M_1 < M_{C-J}$, the range of available turning angles increases rapidly as M_1 exceeds M_{C-J} .

2.3 Real Thermochemistry Calculations

Throughout the first two sections of this chapter, we have assumed that the ambient gas mixture in the flow is calorically perfect, and that the energy release can be represented by a simple, constant value at all conditions. We will now relax these assumptions to include a more realistic model of

gas behavior and energy release at elevated temperatures. Throughout this analysis we will continue to assume that the gas is ideal (thermally perfect). However, we first discuss the issue of vibrational excitation, which affects the constant- γ assumption used previously. The effects of equilibrium combustion chemistry at high temperatures are then discussed, with a view toward explaining the deviations from the constant- \tilde{Q} model. The practical effect of these issues on the shock polar diagram is then presented and analyzed.

2.3.1 Vibrational Excitation

Vibrational excitation typically becomes important in gasdynamics calculations using high temperature air. At lower temperatures, the translational and rotational energy modes of molecules are fully excited. This means that the energy of the gas increases linearly with temperature, leading to constant specific heat coefficients, c_p , and c_v . However, as the temperature is increased, the vibrational energy modes of molecules can also become partially excited, and c_p and c_v (and therefore γ) become functions of temperature. Typically, the contribution of vibrational energy becomes important when the temperature rises to an appreciable fraction of the characteristic vibrational energy, Θ_v , of a molecule ($\Theta_v = 2270$ K for O_2 , 3390 K for N_2). For our purposes, the primary effect on shock wave calculations is the reduction in the specific heat ratio, γ . For example, for N_2 at $T = 300$ K, $\gamma = 1.40$. However, at $T = 1000$ K, $\gamma = 1.34$, and at $T = 2000$ K, $\gamma = 1.30$. As will be shown later in this section, this reduction in γ has a significant effect on the post-shock density and temperature.

For computational purposes, the specific heats and enthalpy of a particular gas species can be expressed as fourth- and fifth-order (respectively) polynomial fits in the NASA-Lewis format (McBride et al., 1993):

$$\frac{C_p}{R} = a_1 + a_2T + a_3T^2 + a_4T^3 + a_5T^4 \quad (2.19)$$

$$\frac{H^0}{RT} = a_1 + \frac{1}{2}a_2T + \frac{1}{3}a_3T^2 + \frac{1}{4}a_4T^3 + \frac{1}{5}a_5T^4 + a_6\frac{1}{T} \quad (2.20)$$

Given these functions, it is then relatively straightforward to compute the jump conditions across a shock (assuming state 1 is known, and the chemistry is frozen) via Newton-Raphson iteration of the specific volume ratio, X , to satisfy the energy equation (Eq. 2.7) recast as

$$h_2(T_2) = h_1(T_1) + (u_{1n}^2/2)(1 - X^2) \quad (2.21)$$

and using the ideal gas law and the expression for the Rayleigh line (Eq. 2.10) to relate T_2 to X

$$T_2 = T_1[X + (\rho_1 u_{1n}^2/p_1)(X - X^2)] \quad (2.22)$$

2.3.2 Equilibrium Chemistry Considerations

The other main deviation from ideal theory in high temperature combustion flows, typically, is the formation of radical species which consume part of the heat of combustion. Consider a water formation reaction which is important in the energy release phase of H₂-O₂ combustion kinetics:



The law of mass action for this reaction is written

$$K_p = \frac{p_{\text{H}_2\text{O}}^*}{p_{\text{H}}^* p_{\text{OH}}^*} = \exp\left(-\frac{\Delta g^0}{RT}\right) \quad (2.24)$$

where p_i^* is the partial pressure of species i with respect to the standard pressure (p_i/p_0) at equilibrium. The term Δg^0 denotes the Gibbs free energy change in the reaction; in this particular case, $\Delta g^0 = \hat{\mu}_{\text{H}_2\text{O}}^0 - \hat{\mu}_{\text{H}}^0 - \hat{\mu}_{\text{OH}}^0$. The chemical potential (Gibbs free energy per unit mole), $\hat{\mu}^0$, is purely a function of temperature: $\hat{\mu}^0(T) = \hat{h}^0(T) - T[\hat{s}^0(T)]$. The subscript and superscript 0 denotes standard pressure (1 bar in these calculations).

Examining Eq. 2.24, we see that K_p is essentially a ratio of products to reactants at equilibrium. For example, at $T = 2000$ K, $K_p = 3.8 \times 10^6$. This means that the product species dominates, and the partial pressure of H₂O is much greater than that of H and OH. This temperature is representative of a simple premixed, adiabatic flame. However, due to shock-heating, the final temperature in shock-induced combustion flows can be much higher. The equilibrium constant for this reaction rapidly decreases at high temperatures ($K_p = 1.2 \times 10^2$ at $T = 3000$ K, and $K_p = 6.7 \times 10^{-1}$ at $T = 4000$ K). Under these conditions, the equilibrium concentrations of H and OH can no longer be neglected, as they form a significant fraction of the final mixture composition.

An example plot showing the effect of shock strength on equilibrium composition and post-shock temperature increase ($\Delta T = T_{2,\text{eq}} - T_{2,\text{fr}}$) is shown in Fig. 2.7. Stoichiometric H₂-air ($2\text{H}_2 + \text{O}_2 + 3.76\text{N}_2$) at $T_1 = 280$ K, and $P_1 = 1.0$ atm was assumed. The calculations were performed using CET-89, the NASA-Lewis Equilibrium Chemistry Program (Gordon and McBride, 1976). At the lowest shock strength calculated ($M_{1n} = M_{C-J} = 5$), both H₂ and OH have significant populations at equilibrium. As the shock strength is increased, the post-shock temperature rises and the populations of H, NO, O, and O₂ become increasingly important. The increase in the populations of radicals and unburned reactants reduces the amount of water formed. As a result, the post-shock temperature change due to combustion ($\Delta T = T_{2,\text{eq}} - T_{2,\text{fr}}$) is significantly reduced as the shock strength is increased.

The shift in equilibrium composition due to shock strength is primarily due to the change in

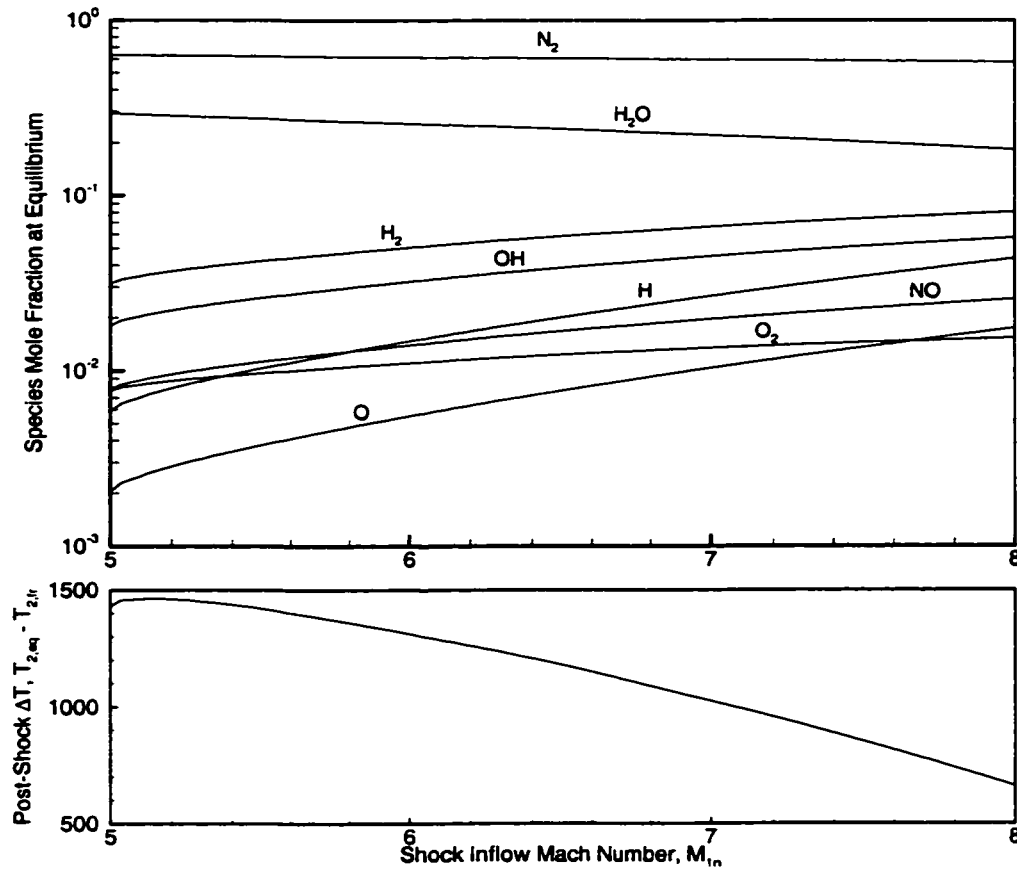


Figure 2.7: Example plots showing effect of shock strength on equilibrium radical populations and temperature in shock-induced combustion. Upper panel: species mole fraction at equilibrium. Lower panel: corresponding post-shock temperature increase, $\Delta T = T_{2,eq} - T_{2,fr}$. Gas mixture: stoichiometric H_2 -air ($2 H_2 + O_2 + 3.76 N_2$). $T_1 = 280$ K, $P_1 = 1.0$ atm.

temperature behind the shock. Note the exponential dependence on temperature for K_p in Eq. 2.24. However, because many of the reactions in a combustion problem are not equimolar (Eq. 2.23 for example), the equilibrium composition is also dependent on the final pressure behind the shock. This is evident if we multiply Eq. 2.24 through by $p_{tot}^* = p_{tot}/p_0$, giving

$$K_p p_{tot}^* = \frac{(p_{H_2O}^*/p_{tot}^*)}{(p_H^*/p_{tot}^*)(p_{OH}^*/p_{tot}^*)} = \frac{\chi_{H_2O}}{\chi_H \chi_{OH}} \quad (2.25)$$

where χ_i is the mole fraction of species i . Thus, an increase in the total pressure of the system will tend to cause an increase in the equilibrium mole fraction of water. An example plot showing the effect of pressure on the final equilibrium composition of stoichiometric H_2 -air combustion is shown in Fig. 2.8. As before, the calculations were performed using CET-89, assuming fixed initial

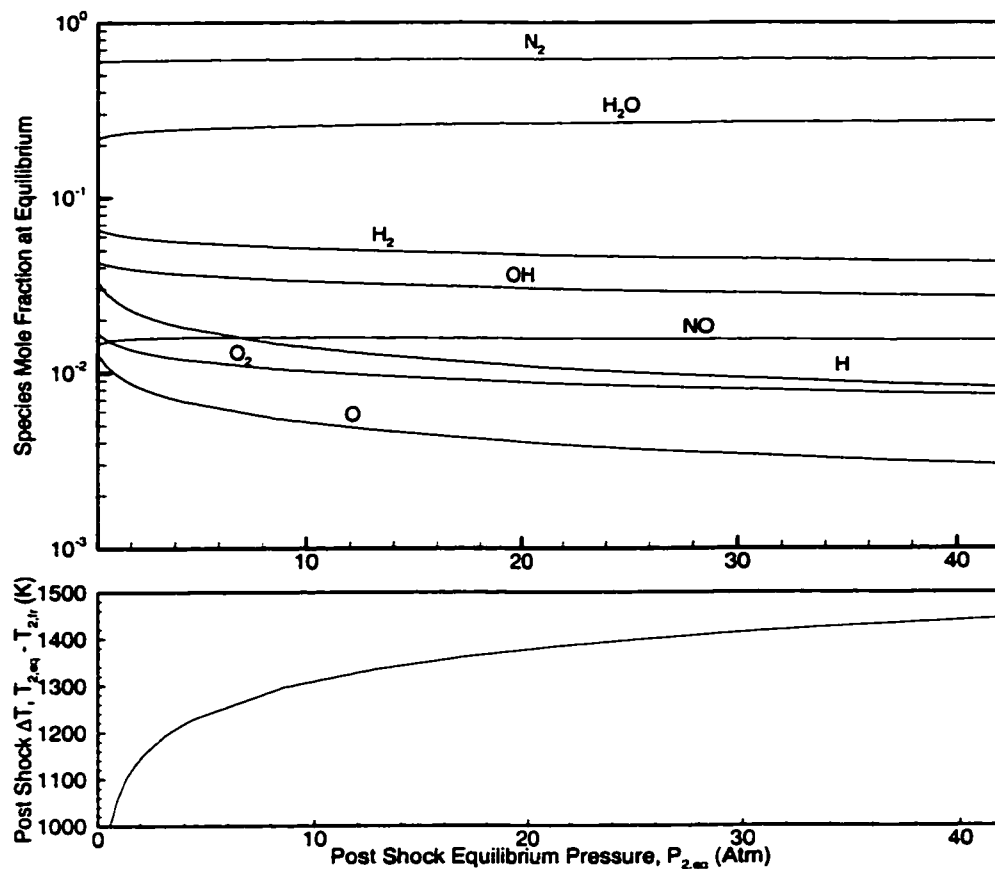


Figure 2.8: Example plots showing effect of pressure on equilibrium radical populations and temperature in shock-induced combustion. Upper panel: species mole fraction at equilibrium. Lower panel: corresponding post-shock temperature increase, $\Delta T = T_{2,eq} - T_{2,fr}$. Gas mixture: stoichiometric H_2 -air ($2 H_2 + O_2 + 3.76 N_2$). $T_1 = 280$ K, $V_{1n} = 2500$ m/s.

$T_1 = 280$ K, and shock inflow velocity of $V_{1n} = 2500$ m/s. The initial pressure was varied from $P_1 = 0.1$ to 10 atm; the results are plotted as a function of the final post-shock pressure. Observe that, as the pressure is increased, the equilibrium mole fraction of H_2O increases while that of the reactants H_2 and O_2 , and radicals such as H , O , OH and NO decreases. Thus the post-shock temperature change due to combustion also increases significantly at higher pressures.

These calculations make it clear that the post-shock equilibrium composition of realistic combustion products is a complex function of both temperature and pressure. The constant- \bar{Q} assumption used previously, if based on lower temperature, atmospheric pressure data, can seriously overestimate the effective energy release at higher Mach numbers or lower pressures.

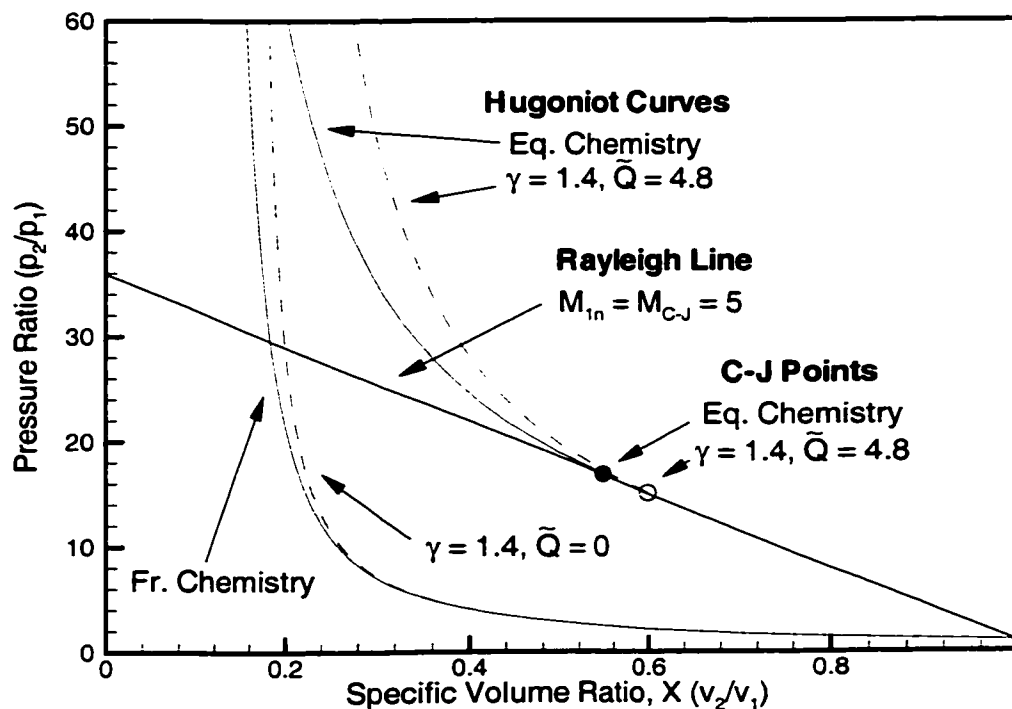


Figure 2.9: Example Rankine-Hugoniot diagram showing solutions for a frozen-chemistry shock, and for a shock with instantaneous equilibrium chemistry. Gas mixture: stoichiometric H_2 -air ($2H_2 + O_2 + 3.76N_2$). $T_1 = 280$ K, $P_1 = 1.0$ atm. For comparison, equivalent constant- γ ($\gamma = 1.4$), and constant- \bar{Q} ($\bar{Q} = 0$ and $\bar{Q} = 4.8$) curves are shown as dashed lines. $M_{C-J} = 5$ in both cases.

2.3.3 Effect on Hugoniot and Shock Polar Diagrams

Having discussed two of the most important aspects of real thermochemistry which affect gasdynamic calculations at high temperatures, we now move on to the practical effects of these phenomena on the Hugoniot and shock polar diagrams used in analyzing oblique shock and detonation flows. For the purpose of comparison with ideal theory, the following calculations were performed assuming stoichiometric H_2 -air at $T_1 = 280$ K, and $P_1 = 1.0$ atm. This example gas mixture and condition was used previously in Fig. 2.7, but more importantly has a Chapman-Jouguet Mach number of 5. This Mach number is identical to that of the ideal $\gamma = 1.4, \bar{Q} = 4.8$ system studied previously in this chapter. Since the Chapman-Jouguet speed is directly related to the energy content of the mixture (Eq. 2.15), this provides the basis of a reasonable comparison. Throughout Figs. 2.9, 2.10 and 2.11, the frozen and equilibrium calculations using real thermochemistry are shown as solid lines, while the ideal theory curves are shown in dashed style.

We first turn our attention to the effects of vibrational excitation on the frozen Hugoniot and shock polar curves. As described previously, the primary effect on the shock wave calculations is the reduction in γ at higher temperatures. Recall that a fixed shock inflow Mach number corresponds to a fixed slope of the Rayleigh line on the Hugoniot diagram, and that larger inflow velocities increase the slope of the line. The Rayleigh line in Fig. 2.9 corresponds to the C-J condition, $M_{1n} = 5$. Examining Eq. 2.13, we see that the reduction in γ decreases the value of the specific volume ratio, X , for a given shock inflow Mach number. The phenomenon may be seen by comparing the frozen and ideal inert curves, both in blue, along the Rayleigh line in Fig. 2.9a. Note also that, typically, the pressure ratio, p_2/p_1 , is not strongly affected by the change in γ . By the ideal gas law, $T_2/T_1 = X(p_2/p_1)$. Consequently, if we account for vibrational excitation, the post-shock temperature is reduced compared to what it would be if γ remained constant at 1.4.

The decrease in specific volume ratio also means that the post-shock density, ρ_2 , is higher than in the ideal inert case. By conservation of mass, Eqn. 2.3, the relative increase in ρ_2 must be accompanied by a relative decrease in the post-shock velocity normal to the wave, u_{2n} . This has the effect, as shown in Fig. 2.10, of increasing the flow turning angle for a particular shock angle on the frozen curve.

The combined effects of vibrational excitation and non-ideal energy release can be seen by comparing the ideal energy release and equilibrium chemistry curves, shown in red, in the figures. It is evident that the combination of both effects leads to more pronounced deviations from ideal theory than was the case for vibrational excitation alone in the ideal inert and frozen chemistry cases. As may be seen from the Rankine-Hugoniot plot (Fig. 2.9), the equilibrium chemistry curve has a significantly lower specific volume ratio than the ideal energy release case at a fixed shock inflow Mach number (i.e. along a particular Rayleigh line). Note that this difference becomes increasingly pronounced for shock strengths higher than the C-J condition. As explained previously, this decrease in specific volume ratio leads directly to a relative decrease in the final post-shock temperature and a relative increase in the final density compared to the ideal energy release case. Thus, the equilibrium chemistry curve on the shock polar diagram (Fig. 2.9) has a correspondingly larger range of flow turning angles. In practical terms, vibrational excitation and equilibrium chemistry effects may be thought of as endothermic processes which consume part of the heat of combustion and counter the normal effects of energy release on the Hugoniot and polar diagrams.

These effects may also be seen by comparing the equilibrium and ideal energy release curves in Fig. 2.11. The maximum and minimum wedge turning angles permitting an attached oblique detonation are both comparatively higher for the equilibrium case. The range of available turning angles between the maximum and minimum values is also larger, particularly at the higher Mach

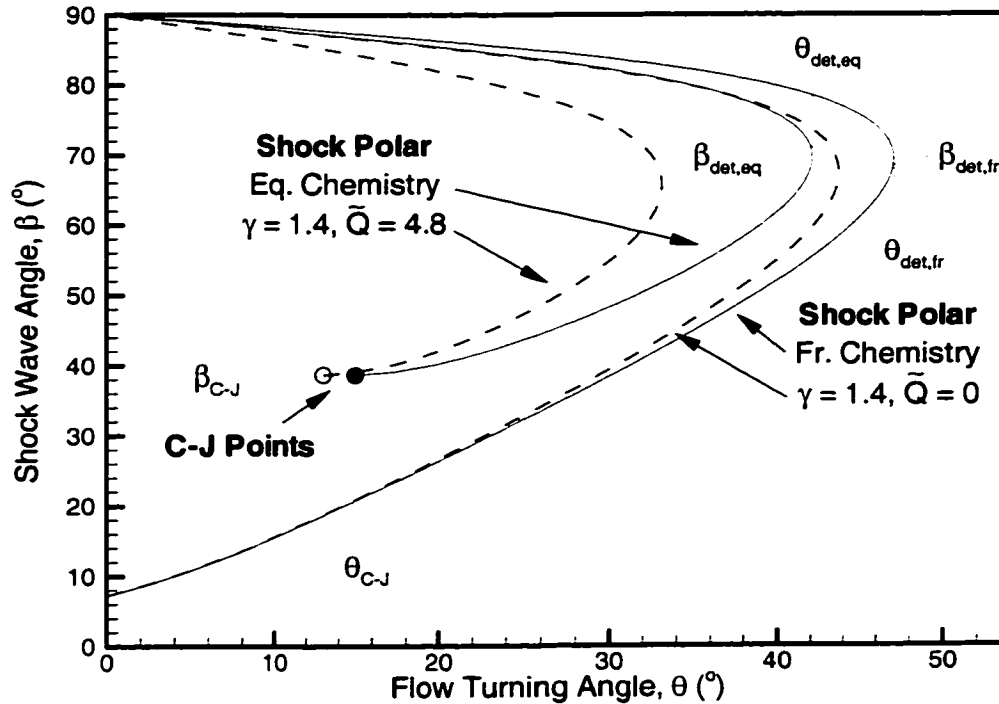


Figure 2.10: Example shock polar diagram showing solutions for a frozen-chemistry shock, and for a shock with instantaneous equilibrium chemistry. Gas mixture: stoichiometric H_2 -air ($2\text{H}_2 + \text{O}_2 + 3.76\text{N}_2$). $T_1 = 280\text{ K}$, $P_1 = 1.0\text{ atm}$, $M_1 = 8$. For comparison, equivalent constant- γ ($\gamma = 1.4$), and constant- \bar{Q} ($\bar{Q} = 0$ and $\bar{Q} = 4.8$) curves are shown as dashed lines. $M_{C-J} = 5$ in both cases.

numbers.

2.4 Finite-Rate Chemistry and Energy Release Behind a Shock Wave

Thus far in our analysis, whether the energy release process was modeled as a simple constant- \bar{Q} model, or as a more realistic mixture of reactant species which proceeds to equilibrium, we have assumed that this process has occurred instantaneously across the oblique shock wave. In some scenarios, particularly at very high enthalpy conditions, the equilibrium calculation will accurately model what occurs in nature. However, in many situations, the conversion of the initial gas mixture composition to the final equilibrium state will occur over finite timescales which can not be conveniently ignored in predicting the resultant flowfield. In this section, we first describe a simple, 0-dimensional, constant-volume H_2 - O_2 ignition problem. This is done with the view of illustrating the two significant timescales in the problem. We next turn to finite-rate ignition and energy release

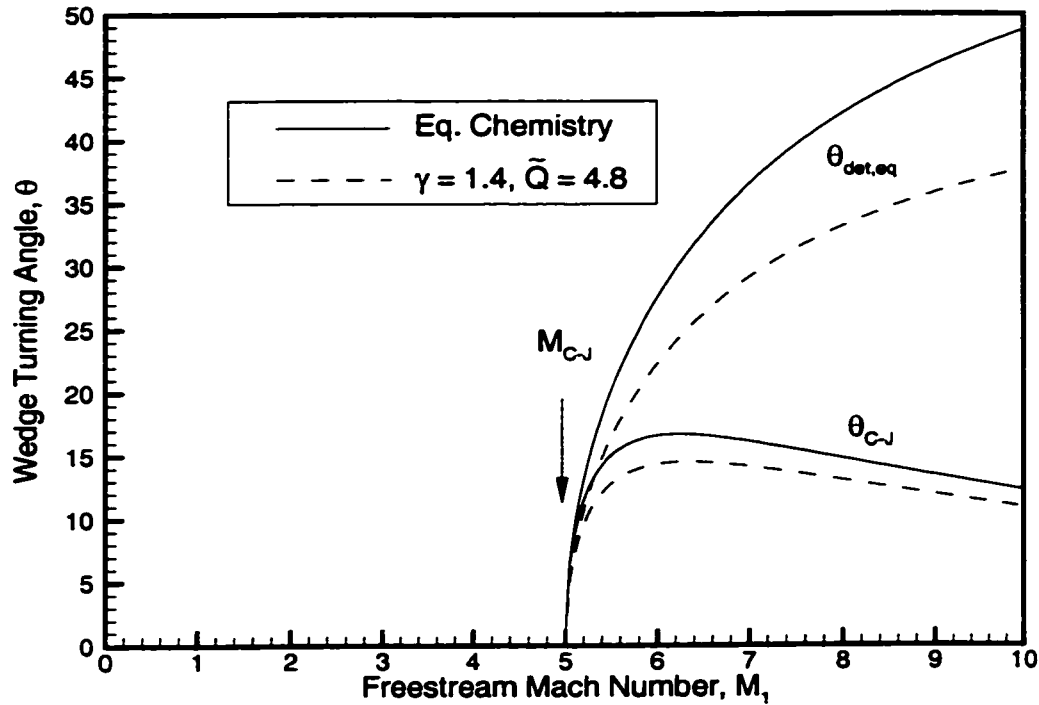


Figure 2.11: Example plot showing effect of freestream Mach number on the maximum ($\theta_{\text{det},q}$) and minimum (θ_{C-J}) wedge turning angles which will permit an attached exothermic shock solution. Gas mixture: stoichiometric H_2 -air ($2\text{H}_2 + \text{O}_2 + 3.76\text{N}_2$). $T_1 = 280\text{ K}$, $P_1 = 1.0\text{ atm}$. For comparison, equivalent constant- γ ($\gamma = 1.4$), and constant- \tilde{Q} ($\tilde{Q} = 0$ and $\tilde{Q} = 4.8$) curves are shown as dashed lines.

behind a normal shock wave using the ZND model, and finally describe the extension of this model to a straight oblique detonation wave.

2.4.1 H_2 - O_2 Ignition and Energy Release

Typically, when a combustible gas mixture is suddenly heated to high temperature, the ignition process can be thought of having two significant timescales: an initial induction phase where combustion radicals such as H, OH and O are rapidly formed from the initial reactants, and an energy release phase in which these radicals combine to form combustion products such as H_2O . This behavior is evident in Fig. 2.12, which shows the time history for the constant-volume ignition of stoichiometric H_2 -air at $T_{\text{ini}} = 1500\text{ K}$, $P_{\text{ini}} = 1.0\text{ atm}$. This plot was generated by integrating the 9 species, 18 reaction mechanism published by Petersen and Hanson (1999) (see Appendix B), using

the stiff-ODE solver routine developed for this study. Note the explosive growth in the populations of H, O, OH, and H₂O during the induction phase. This is primarily due to chain-branching reactions such as $\text{H} + \text{O}_2 \rightarrow \text{OH} + \text{O}$ and $\text{O} + \text{H}_2 \rightarrow \text{OH} + \text{H}$ which increase the number of radicals available each time they occur. Due to the exothermic nature of H₂O formation, once significant quantities of water are formed the temperature of the system increases rapidly. Both HO₂ and H₂O₂ are also shown; they are important in governing H₂-O₂ ignition behavior at higher pressures and lower temperatures.

Throughout this analysis, we shall often make reference to two (somewhat arbitrarily defined) timescales which for convenience are depicted on the temperature history plot. We define the characteristic ignition timescale, τ_{ign} , as the interval between $\tau = 0$ and the point at which the change in temperature has reached 1% of the total change from the initial to the final state. This timescale is also sometimes called the induction time. The characteristic equilibration timescale, τ_{equil} , we shall define from $\tau = \tau_{\text{ign}}$ to the point at which the change in temperature has reached 99% of the total change. The induction time is, in general, considerably shorter than the equilibration timescale.

2.4.2 Finite-Rate Chemistry in a 1-D Normal Shock Flow

We now extend our study to consider ignition and energy release behind a normal shock wave. We will treat the problem as entirely 1-dimensional. It should be noted that, in many cases, this is a considerable idealization: C-J detonation waves often have a complex, multi-dimensional structure which includes cellular features and transverse waves. Nevertheless, the classic 1-D ZND model, so named from Zel'dovich, von Neumann, and Döring who developed it independently during World War II, represents the basic theory for understanding ignition and energy release behind a shock wave. The following is a general description of this model. A more extensive explanation of this (and other) detonation models is provided in Fickett and Davis (1979).

A schematic of the flow, in a reference frame in which the shock is stationary, is shown in Fig. 2.13. Proceeding from left to right in the figure, we have initially an unreacted gas (state 1) which flows into shock wave. The model assumes that, as shock waves are typically only a few mean-free-paths thick, there are negligible reactions which occur across the shock. Thus the gas immediately behind the shock, though at an elevated temperature and pressure, has the same chemical composition as that at state 1 (i.e., it is chemically frozen). If the temperature of state 2 is high enough, the radical populations will thereafter increase rapidly. Once a significant quantity of water has been formed the temperature will rapidly increase and the reactions will proceed to chemical equilibrium. Note that we have assumed here that vibrational excitation occurs significantly faster

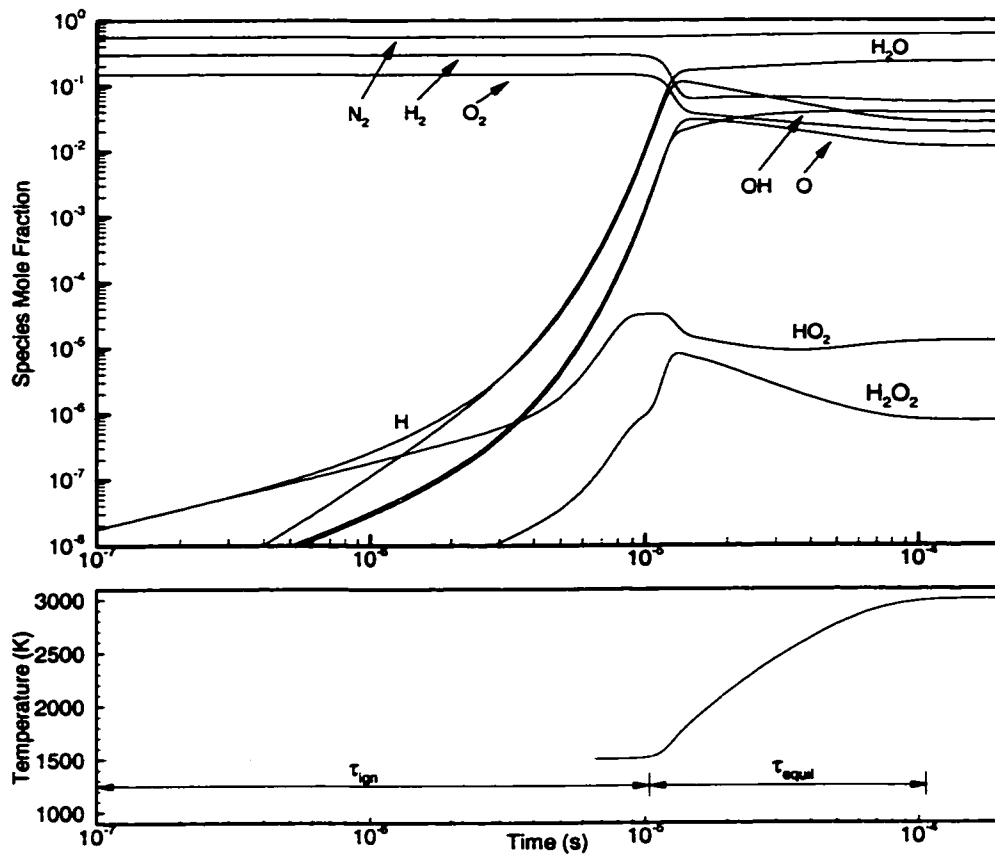


Figure 2.12: Example plots showing species (upper panel) and temperature (lower panel) history for the constant-volume ignition of stoichiometric H_2 -air ($2\text{H}_2 + \text{O}_2 + 3.76\text{N}_2$). Initial conditions: $T_{\text{ini}} = 1500\text{ K}$, $P_{\text{ini}} = 1.0\text{ atm}$. τ_{ign} defined as point (from $\tau = 0$) when $\Delta T = 0.01\Delta T_{\text{tot}}$. τ_{equil} defined as point (from $\tau = \tau_{\text{ign}}$) when $\Delta T = 0.99\Delta T_{\text{tot}}$

than the relevant chemical timescales in the flowfield, and that the gas is effectively in thermal equilibrium throughout the flowfield. In this steady-flow model, the concept of an induction time behind the shock, τ_{ign} , is often interchanged freely with a characteristic ignition lengthscale, often termed the induction zone, where $L_{\text{ign}} \simeq \tau_{\text{ign}}\mu_{2,\text{fr}}$. In similar fashion, the chemical equilibration zone on the diagram can be thought of as equivalent to the characteristic equilibration timescale defined in the previous subsection.

The essential difference between combustion behind a shock and other scenarios, such as a constant-pressure process in an atmospheric flame, or a constant-volume process in a combustion bomb, is that in the case of shock-induced combustion the gas velocity forms an important contribution to the total enthalpy of the flow. There exists a close coupling between the velocity of the

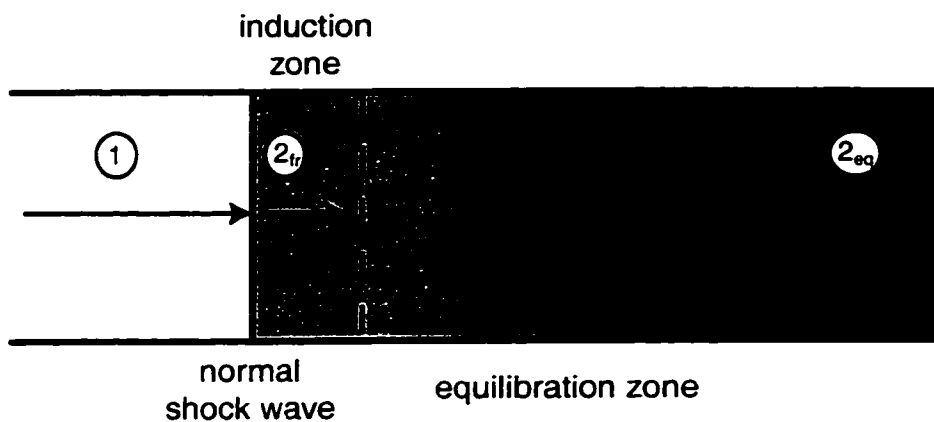


Figure 2.13: Schematic of 1-D reaction zone structure in a normal detonation wave.

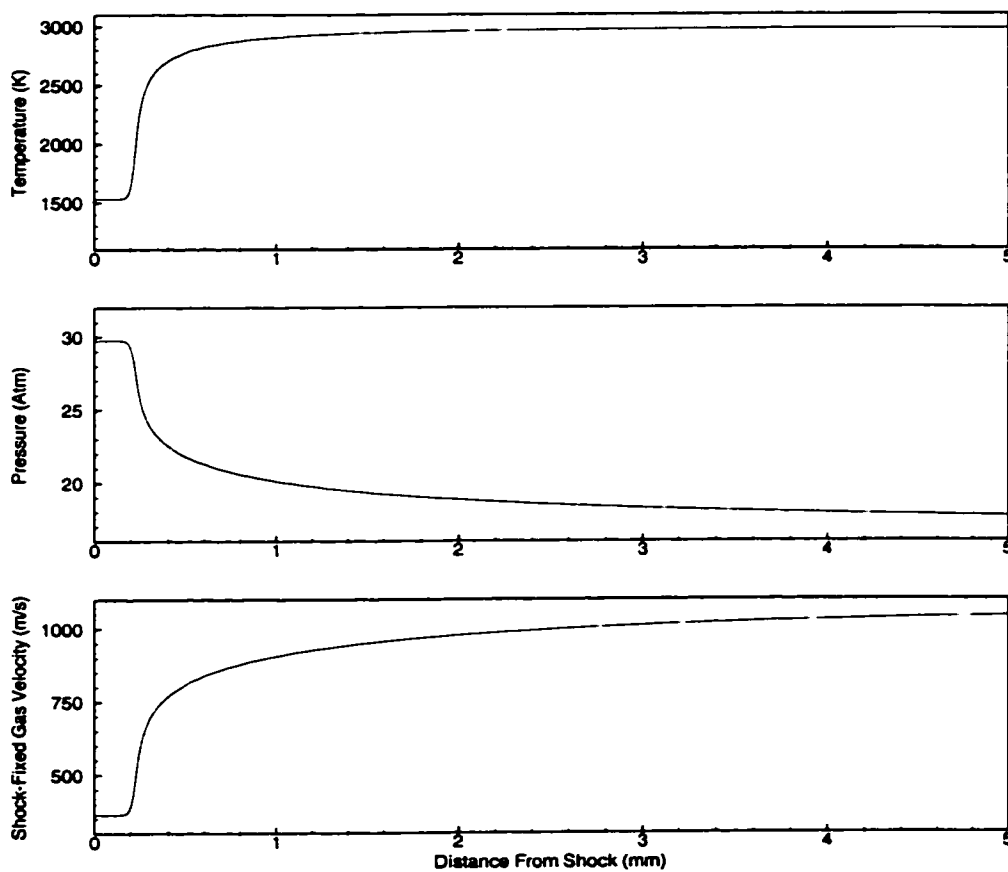


Figure 2.14: Computed 1-D reaction zone structure in a normal C-J detonation wave. Gas mixture: stoichiometric H_2 -air ($2 H_2 + O_2 + 3.76 N_2$). $T_1 = 280$ K, $P_1 = 1.0$ atm, $u_1 = 1980$ m/s.

gas behind the shock and the changes in temperature and pressure as the reactions proceed to equilibrium. This behavior is evident when we examine the computed 1-D reaction zone structure for a H_2 -air detonation wave (Fig. 2.14). This profile was computed using the program SHOCK (Mitchell and Kee, 1982), which is included in the CHEMKIN-II (Kee et al., 1989) package. Initial conditions were $T_1 = 280 \text{ K}$, $P_1 = 1.0 \text{ atm}$, $u_1 = 1980 \text{ m/s}$. Observe that the temperature, pressure and gas velocity are essentially fixed throughout the induction zone immediately behind the shock wave (located at the origin of the figure). Once significant energy release takes place, both the temperature and gas velocity (in the shock-fixed reference frame) steadily increase while the pressure decreases from the initial (frozen) post-shock state. The relative increase in temperature and decrease in pressure results, by the ideal gas law, in a relative decrease in gas density through the equilibration zone. This decrease in density is also consistent with the increase in gas velocity by conservation of mass. The thermodynamic process pathline for the conversion of the reactants behind the shockwave to products at the equilibrium state is easier to visualize on a Rankine-Hugoniot diagram. Frozen and equilibrium shock Hugoniot curves, along with the Rayleigh line for these initial conditions, are shown in Fig. 2.15. The computed reaction zone data points from Fig. 2.14 are also plotted on the diagram. The points fall initially at the intersection point between the Rayleigh line and the computed frozen shock Hugoniot curve. The reaction zone points then proceed along the Rayleigh line toward the equilibrium Hugoniot curve, and terminate at the C-J point on the diagram.

2.4.3 Extension to a Straight Oblique Detonation Wave

The extension of the ZND model to a straight oblique detonation wave is rather straightforward. A schematic of the ZND model applied to a straight oblique detonation at angle β is shown in Fig. 2.16. Recall from our previous discussion earlier in this chapter that the jump conditions across an oblique shock can be calculated by using 1-D normal shock theory and substituting the velocity component normal to the wave as the relevant inflow velocity parameter. Furthermore, we found that for a straight oblique wave the velocity component tangential to the wave was unchanged across the shock. In similar fashion, it can be shown that there is translational invariance if we include the ZND reaction structure behind a straight oblique shock. The problem then again reduces to a 1-D ZND calculation using the velocity component normal to the oblique wave as the inflow velocity. The constant tangential velocity may then be superimposed to produce the flowfield behind the oblique wave. A more extensive description of this analysis and reduction is contained in the review article by Shepherd (1994).

Observe in Fig. 2.16 that the gas initially emerges from the shock in the induction zone at the angle given by relevant frozen shock polar, θ_{fr} . The flow angle essentially remains constant at θ_{fr}

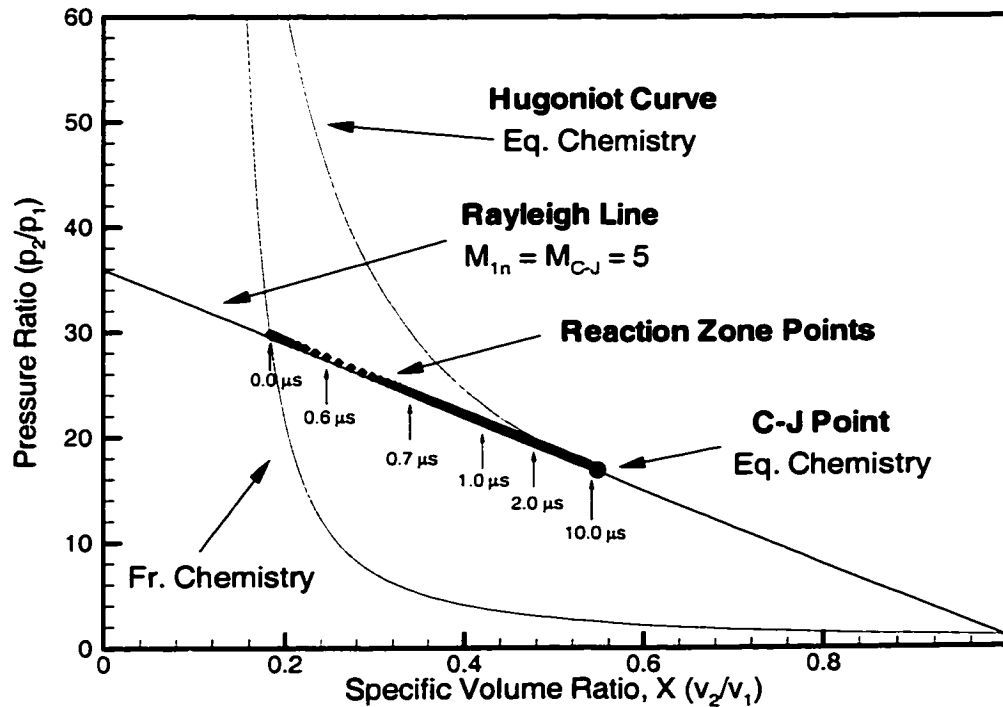


Figure 2.15: Example Rankine-Hugoniot diagram showing solutions for a frozen-chemistry shock, and for a shock with instantaneous equilibrium chemistry. Reaction zone points are computed for a 1-D C-J detonation wave. Time scale referenced on the diagram is particle time from passage through the shock. Gas mixture: stoichiometric H_2 -air ($2 H_2 + O_2 + 3.76 N_2$). $T_1 = 280$ K, $P_1 = 1.0$ atm.

throughout the induction zone, then decreases once energy release begins in the equilibration zone. Recall from our previous discussion of the ZND model in a 1-D shock flow that the gas velocity (in a shock-fixed reference frame) increased in the equilibration zone. Thus, since the tangential velocity is constant, this increase in the velocity component normal to the wave results in a decrease in the flow angle as the reactions proceed to equilibrium. This process is shown graphically in the example shock polar diagram in Fig. 2.17. The computed reaction zone data points for a stoichiometric H_2 -air C-J oblique detonation wave at an angle of $\beta = 38.8^\circ$ are shown. Freestream conditions are $T_1 = 280$ K, $P_1 = 1.0$ atm, $M_1 = 8$. The computed reaction points were obtained using SHOCK with the geometric transformation handled by post-processing. As expected, the flow angle behind the shock initially intersects the frozen shock curve and then rapidly decreases to intersect the C-J point on the equilibrium curve.

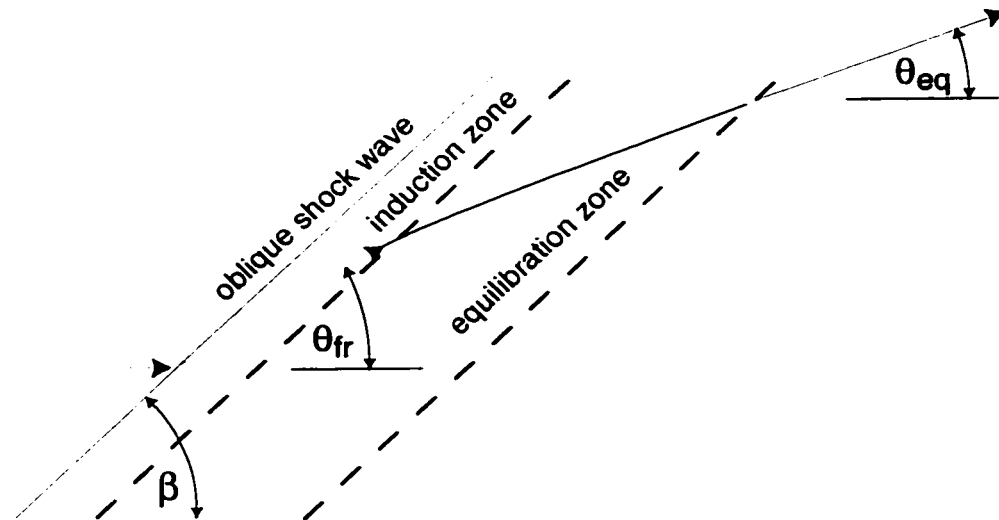


Figure 2.16: Schematic of ZND reaction zone structure in a straight oblique detonation wave.

2.5 Finite-Rate Chemistry in Supersonic Wedge Flow

We now turn to the practical problem of generating an oblique detonation wave using a wedge introduced into a uniform flow of a combustible gas mixture. We will first provide a generalized description of the flow in order to provide the framework for a more detailed discussion using a finite-rate chemistry CFD code developed by the author.

2.5.1 Generalized Description

The introduction of finite-rate chemistry introduced critical time- and length-scales into the ignition and energy release behind a shock wave. Any physical wedge body will similarly introduce a relevant flow lengthscale into the problem. As shown in Fig. 2.18, one way of describing the possibilities which may occur in these flows is to compare the chemical and flow lengthscales for a particular case. In our discussion here, we shall define the relevant flow lengthscale as length of the wedge forebody from the tip of the wedge to the edge of the expansion corner. The chemical lengthscale is defined as the ignition length along the wedge surface, i.e., from the wedge tip to the onset of the reaction front (if any) on the forebody. In most situations, this ignition lengthscale can be calculated based on the post-shock conditions for a frozen polar curve oblique shock solution. It should be noted that, at very high flow enthalpies, compressible boundary layer growth at the wedge tip may require a more sophisticated analysis of the ignition lengthscale than the simplified analysis presented here. It is also important to note that (as discussed in section 2.2) the freestream Mach number in this discussion must be greater than the C-J detonation velocity of the combustion

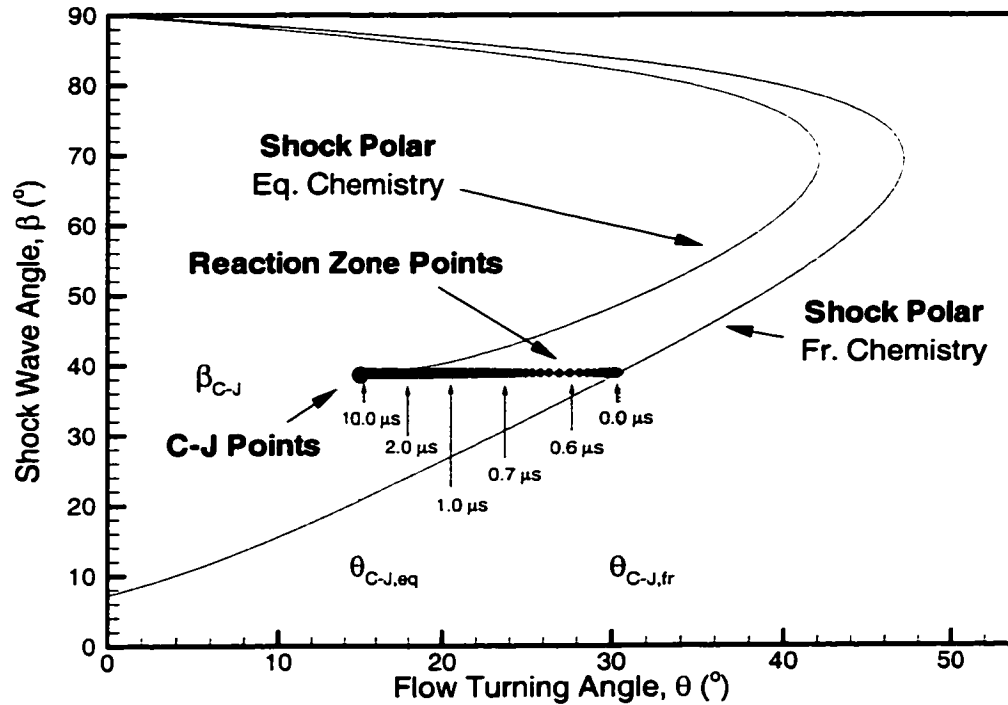


Figure 2.17: Example shock polar diagram showing solutions for a frozen-chemistry shock, and for a shock with instantaneous equilibrium chemistry. Reaction zone points are computed for a 1-D C-J oblique detonation wave at an angle of $\beta = 38.8^\circ$. Time scale referenced on the diagram is particle time from passage through the shock. Gas mixture: stoichiometric H_2 -air ($2\text{H}_2 + \text{O}_2 + 3.76\text{N}_2$). $T_1 = 280\text{ K}$, $P_1 = 1.0\text{ atm}$, $M_1 = 8$.

gas mixture ($M_1 > M_{C-J}$). Moreover, we are initially considering only wedge angles in the range permitting both frozen and equilibrium shock solutions ($\theta_{C-J} < \theta < \theta_{\text{det,eq}}$). Thus we would expect the flow to remain supersonic throughout and evolve to a steady solution.

The first case we consider is one in which the chemical ignition length is longer than the flow lengthscale. Logically, in this case the oblique shock remains at the frozen oblique shock angle throughout the flow until it encountered the rarefaction fan radiating from the expansion corner.

The next case we consider is perhaps the most interesting: when the chemical ignition length is less than, but of roughly the same order as, the flow lengthscale, a mixed flow situation develops. In this case, moving from the wedge tip toward the expansion corner, the oblique shock is initially at the frozen shock angle. However, once the gas mixture begins to burn along the wedge surface, the thermodynamic changes in the gas state will influence the oblique shock via Mach waves. If the burned gas evolves relatively slowly toward equilibrium, we expect the wave angle to similarly

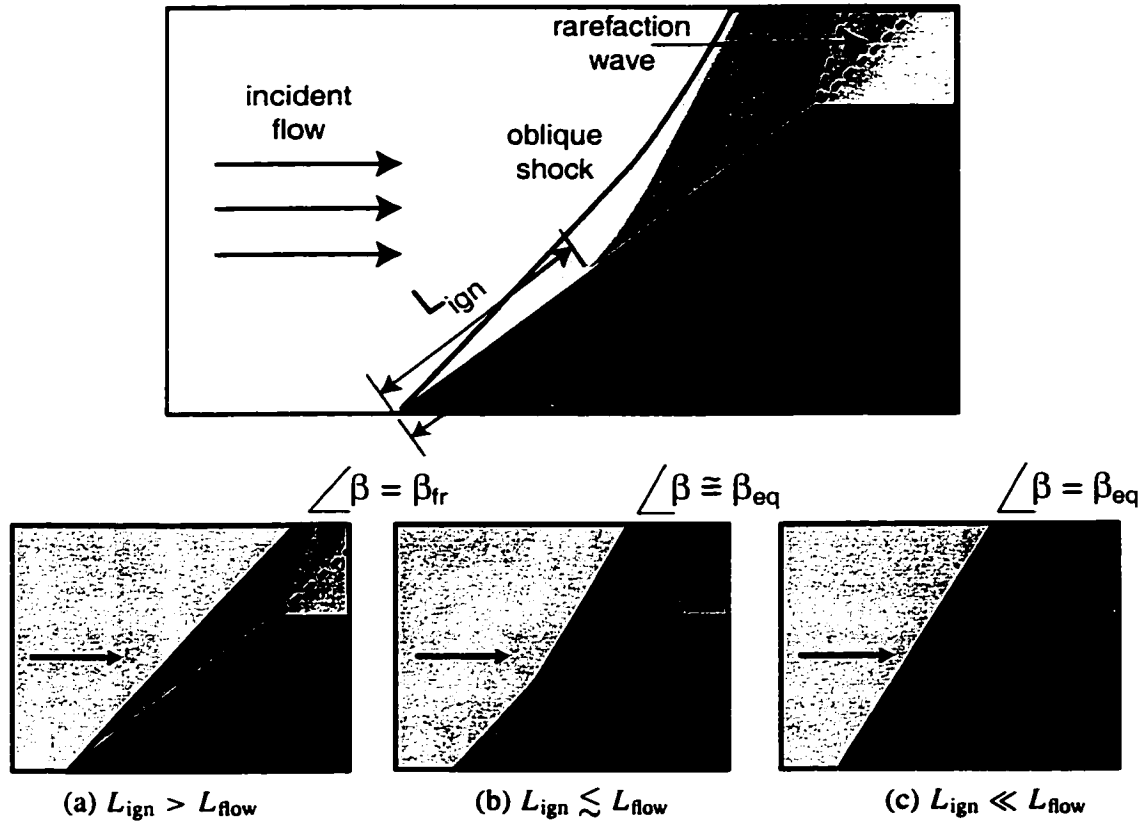


Figure 2.18: Generalized description of possibilities for supersonic wedge flow with a combustible gas mixture. Note: Freestream Mach number $M_1 > M_{C-J}$, Wedge angle θ limited by $\theta_{C-J} < \theta < \theta_{det,eq}$. (a) Oblique shock (fr. solution), no reaction front (b) Oblique shock (fr. solution) followed by reaction front, transition to oblique detonation (eq. solution) (c) Oblique detonation (eq. solution)

change slowly, and may not reach the equilibrium wave angle within the flowfield region. On the other hand, if the burned gases evolve relatively quickly toward equilibrium, the shock will consequently also change rather quickly to the equilibrium shock solution. It is evident even at this general level, then, that in addition to the chemical ignition length, a relevant equilibration lengthscale is also critical in determining the particular features of this flow case.

The last case considered is one in which the chemical ignition length is much shorter than the flow lengthscale. In this case, after a small frozen shock and transition zone near the wedge tip, we naturally expect the shock to rapidly develop into a fully-coupled oblique detonation wave which asymptotes to the equilibrium oblique shock angle throughout the remainder of the flowfield.

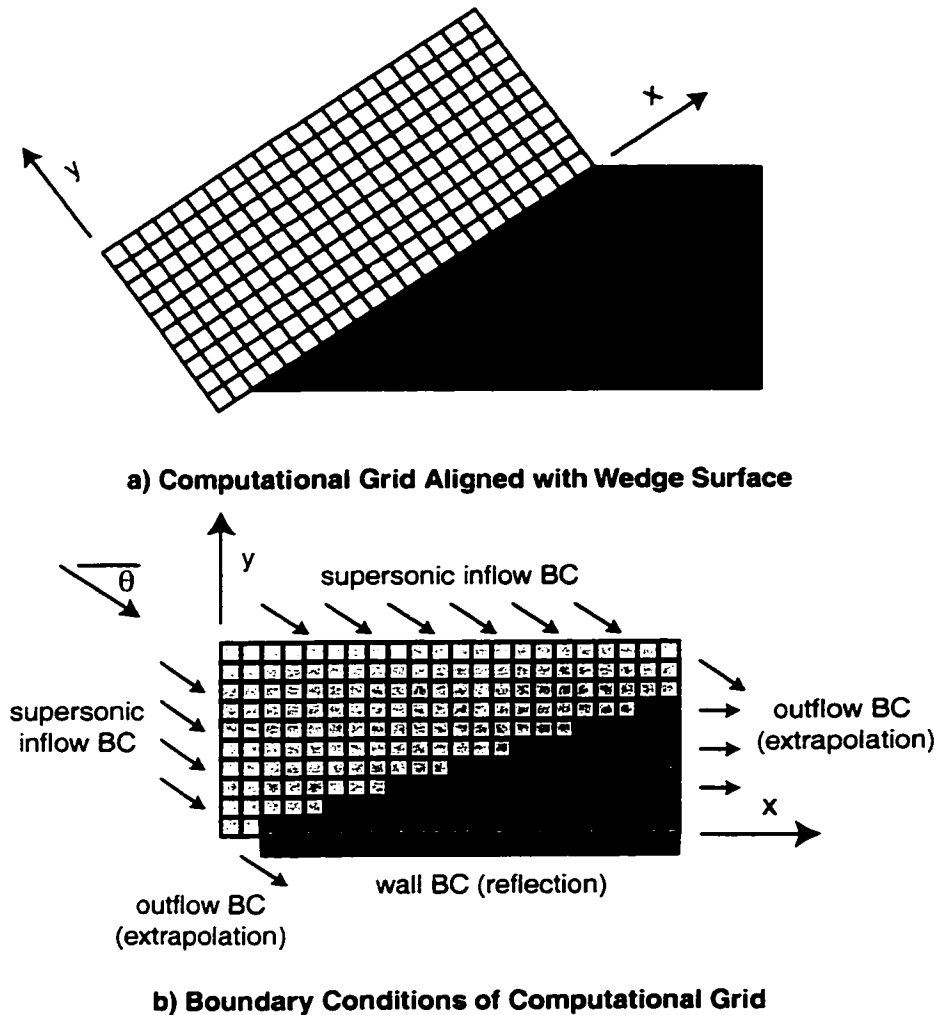


Figure 2.19: (a) Schematic of computational grid aligned with the wedge surface. (b) Schematic of boundary conditions of the computational grid.

2.5.2 Finite-Rate Chemistry CFD Calculations

In order to obtain a more detailed understanding of oblique shock-induced combustion and detonation waves generated by a wedge body, we turn to a finite-rate chemistry CFD code developed by the author. A general overview of the approach is given here.

As shown in Fig. 2.19, the code utilizes a finite-volume Cartesian grid which is aligned with the inclined forebody of the wedge. The reference frame is rotated so that the problem essentially becomes an inclined flow (at angle $-\theta$) impinging on a flat plate. The grid cells are uniformly spaced (Δx and Δy are both constant) though Δx and Δy are not necessarily the same value. It can be argued that a polar grid radiating from the wedge tip would be more appropriate for inert

oblique shock flows, as shock smearing and numerical diffusion would be reduced compared to the Cartesian grid. However, this study focuses on flows involving energy release, which introduces variations in the shock angle throughout the flowfield, as well as potential time-dependence. Therefore, unless coupled with an adaptive algorithm, a polar grid would also exhibit numerical diffusion and smearing across the shock. Even under ideal conditions (1-D grids), calculations of strong shocks involving real thermochemistry using modern shock-capturing methods (Montagné et al., 1988) will smear the shock over several grid points. It was judged to leave development of adaptive grid algorithms in the code to future development.

Ghost cells are utilized to specify the boundary conditions in the problem. Supersonic inflow boundary conditions are used along both upstream boundaries (left-hand and upper boundaries in the figure). Simple zeroth-order extrapolation is used as the outflow boundary condition on the right-hand downstream boundary and on the bottom edge before the surface. This boundary condition works well when the outflow is supersonic, a condition generally true throughout this study. A standard reflection boundary condition is specified along the wedge surface. Note that the grid extends a few cells (typically 10) beyond the wedge tip in order to clearly capture the oblique shock at that location.

The code utilizes a 1st-order time-step splitting approach where the fluid and finite-rate chemistry solvers are called as separate subroutines. In the 1st-order approach, each complete time-step involves calling each subroutine once. Thus, in operator notation, the solution U at time-step $n + 1$ is

$$U^{n+1} = \mathcal{L}_f^{\Delta t} \mathcal{L}_c^{\Delta t} U^n \quad (2.26)$$

where \mathcal{L}_f represents the fluid solver and \mathcal{L}_c represents the finite-rate chemistry solver. The time-step splitting approach allows both high-quality fluid and chemical solvers to be developed and tested independently, and then joined together in relatively straightforward fashion. As described by Oran and Boris (1987), the time-step splitting approach works well when relatively small time-steps are used. Since the global time-step in the present code is strictly limited by the explicit Courant-Friedrichs-Lewy (CFL) condition, this is not thought to be a problem. Moreover, most of the cases we examine will be steady flows in which the time-dependent solution has been allowed to evolve into the steady-state. In this case, the problems that a time-step splitting approach may have with a rapidly evolving solution are not an issue.

The fluid solver used here is a 2nd-order accurate (in time and space) Harten-Yee symmetric-TVD algorithm (Yee, 1989). The solver employed Roe's approximate Riemann solver modified for nonequilibrium ideal gases (Grossman and Cinnella, 1990). It also incorporates suggestions by Larroutourou (1991) to ensure species positivity. The ideal gas thermodynamic fits of McBride et al.

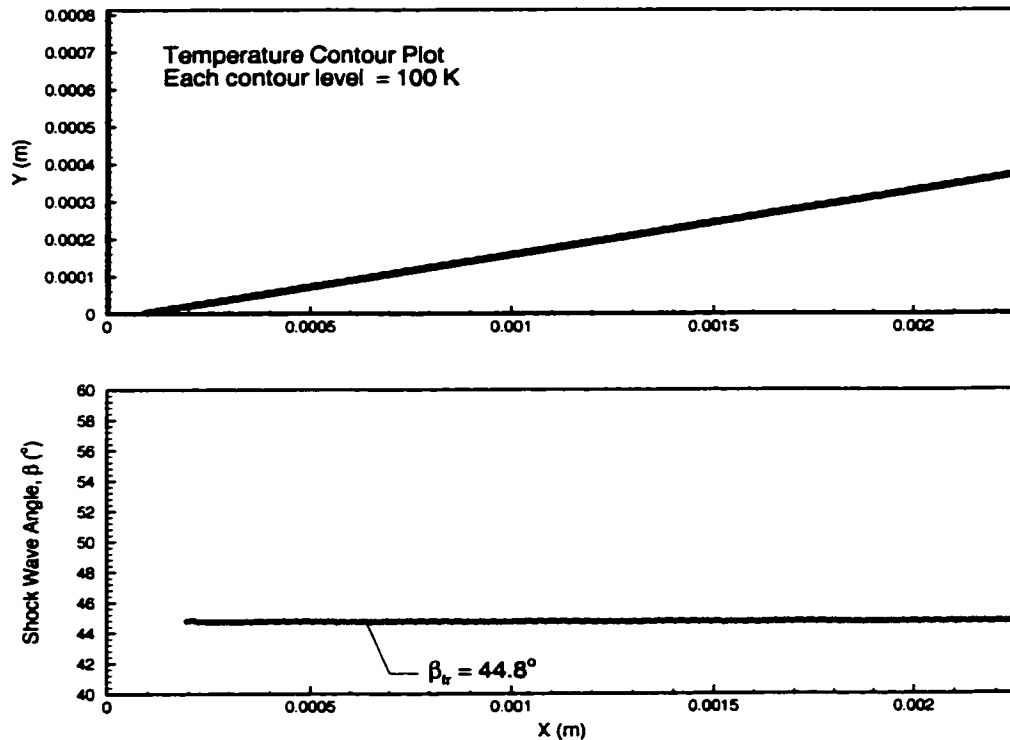


Figure 2.20: Converged CFD simulation of stoichiometric H_2 -air ($2\text{H}_2 + \text{O}_2 + 3.76\text{N}_2$) flow over a $\theta = 35^\circ$ wedge. $T_1 = 280\text{ K}$, $P_1 = 0.125\text{ atm}$, $M_1 = 8$. $\Delta x = 0.01\text{ mm}$, $\Delta y = 0.005\text{ mm}$. Upper panel: temperature contour plot. Lower panel: corresponding plot of shock wave angle as a function of grid x-coordinate.

(1993) are used for the 9 species in the problem (N_2 , O_2 , H_2 , OH , H_2O , H , O , HO_2 , and H_2O_2 are included). See Appendix A for a listing of the thermodynamic model data.

The chemical solver utilizes the reduced 18-reaction H_2 - O_2 ignition mechanism published by Petersen and Hanson (1999). The mechanism is described in detail in Appendix B. As with most chemical kinetics problems, the time-integration of this mechanism requires a stiff-ODE solver to ensure accuracy. The method used here is Newton-Rhapson iteration of a linearized implicit trapezoidal scheme. Typically, convergence to acceptable accuracy is achieved within 1-2 iterations at each time-step.

2.5.3 Example CFD Calculations

We will now apply this code to the study of several example cases, using the standard stoichiometric H_2 -air test condition used previously in this chapter. This brief study is done with the view of both confirming our generalized synopsis from earlier in this section, and also illustrating the basic

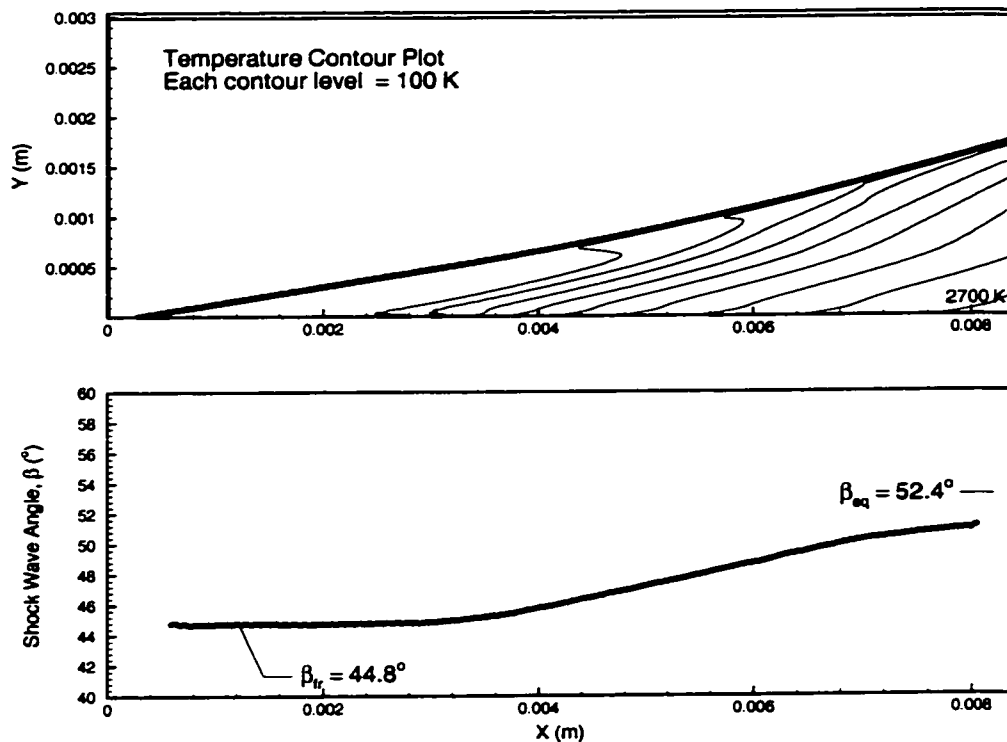


Figure 2.21: Converged CFD simulation of stoichiometric H_2 -air ($2\text{H}_2 + \text{O}_2 + 3.76\text{N}_2$) flow over a $\theta = 35^\circ$ wedge. $T_1 = 280\text{ K}$, $P_1 = 0.125\text{ atm}$, $M_1 = 8$. $\Delta x = 0.03\text{ mm}$, $\Delta y = 0.015\text{ mm}$. Upper panel: temperature contour plot. Lower panel: corresponding plot of shock wave angle as a function of grid x-coordinate.

features of the flow in more detail.

The first test case given is of stoichiometric H_2 -air flow over a $\theta = 35^\circ$ wedge. Freestream conditions are $T_1 = 280\text{ K}$, $P_1 = 0.125\text{ atm}$, $M_1 = 8$. The domain studied was an area $2.24\text{ mm} \times 0.80\text{ mm}$ (224×160 , $\Delta x = 0.01\text{ mm}$, $\Delta y = 0.005\text{ mm}$). A temperature contour plot, and a corresponding plot of shock wave angle for the converged CFD solution are shown in Fig. 2.20. As is evident from the figure, no ignition took place along the wedge surface in this particular case. Therefore, this solution can be thought of as an example of the $L_{\text{ign}} > L_{\text{flow}}$ case described above. Note that both plots confirm that the shock wave is straight and steady at the frozen shock polar angle of 44.8° throughout the flowfield.

A test run using the same freestream conditions over a larger domain (280×200 , $\Delta x = 0.03\text{ mm}$, $\Delta y = 0.015\text{ mm}$) is shown in Fig. 2.21. As before, the shock wave angle is initially at the frozen polar value near the wedge tip. Note however that in this case the temperature contour plot clearly shows ignition in this case, the reaction front starting roughly one-quarter of the distance

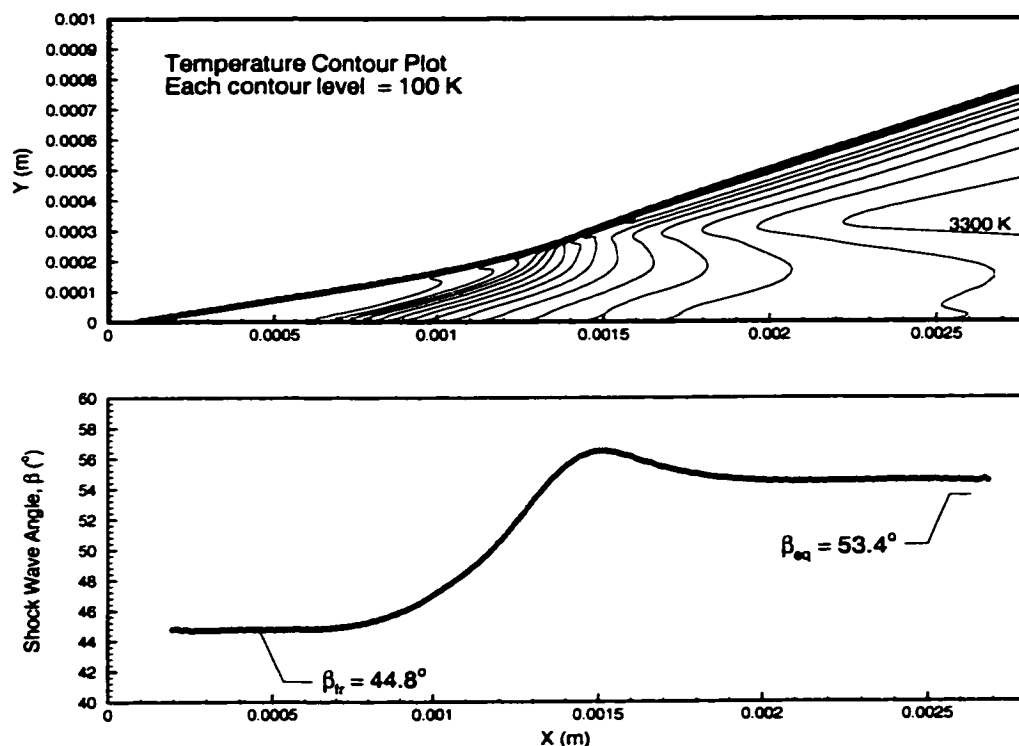


Figure 2.22: Converged CFD simulation of stoichiometric H_2 -air ($2 \text{H}_2 + \text{O}_2 + 3.76 \text{N}_2$) flow over a $\theta = 35^\circ$ wedge. $T_1 = 280 \text{ K}$, $P_1 = 0.5 \text{ atm}$, $M_1 = 8$. $\Delta x = 0.01 \text{ mm}$, $\Delta y = 0.005 \text{ mm}$. Upper panel: temperature contour plot. Lower panel: corresponding plot of shock wave angle as a function of grid x -coordinate.

across the domain. The energy release behind the oblique shock gradually increases the shock angle toward the equilibrium shock polar value of 52.4° throughout the flowfield. However, it is evident that, in this particular case, this steepening process is relatively slow and the shock does not reach the equilibrium value within the domain. This solution then corresponds to the mixed flow case where $L_{\text{ign}} \lesssim L_{\text{flow}}$. The equilibration lengthscale for this case is evidently somewhat larger than L_{flow} .

Another example of the mixed flow scenario occurs when using the same gas mixture, freestream temperature and velocity, but increasing the freestream pressure by a factor of four to $P_1 = 0.5 \text{ atm}$. This case (Fig. 2.22) is computed using a domain similar to (though slightly larger than) that of the first case: 280×200 , $\Delta x = 0.01 \text{ mm}$, $\Delta y = 0.005 \text{ mm}$. Similar to our previous example, the reaction front starts roughly one-fifth of the distance across the domain. However, the temperature contours in this case clearly indicate that the burned gases approach the equilibrium state much more rapidly. The reaction front rapidly steepens and merges with the shock wave, driving the wave angle

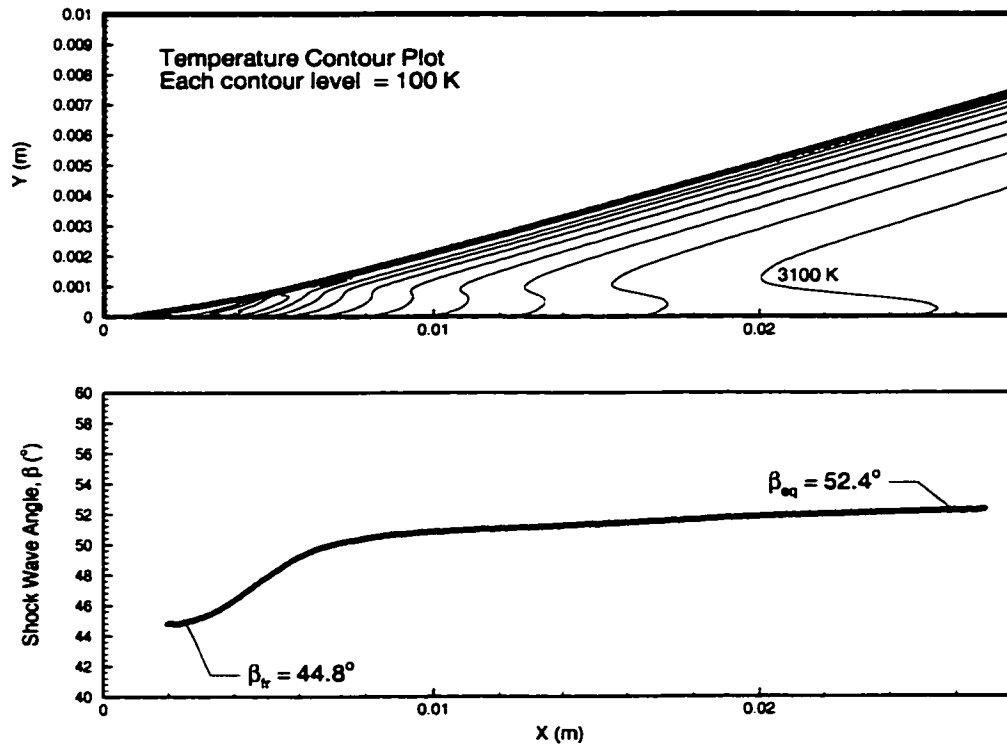


Figure 2.23: Converged CFD simulation of stoichiometric H_2 -air ($2 \text{H}_2 + \text{O}_2 + 3.76 \text{N}_2$) flow over a $\theta = 35^\circ$ wedge. $T_1 = 280 \text{ K}$, $P_1 = 0.125 \text{ atm}$, $M_1 = 8$. $\Delta x = 0.1 \text{ mm}$, $\Delta y = 0.05 \text{ mm}$. Upper panel: temperature contour plot. Lower panel: corresponding plot of shock wave angle as a function of grid x -coordinate.

above even the equilibrium polar value. Note also that the temperature contours in the upper-right of the figure align parallel with the steepened shock. This behavior is consistent with the steady, straight oblique detonation wave model presented earlier in this chapter. Clearly, the increase in freestream pressure here has dramatically reduced the relative size of the equilibration lengthscale.

Our final two examples increase the domain size further in order to illustrate the case where $L_{\text{ign}} \ll L_{\text{flow}}$. The solution in both Fig. 2.23 ($P_1 = 0.125 \text{ atm}$, 280×200 , $\Delta x = 0.1 \text{ mm}$, $\Delta y = 0.05 \text{ mm}$) and Fig. 2.24 ($P_1 = 0.5 \text{ atm}$, 280×200 , $\Delta x = 0.03 \text{ mm}$, $\Delta y = 0.015 \text{ mm}$) are dominated by well-formed oblique detonation waves. In Fig. 2.23, the relatively slow equilibration rate (at lower pressure) drives the detonation wave angle to the equilibrium polar value of 52.4° only at the rightmost edge of the domain. The higher freestream pressure in Fig. 2.24 drives the wave to the equilibrium polar value of 53.4° relatively quickly. The parallel temperature contours behind the detonation wave are again consistent with the ZND model discussed previously.

To summarize, these examples confirm the basic features of the simple analysis presented earlier

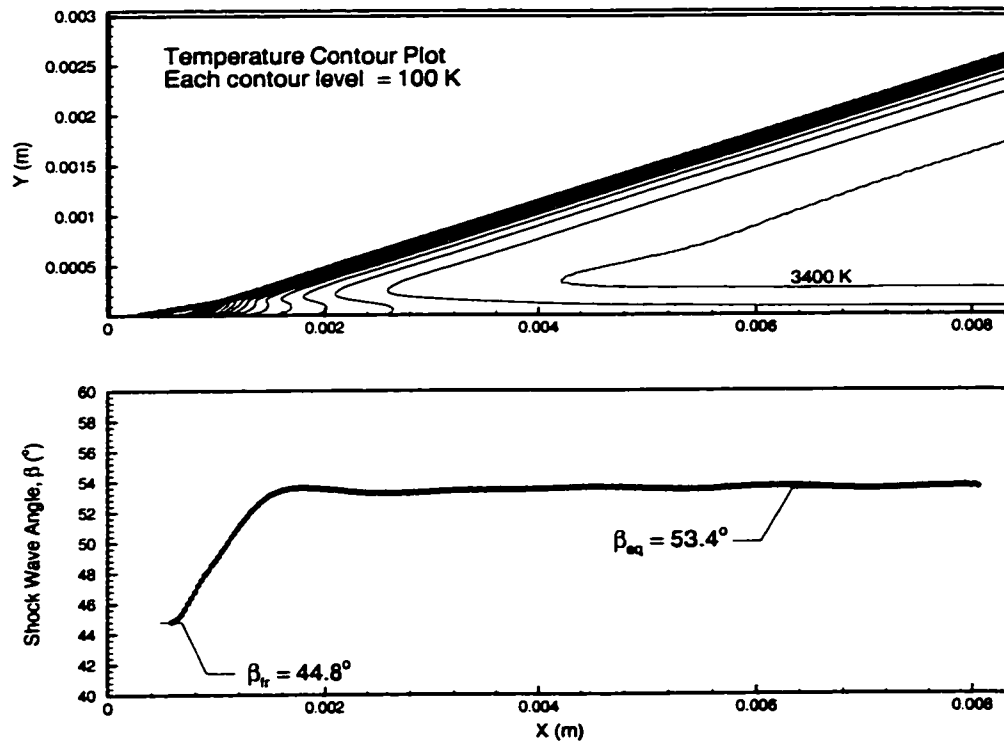


Figure 2.24: Converged CFD simulation of stoichiometric H_2 -air ($2\text{H}_2 + \text{O}_2 + 3.76\text{N}_2$) flow over a $\theta = 35^\circ$ wedge. $T_1 = 280\text{ K}$, $P_1 = 0.5\text{ atm}$, $M_1 = 8$. $\Delta x = 0.03\text{ mm}$, $\Delta y = 0.015\text{ mm}$. Upper panel: temperature contour plot. Lower panel: corresponding plot of shock wave angle as a function of grid x-coordinate.

in this section, while simultaneously hinting that the details of the transition from a frozen oblique shock wave to an oblique detonation are complicated, and strongly dependent on the mixture sensitivity. These CFD results also confirm that, in the limiting cases of $L_{\text{ign}} > L_{\text{flow}}$ and $L_{\text{ign}} \ll L_{\text{flow}}$, the wave angle corresponds to the appropriate curves on the shock polar diagram (accounting for real thermochemistry). It is important to state, however, that the results presented here are for one particular freestream condition and wedge angle. Chapter five will analyze the impact of these parameters on the flowfield in much greater detail.

Chapter 3

Experimental Apparatus

As was described in the Introduction, one method of obtaining experimental data on oblique shock-induced combustion and detonation waves is to fix a wedge or conical test body in the laboratory reference frame, and use a hypersonic test facility to produce a stream of combustible gases around the model. This is the approach which has been taken in this work. An expansion tube facility was designed and built in the High Temperature Gasdynamics Laboratory at Stanford University in order to generate the combustible test flow. Additionally, Planar Laser-Induced Fluorescence (PLIF) and schlieren imaging systems were installed to obtain flow visualization data around the model.

This chapter is split into two sections. The first section provides an overview of the idealized theory of expansion tubes and a description of the specific expansion tube facility at Stanford. A brief discussion of real expansion tube effects is also provided, along with a description of the methods used to characterize the test flow generated by this facility. The second section briefly summarizes the theory of PLIF and describes the schlieren/PLIF imaging system used in these experiments.

3.1 Expansion Tube Facility

This section provides an overview of the expansion tube facility used in this work. The idealized theory of expansion tubes is given first, in order to provide background for the description of the specific Stanford facility which follows. A brief discussion of real expansion tube effects is also provided, as well as an explanation of the methods used to characterize the test flow.

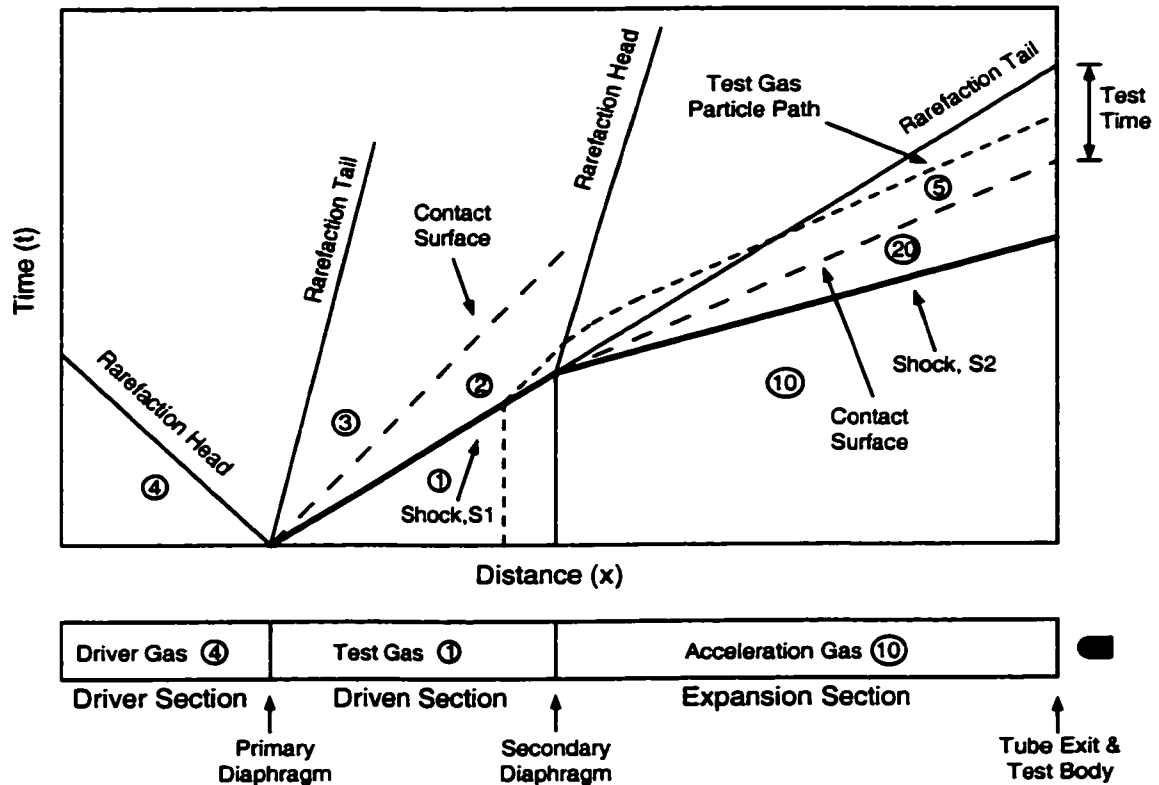


Figure 3.1: X-t wave diagram and schematic of an expansion tube. Gas states are summarized as follows: 1 = initial condition of test gas in driven section, 4 = initial condition of driver gas, 3 = expanded driver gas, 2 = post-shock condition of the test gas, 5 = expanded test gas, 10 = initial condition of acceleration gas in expansion section, 20 = post-shock condition of acceleration gas.

3.1.1 Expansion Tube Theory

An expansion tube is an impulse flow device used to generate short-duration, high-velocity gas flows. The device generally consists of three sections of tubing aligned in tandem, and may be thought of as a conventional shock tube with an additional stage attached on the downstream end. Thin plastic or metal diaphragms are used to isolate the sections from each other. The driver section is initially filled to high pressure with a light gas such as helium. The driven section is filled to a lower pressure with the test gas of interest. The third section of tubing, named expansion section, contains a light gas (again typically helium) at very low pressure. The expansion section gas is also sometimes known as the acceleration gas. A detailed description of expansion tube theory can be found in Trimpi (1962).

The 1-D, unsteady gasdynamics of shock and expansion tubes are often visualized with the aid of an x-t wave diagram (Fig. 3.1). As shown in the figure, the x-axis represents distance along the

tube, while the y-axis represents the temporal evolution of the experiment. The first stage of an expansion tube is very similar to a shock tube. When the driver/driven (primary) diaphragm is broken at $t = 0$, the high-pressure driver gas expands into the lower-pressure driven section. A shock wave is formed which propagates into the test gas, inducing an increase in temperature, pressure, and density behind it. The shock also induces an intermediate (lab-reference frame) velocity in the test gas. Thus, for moderate-to-strong shocks, state 2 is characterized as a supersonic ($M_2^{(\text{lab})} \simeq 1 - 2$), high temperature gas flow. Note also on the diagram that there is a contact surface separating the test gas from the driver gas. The contact surface is often idealized as a pure discontinuity between two different gases, though in reality real diaphragm effects and diffusion tend to smear the surface over a short length of the flow.

When the primary shock reaches the end of the driven section, it breaks the driven/ expansion (secondary) diaphragm, and accelerates upon entering the expansion section. The shock wave now induces an increased pressure, density, temperature and velocity in the acceleration gas. Meanwhile, the previously shocked test gas (state 2) is simultaneously cooled and accelerated by an unsteady, constant-area expansion from the driven section into the lower-pressure expansion section. State 5 is thus a relatively high Mach number, low temperature gas flow. A sample particle path for the time history of a test gas molecule is also shown in the figure. Again, there is a contact surface which separates the test gas from the acceleration gas.

It is important to understand the flow history at the exit of the tube. An observer at that location would first witness the arrival of the secondary shock wave, S2, and then a steady flow period of acceleration gas (state 20). At a certain point, a contact surface will appear which signals the arrival of the test gas at the exit. The subsequent uniform flow period of the test gas at state 5 is known as the test time. The end of the test time is limited by unsteady expansion waves which are carried downstream from the secondary diaphragm station.

Reflected-type shock tunnels are another commonly used method of obtaining high-enthalpy flows. In a shock tunnel, the downstream end of the shock tube is closed off so that the primary shock reflects off the end wall. This creates a very high temperature and pressure stagnation region next to the wall. A small hole in the end wall opens into a 2-D or axisymmetric nozzle, through which the stagnant test gas can expand to high velocity. Two critical performance factors in any impulse facility are the enthalpy of the test flow, and the length of the test time. Expansion tubes have a comparative advantage in that they can theoretically generate high-enthalpy flows without exposing the test gas to a high-temperature stagnation condition. The high-temperature stagnation region in a shock tunnel can lead to undesirable dissociation effects, or auto-ignition in a combustible test gas. The latter danger is of great concern for the experiments here, since it is critical that the

combustible test gas in our experiments be safely accelerated without pre-ignition inside the tube. It is fair to point out, however, that reflected-type shock tunnels typically have significantly longer test times than expansion tubes. Thus, expansion tubes have mainly found employment for accelerating combustible gas mixtures, and for studying extremely high-enthalpy flows such as super-orbital velocity re-entry problems.

3.1.2 Description of the Facility

As shown in Fig. 3.2, the Stanford expansion tube is comprised of four sections of tubing. The purposes of the driver, driven and expansion sections have been described previously. The driver is constructed on T304 stainless steel (10.2 cm I.D., 12.7 cm O.D.) and is 1.829 m in length. The driven and expansion sections are both constructed of T6061 aluminum (8.9 cm I.D., 12.7 cm O.D.) and are 2.743 m and 4.267 m in length respectively. One modification to the standard expansion tube design is the buffer section, a 91.4 cm length of tubing (with the same specifications as the driven and expansion sections) installed between the driver and driven sections. The buffer, isolated via diaphragms, is typically filled with an inert gas such as N_2 to the same pressure as the driven section. This serves to isolate the combustible test gas in the driven section from the relatively violent rupture of the primary diaphragm at the start of the experiment. The entire assembly is mounted on casters stabilized by a 6.35 m length aluminum I-beam. The driver, buffer and expansion sections are free to roll on the casters and thus move along the axis of the tube. This facilitates the removal of old diaphragms and the installation of new diaphragms before each experiment. The driven section is fixed in place.

An additional refinement is the use of a double diaphragm section, an assembly of inserts shrouded by a short 17.8 cm length of stainless tubing. The inserts in the double diaphragm section, combined with two diaphragms, allow a small 393 cm^3 evacuable volume to be created in between the driven and buffer sections. The purpose of this section is to allow for firing of the facility on command. The diaphragms are selected to break at a pressure greater than one-half of, though not exceeding, the desired fill pressure of the driver. When loading the facility, the intermediate volume is then filled with helium to one-half of the driver pressure. Thus, the pressure difference across each diaphragm is initially less than that needed to break each diaphragm. At the start of the experiment, the intermediate volume is vented to the exhaust system, causing both diaphragms to break and allowing the high-pressure driver gas to expand into buffer and driven sections.

Downstream of the expansion section, a square viewing chamber of 27×27 cm cross section is mounted to a 356 liter dump tank which acts as a receiver for the gas flow during the experiment. The front of the viewing chamber is equipped with an access port and o-ring to allow the expansion

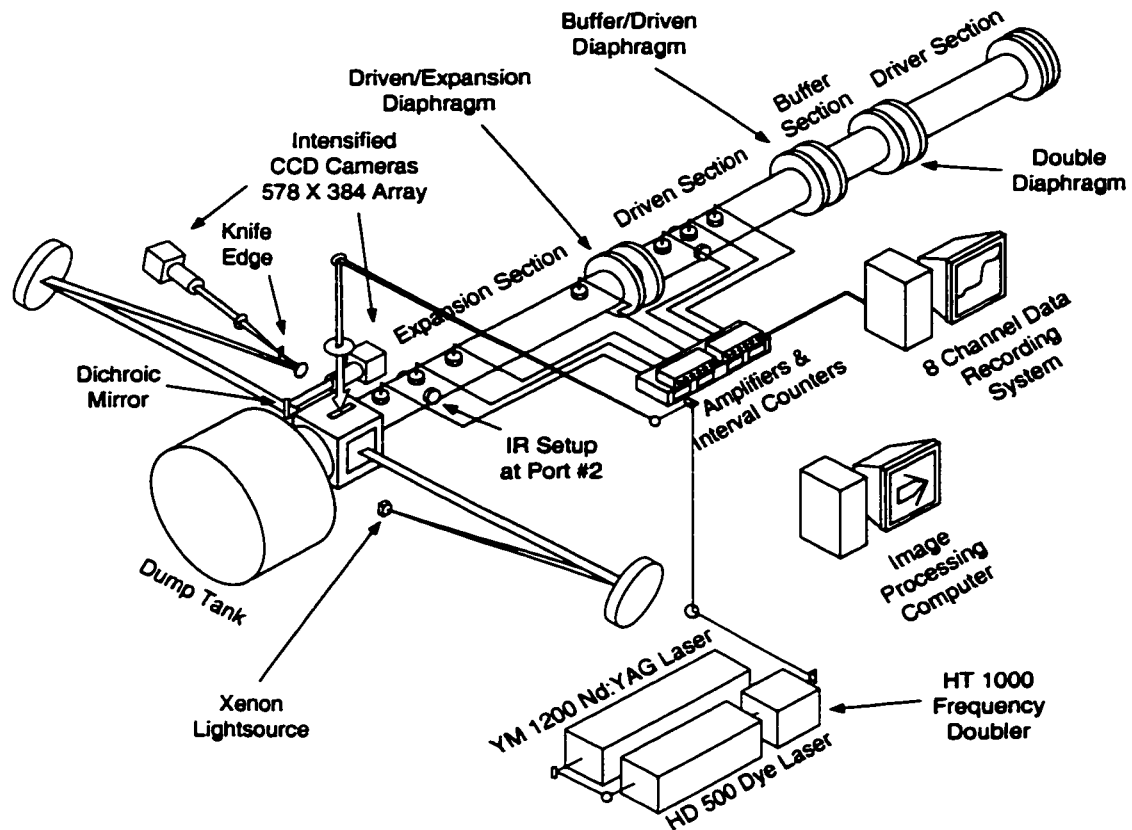


Figure 3.2: Schematic of expansion tube facility and optical arrangement used for simultaneous OH PLIF and schlieren imaging of reactive flows.

section to slide inside the viewing chamber. The exterior of the final 10.2 cm on the downstream end of the expansion section has been honed to enable a vacuum-quality seal with the o-ring in the access port. The test body is mounted downstream of the exit of the expansion section, inside the viewing chamber. The chamber is equipped with an opposed pair of square (13×13 cm) quartz windows for observation, and a fused silica window on top of the chamber for admission of the laser sheet for PLIF imaging.

A number of pumps are employed to evacuate the facility. A Welch 1397 mechanical roughing pump is used to evacuate the dump tank, viewing chamber, and expansion section. Another Welch pump is used for the driver, buffer, and driven sections. A Varian HS-2/0160 diffusion pump, backed by a Varian SD-200 mechanical pump, is also available for generating a high-quality vacuum in the driven section. A dedicated mixing assembly, consisting of a mixing manifold and a 16.4 liter mixing tank equipped with a magnetic stirrer, is attached to the driven section. A Varian SD-451 mechanical pump directly services the mixing tank. Four thermocouple gauges are installed

throughout the vacuum system to monitor the pressure in each section of the tube. An additional ionization gauge is connected to the driven section for monitoring high-vacuum conditions.

A facility control panel houses the mixing assembly, the diffusion pump, and a number of solenoid valve control switches, pressure gauges and readouts. The filling pressure in the driver and double diaphragm sections are monitored by two Ashcroft test gauges with maximum readings of 1000 psig and 600 psig respectively. Two Setra pressure transducers, each with a range of 0–50 psia, are mounted to monitor the filling pressure in the buffer and driven sections. A Baratron pressure gauge (0–100 torr) measures the pressure in the expansion section, viewing chamber and dump tank.

Both the driven and expansion sections are equipped with sensor access ports. The driven section has five ports spaced at 30.5 cm intervals along the top of the tube, starting 15.2 cm from the downstream end of the section. An additional two ports form a horizontally-opposed pair 45.7 cm from the downstream end. The expansion section is similarly equipped with seven ports along the top, starting 40.6 cm from the downstream end. As was the case in the driven section, an additional two ports form a horizontally-opposed pair 102 cm from the downstream end. PCB 113A26 piezoelectric pressure transducers are installed in plugs in the final three (closest to the downstream end) vertically-oriented ports along the top of each tube. An additional transducer is installed in the first expansion section port, 20.3 cm downstream from the driven/expansion interface, in order to monitor the unsteady expansion process at that location. The transducers measure the dynamic pressure history at each station throughout the experiment. The signals from the transducers are amplified using a PCB 483A08 variable-gain unit, and are connected to an array of four Fluke PM-6666 interval counters. When set with the appropriate trigger voltage, the counters automatically display the time interval for the shock to travel between adjacent stations in the tube. The transducer signals are also digitized and recorded for later analysis using a PC-based array of four Gagescope CS1012 ISA cards, providing eight channels at 12 bits of resolution. The recording speed is typically 1 Msample/s.

The horizontally opposed pair of ports in the expansion section are typically fitted with plugs mounting sapphire windows for IR-emission and absorption measurements during a test run. In this work, IR-absorption of CO₂ seeded into the test gas is employed for measuring the test gas velocity during characterization runs. The IR-setup consists of a Globar light source mounted on one side of the tube, and a focusing lens and Judson J-10 IR-detector mounted on the other side. A concentration of 5% CO₂ (by volume) in the test gas has been found to provide an absorption signal sufficient for accurate determination of the arrival of the test gas at that location. Characterization tests also employ an array of four pitot probes equipped with pressure transducers to measure the

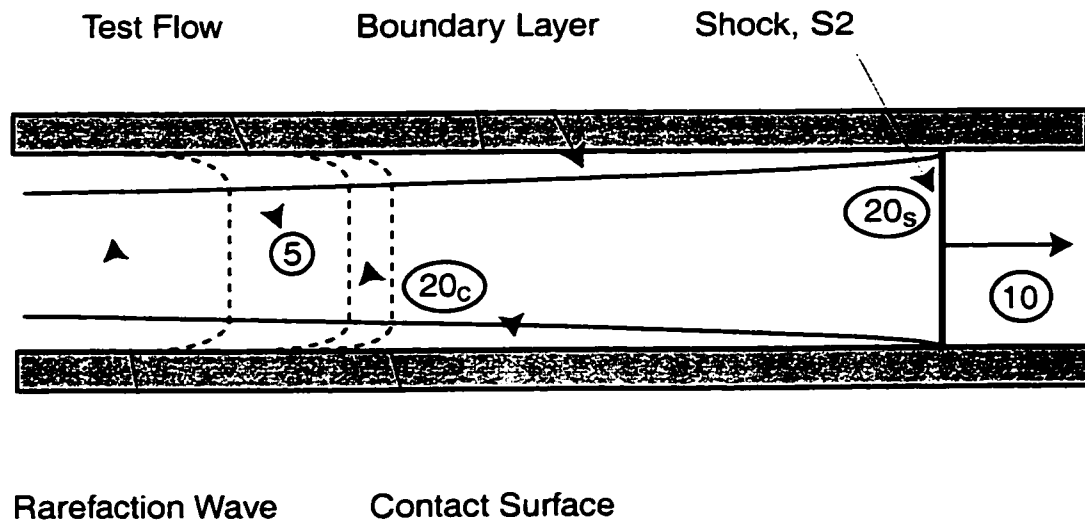


Figure 3.3: Schematic of flow behind the shock wave in the expansion section. 10 = initial condition of acceleration gas in expansion section, 20s = immediate post-shock condition of acceleration gas, 20c = condition of acceleration gas near the contact surface, 5 = expanded test gas.

pitot pressure at the exit of the tube. The use of the IR and pitot measurements to determine the test gas velocity and test time will be explained in further detail below.

3.1.3 Nonidealities in Expansion Tubes

Accurate knowledge of the exit flow pressure, temperature, and velocity are critical in analyzing the results of expansion tube experiments. The idealized, 1-D, constant- γ shock equations and isentropic expansion relations can be used to predict the resultant flow conditions and test times for a particular expansion tube geometry and initial conditions. However, as we have seen previously, real thermochemistry effects can significantly impact the calculated post-shock conditions for di- and polyatomic gases. Moreover, non-ideal diaphragm rupture and boundary layer growth behind the shock wave typically attenuate the shock strength below the value predicted from idealized predictions. Therefore, as will be described in more detail below, the post-shock conditions are calculated using real thermochemistry codes and the experimentally measured shock speeds.

Non-ideal diaphragm rupture and boundary layer growth are problems common to both shock and expansion tubes. However, these factors have a much greater impact on the test condition in expansion tubes than in shock tubes. A schematic of the flow behind the shock in the expansion section is shown in Fig. 3.3. One feature immediately evident from this figure is the fact that the test flow, state 5 in the figure, occurs after the contact surface well behind the shock wave. This is in contrast to most shock tube experiments, where typically the gas immediately following the

shock is of interest. This means that the boundary layer which grows behind the shock wave can have a significant effect on both the acceleration gas and test gas flow conditions. The influence of boundary layer growth on the freestream flow conditions behind a shock wave was analyzed in the classic papers of Mirels (1963, 1964, 1966). The Mirels analysis applies in the limit of very long tubes in which the shock and contact surface have reached their maximum separation. Moreover, it is primarily directed toward the flow nonuniformity of the gas between the shock and contact surface, which is the acceleration gas in our case (state 20s through 20c in the figure). In our experiments, the shock and the contact surface typically do not achieve their maximum separation. Moreover, we are primarily interested in the test flow condition, state 5, as opposed to the conditions in the acceleration gas. However, the Mirels analysis does show that, in the presence of significant boundary layer growth, the freestream gas velocity behind the shock will increase in the laboratory reference frame. Thus, since the relatively low fill pressures used for the acceleration gas do lead to significant boundary layer growth, we measure the velocity of the test gas experimentally in separate flow characterization tests. These issues have been explored in greater detail in numerical studies by Sharma and Wilson (1995). Measurements of test time and comparison with the Mirels theory in the Stanford facility were first reported by Morris et al. (1995), and are summarized briefly below.

Non-ideal diaphragm rupture is also an important factor in expansion tube flows. In an ideal expansion tube, the secondary diaphragm vanishes instantaneously upon impact by the primary incident shock. In our experiments, Mylar diaphragms of the absolute minimum thickness necessary (typically $\leq 25 \mu\text{m}$) to sustain the initial pressure differences are employed. However, the finite mass and breaking-time of any physical diaphragm leads to a brief reflected-shock condition as the diaphragm breaks. The reflected shock decays rapidly as the diaphragm particles are accelerated with the contact surface gases (Bakos and Morgan, 1994). However, as the test gas which evolves into the test flow is located immediately adjacent to the diaphragm, the reflected shock can potentially contaminate the early test flow and reduce the available test time. Additionally, the brief reflected-shock condition can also serve as an ignition source for a combustible test gas mixture. This factor effectively limits the sensitivity of the mixture which may be used, as well as the shock strength in the driven section. In practice, premature ignition can be detected by examination of the shock speed records, wall pressure measurements, and the imaging results.

A third factor which influences the test flow is lateral waves which appear as oscillations in the static and pitot pressure records. These waves are believed to be produced as the driver gas flows through the area change at the double diaphragm. In the model of Paull and Stalker (1999), these lateral oscillations can in some circumstances be transmitted into the test gas, and focused through the expansion fan to produce a dominant frequency in the test flow. The predictions of this theory

agree well with numerical results by Jacobs (1994). Some limited comparisons with this theory and experimental measurements in the Stanford facility are summarized below.

3.1.4 Calculation of Test Flow Conditions

We will now explain in further detail the methods used to calculate the test flow condition for a particular experiment. We turn first to the wall static pressure history recorded by the pressure transducers installed at the three ports closest to the downstream end of both the driven and expansion sections. An example wall pressure record in the expansion section is shown in Fig. 3.4. Note that the wall pressure record clearly shows the shock arrival, followed by a constant pressure flow period, and finally a rarefaction fan which marks the end of steady flow. By measuring the time-of-arrival of the shock at each station, the shock velocity may be calculated using the distance between adjacent stations (30.5 cm in the driven section, 61.0 cm in the expansion section) and the appropriate time interval. The shock velocity, along with knowledge of the gas composition, allows the post-shock properties to be calculated in each section. The post-shock conditions are calculated using FROSH, a frozen-chemistry, thermal-equilibrium shock code developed at Stanford. The calculated post-shock pressure typically agrees to within 3% of the measured wall pressure each section.

In order to more clearly define the test flow condition and test time, separate characterization tests employing a nonreactive test gas similar to the combustible mixture are conducted. For example, a characterization mixture of 5% CO₂ + 15% H₂ + 80% N₂ is substituted for a 6.7% H₂ + 13.3% O₂ + 80% N₂ reactive mixture, both having similar average molecular weights and producing similar shock speeds. The addition of CO₂ allows for IR-absorption measurements which show the arrival of test gas as the detector port (Fig. 3.4). The absorption signal can then be compared with the pressure history at that location in order to determine the helium flow time and test gas uniform flow time (test time) there. Characterization tests also employ an array of four pitot probes with embedded piezo-electric pressure transducers to measure the pitot pressure at the exit of the tube (Fig. 3.5). Although the gas static pressure and velocity are matched across the helium/test gas contact surface, the differences in gas composition and density mean that the pitot pressure changes quite dramatically across the surface. Therefore, the pitot pressure history provides time-of-arrival information for both the shock and test gas, and also a measure of the test time at the exit of the tube. The contact surface velocity may then be calculated based on the time interval between the arrival of the test gas at the IR port and the pitot probe. In our analysis, this value is assumed to be equivalent to the flow velocity immediately behind the contact surface. Note that this velocity constitutes an average value over the final 104 cm of the expansion section.

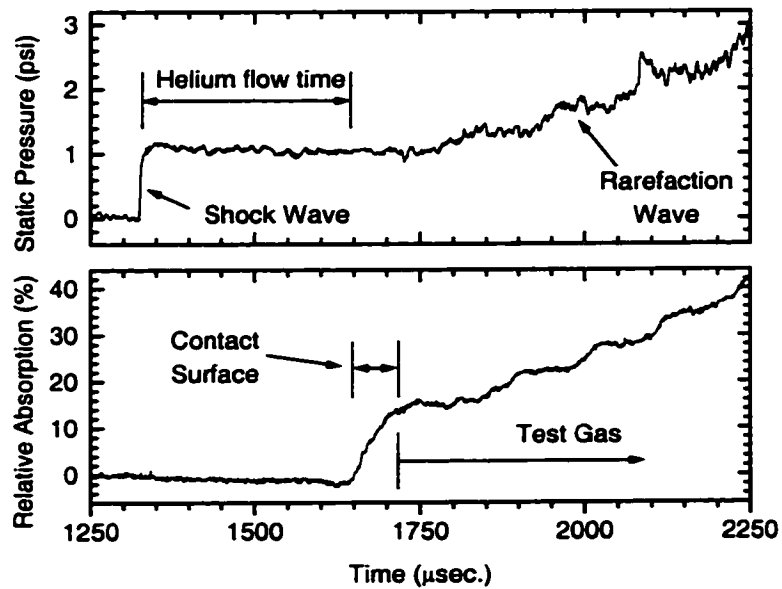


Figure 3.4: Example wall pressure and IR absorption records at $x = 102$ cm upstream from exit plane of the expansion tube. Test gas: 5% CO_2 + 95% N_2 . $P_{10} = 5.00$ mm Hg helium. $M_{\text{shock}} = 2.85$.

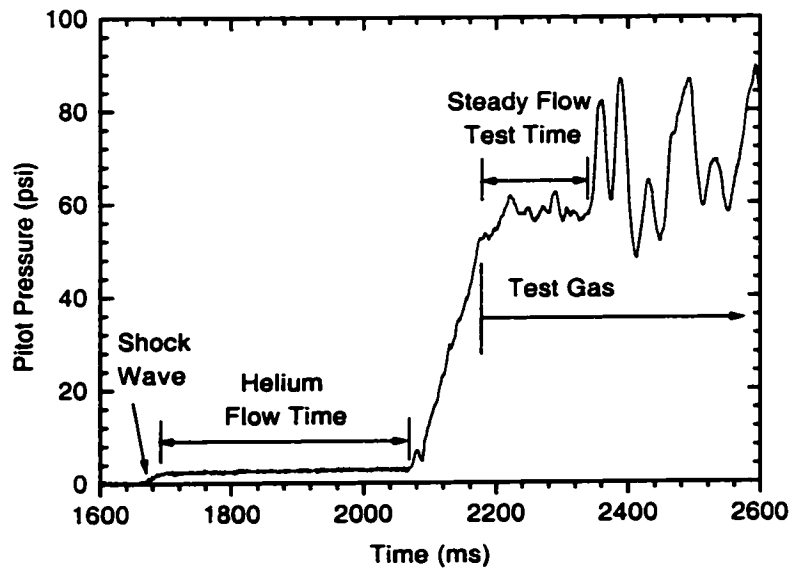


Figure 3.5: Example pitot pressure record from $x = 2$ cm downstream of the exit plane of the expansion tube. Test gas: 5% CO_2 + 95% N_2 . $P_{10} = 5.00$ mm Hg helium. $M_{\text{shock}} = 2.85$.

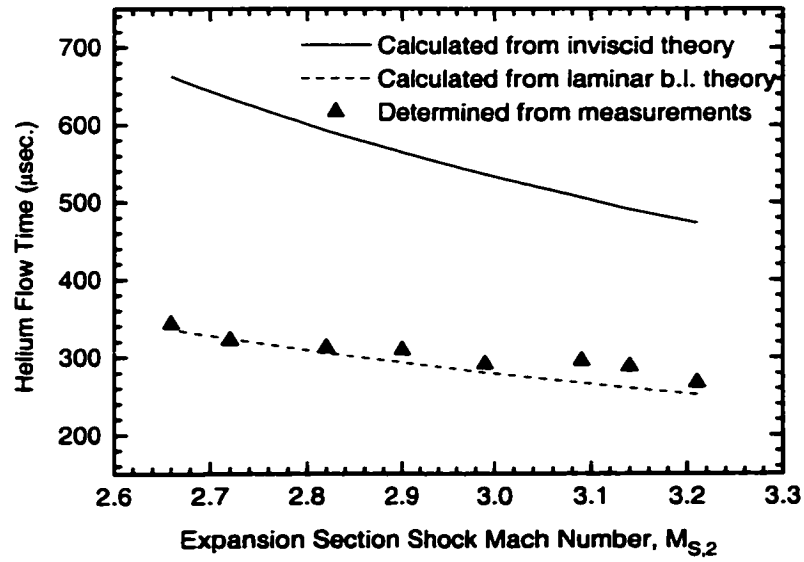
In addition to the test flow velocity and pressure, the temperature is required for accurate analysis of the experimental results. The test flow temperature and Mach number are obtained using an indirect calculation procedure. The test flow composition, pressure and velocity are fixed as input variables into FROSH. The input temperature is then varied until the calculated post-shock pressure, followed by an isentropic compression to stagnation, agrees well with the measured pitot pressure. The value of the test flow Mach number calculated in this fashion is typically within 3% of that predicted by assuming an isentropic expansion of the shocked test gas in the driven section to the final test flow pressure in the expansion section.

3.1.5 Observed Flow Nonidealities

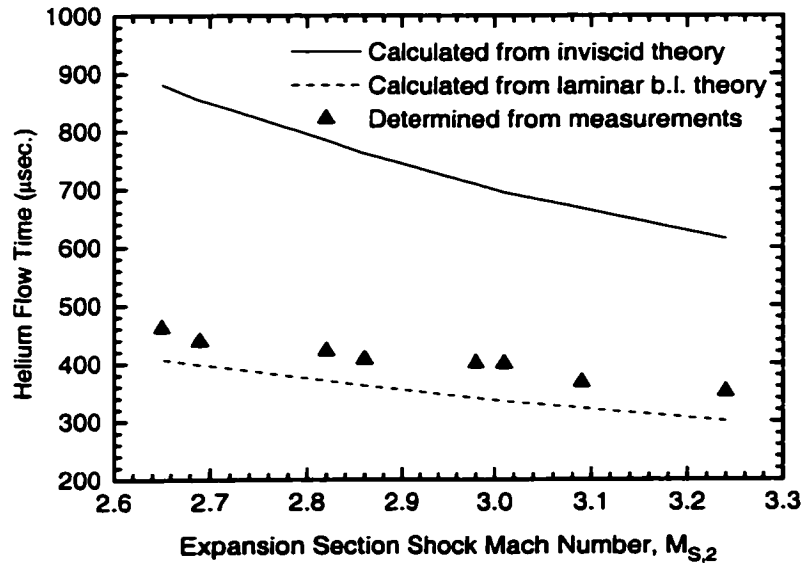
Experimental results from a series of facility characterization tests performed by Morris et al. (1995), shortly after the facility was fully operational, are reported here. In this series the driver and expansion section pressures are held constant, and the driven section pressure varied over a wide range in order to generate shocks of different strength in the acceleration gas. The helium flow time and test time are determined at two different locations, using the wall static pressure/IR absorption method at a station 102 cm from the downstream end of the expansion tube, and pitot pressure measurements 2 cm downstream from the end of the expansion tube.

The measured helium flow times are plotted against measured expansion section shock wave Mach number in Fig. 3.6. The helium flow time computed for an ideal, inviscid expansion tube, using the measured shock speeds in the calculation, is shown in Fig. 3.6 for comparison. The measured flow time is roughly half that predicted by theory, a result consistent with the boundary layer-related degradation typically experienced in shock tubes. There is good agreement between the data and a viscous prediction for the flow time using the laminar boundary layer methods of Mirels (1963, 1966). These results were obtained from a series of tests in which the expansion section fill pressure, P_{10} , was fixed at $P_{10} = 5$ mm Hg helium. A battery of tests run with $P_{10} = 10$ mm Hg helium yielded similar agreement. Estimates for the Reynolds number of the helium at the contact surface indicate that the boundary layer in that gas likely remains laminar throughout the experiment. This agreement suggests that, in the absence of definitive measurements, the laminar boundary layer correction to the theory can allow a good prediction for the time of arrival of the test gas at the tube exit to be made. Further confirmation of boundary layer effects comes from measurements by the pitot rake which indicate a core flow region ~ 4 cm in diameter.

The test gas flow time is measured from the end of the contact surface to the onset of pressure rise in the test gas history. In this series of characterization tests, typical test times range from 100–200 μ s. This range is consistent with the reacting flow experiments which constituted the focus of



(a)



(b)

Figure 3.6: Comparison of measured helium flow-time data with viscid and inviscid predictions using measured expansion section shock speed. (a) Wall static pressure/IR absorption method at $x = 102$ cm upstream from exit plane of the expansion tube. (b) Pitot pressure method at $x = 2$ cm downstream of the exit plane of the expansion tube. Laminar boundary layer assumed for viscous correction. Test gas: 5% CO_2 + 95% N_2 . $P_{10} = 5.00$ mm Hg helium.

M_{S1}	c_2 (m/s)	c_3 (m/s)	c_2/c_3	Observed Oscillations
4.79	738	562	1.31	None
4.21	689	609	1.13	None
4.05	657	640	1.03	10 kHz, 18 kHz
3.69	619	678	0.913	10 kHz, 16 kHz
3.44	591	706	0.837	10 kHz, 24 kHz

Table 3.1: Spectral analysis of oscillation phenomena on pitot pressure records. M_{S1} is the measured shock Mach number through the test gas in the driven section. c_2 is the post-shock test gas sound speed. c_3 is the sound speed of the expanded driver gas adjacent to the contact surface. Test gas: 5% CO_2 + 95% N_2

this work.

Note the presence of relatively small oscillations in the wall static pressure history and IR absorption traces of the test gas, and significantly larger oscillations in the pitot measurements. A complete analysis of the pressure oscillation phenomena is beyond the scope of this work. However, the oscillations appear similar to those observed and modeled in work by Paull and Stalker (1999). In brief, those authors modeled the oscillations as lateral waves generated at the primary diaphragm station. These waves can be transmitted into the test gas and focused in the expansion wave, thereby disrupting the integrity of the uniform test time. Paull and Stalker also demonstrated that these waves could be dissipated at the driver/test gas contact surface if the sound speed of the test gas is sufficiently higher than that of the expanded driver gas. A spectral analysis of our center-line pitot pressure records is in good agreement with their work (Tbl. 3.1). The strong 10 kHz wave observed in the data agrees well with the 12 kHz 1st-order lateral wave frequency predicted by their methods for typical conditions in these experiments.

3.2 Optical Diagnostics

This section reviews the optical diagnostic set-up for PLIF and schlieren imaging in the facility. A brief review of the basis of PLIF is provided first, as a background to the specific description of the optical set-up which follows.

3.2.1 Description of PLIF Imaging

The basis of PLIF as applied here is linear laser excitation of tracer molecules, followed by broadband collection of the fluorescence from the radiative decay of these excited molecules. In the

present study on reactive flows, PLIF imaging relied on OH, a naturally occurring combustion radical, as the fluorescent tracer. For each experiment, the CCD array accumulated a fluorescence signal given by Hanson et al. (1990):

$$S_f = \eta V_c n_{\text{OH}} f_{J''} B E g \phi \quad (3.1)$$

where η represents the overall efficiency of the optical setup in converting photons from fluorescence into photoelectrons incident on the detector, V_c is the collection volume, n_o is the number density of the absorbing species OH, $f_{J''}$ is the Boltzmann fraction of the tracer species molecules that are in the absorbing state, B is the Einstein coefficient for stimulated absorption, E is the laser energy fluence (energy per unit area), and g is the spectral convolution of the laser spectral distribution and the absorption transition. The fluorescence yield ϕ , defined as $A/(A + Q)$, where A is the Einstein coefficient for spontaneous emission from the populated upper states and Q is the rate of electronic quenching to the lower state, represents the fraction of the molecules pumped to the upper state that decay radiatively.

At the combustion pressures obtained in this work, $Q \gg A$, which simplifies the fluorescence yield to $\phi \simeq A/Q$. Q can be represented by the expression $Q = n_{\text{tot}} \sigma \langle v \rangle$, where n_{tot} is the total number density of the mixture, σ is the mixture-averaged quenching cross-section, and $\langle v \rangle$ is the mean molecular speed. Typically, the mixture-averaged quenching cross-section is the most difficult term to quantify. If we assume that σ is constant, then Q is simply proportional to $n_{\text{tot}} T^{1/2}$. Thus, the fluorescence signal can be simplified as:

$$S_f \sim \chi_{\text{OH}} [f_{J''}/T^{1/2}] \quad (3.2)$$

where χ_{OH} is the OH mole fraction. For the absorption transition considered here — the $Q_1(7)$ transition of the $A^2\Sigma^+ \leftarrow X^2\Pi(1, 0)$ band of OH, located at 283.31 nm — the bracketed term in (3.2) plays a relatively minor role in interpreting the signal in the regions observed to contain OH. It is important to point out that, due to the strong collisional cross-section of H_2O (see, for example, the calculations of Paul (1994)), the assumption of constant cross section is at best only approximate in the portions of the flowfield undergoing substantial energy release and water production. As the OH measurements in this work are primarily used for mapping the location of the reaction front, it is thought that this effect does not significantly impact the conclusions.

3.2.2 Description of Imaging Set-up

The laser sheet for OH PLIF imaging is formed from the frequency-doubled output of a Lumonics HD-500 dye laser pumped by a Lumonics YM-1200 pulsed Nd:YAG laser. Rhodamine 590 dye is used for OH PLIF transitions near 283 nm, with pulse energies of approximately 6 mJ. The sheet is

roughly 0.5 mm thick \times 3 cm wide at the viewing section. A dichroic mirror, mounted at 45° with respect to the observation windows, serves to reflect $> 99\%$ of the collected OH fluorescence into the optics of a 578×384 Princeton Instruments (PI) intensified CCD camera. UG11 and WG305 Schott glass filters are placed in front of the camera's $f/4.5$, 105 mm UV objective lens in order to block elastically scattered laser light while still passing the majority of the OH fluorescence. A 100 ns camera intensifier gatewidth was employed to capture all of the fluorescence signal (15 - 20 ns), while minimizing the interference from natural emissions in the flowfield.

The schlieren system was set up in a standard Z-arrangement. Illumination is provided by a Strobotac 1539 Stroboslave Xenon flashlamp light source (3-4 μ sec duration). Two $f/8$, 31.8 cm (dia.) concave mirrors are positioned to collimate the light through the test section, and then refocus it onto a knife-edge (razor blade). The test object is imaged with an $f/6$, 80 mm lens onto a 576×384 PI ICCD camera. The same dichroic mirror used to divert the OH PLIF fluorescence also passes the visible light used in the schlieren system. The camera gatewidth is set to 100 ns.

The PLIF and schlieren systems are controlled by electronics triggered from the pressure transducer located 40.6 cm from the exit of the tube (approximately 870 μ s before the onset of the steady flow test time). The PLIF laser and schlieren flashlamp are synchronized to fire near the end of the $\sim 150 \mu$ s test time. The PLIF camera system is triggered by an output signal synchronized to the Q-switch on the PLIF laser system; the schlieren camera acquires its image $\sim 2 \mu$ s later.

Chapter 4

Study of Oblique Detonation Waves in Wedge Flows

4.1 Numerical Study of Oblique Detonation Waves

As was described in Chapter two, the shock polar diagram allows for several flow scenarios as the wedge turning angle is varied. Three possible regimes are depicted schematically as cases (a), (b), and (c) below the example shock polar diagram in Fig. 4.1. To summarize briefly, shock polar theory predicts that a steady, straight oblique detonation wave may be stabilized on a wedge only in case (b) ($\theta_{C-J} < \theta < \theta_{det,eq}$). Wedge turning angles greater than the detachment point on the equilibrium polar ($\theta_{det,eq} < \theta < \theta_{det,fr}$) will lead to an initially straight frozen oblique shock wave, which transitions to a locally detached detonation wave. There is a question as to whether the detached detonation can remain steady and stabilized on the wedge. Additionally, Rankine-Hugoniot and shock polar theory do not allow for steady, equilibrium shock solutions at a wave angle below the C-J point on the polar diagram. This leads to a question regarding the nature of exothermic flows when the wedge turning angle is reduced below the C-J point ($0 < \theta < \theta_{C-J}$). In this section, we will study the formation of detonation waves in each of these scenarios using numerical simulations.

4.1.1 Oblique Detonation Wave Formation when $\theta_{C-J} < \theta < \theta_{det,eq}$

As may be seen from the polar diagram, when $\theta_{C-J} < \theta < \theta_{det,eq}$, both inert (frozen chemistry) shocks and detonation waves (equilibrium chemistry) have valid solutions in this regime. In Chapter two, we pointed out some of the effects that finite-rate chemistry has on an actual wedge-induced oblique detonation flowfield. To summarize, in nearly any physical case, an inert oblique shock (at

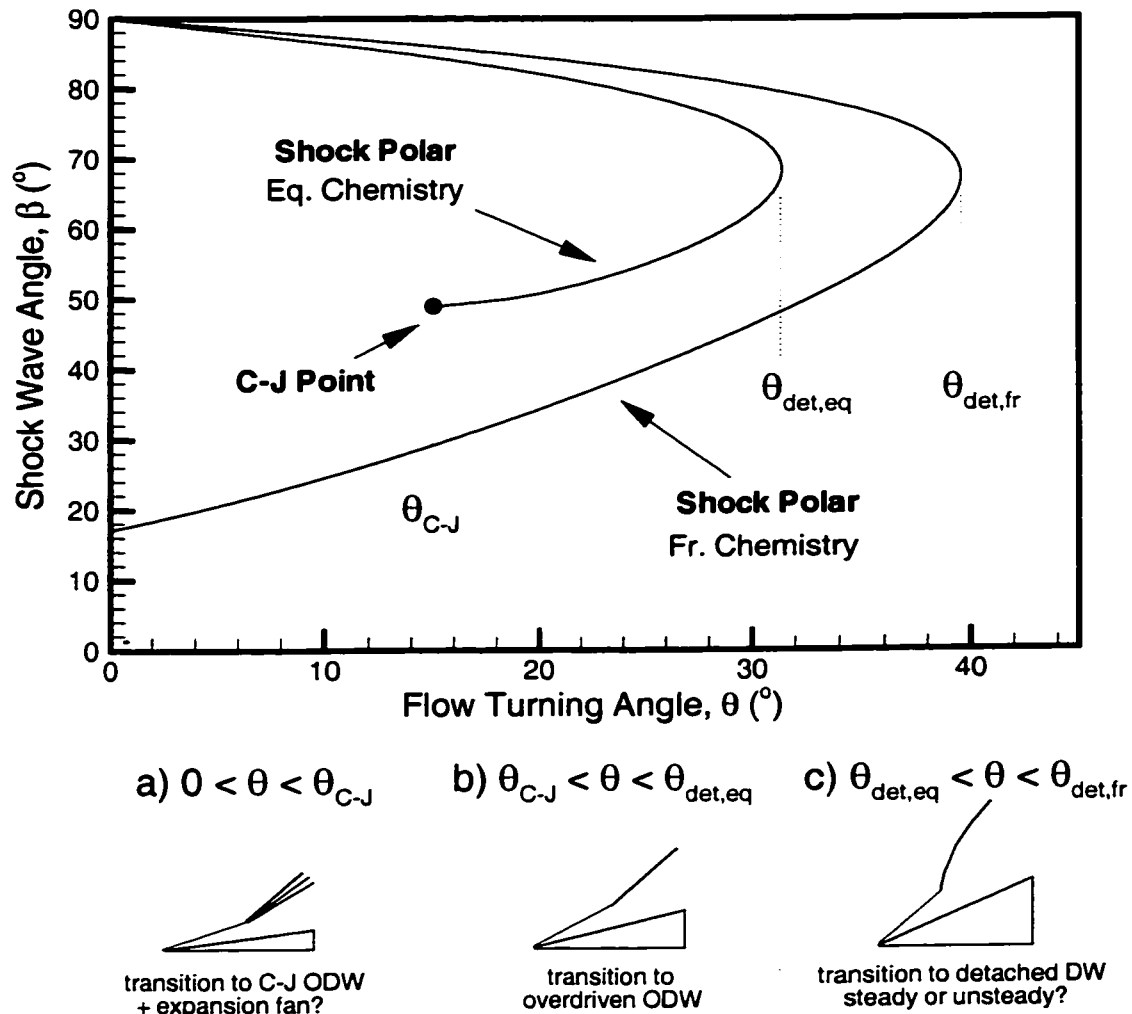


Figure 4.1: Example shock polar diagram showing solutions for a frozen shock, and for a shock with instantaneous equilibrium chemistry. Gas Mixture: H_2 -air ($2H_2 + O_2 + 3.76N_2$). $T_1 = 1000$ K, $P_1 = 1.0$ atm, $V_1 = 2500$ m/s.

an angle β_{fr} given by the frozen polar curve) will form attached to the wedge tip. If the temperature behind the oblique shock is sufficiently high, at some point downstream a reaction front can be initiated along the wedge surface. This reaction front can then merge with the shock and form a stabilized oblique detonation wave. The detonation will also eventually converge to a steady angle, β_{eq} , given by the equilibrium polar curve. The preliminary calculations shown in Chapter two showed that the relative length of the ignition and equilibration zones, compared to the physical dimensions of the wedge body, were critical in determining both whether a reaction front is initiated

on the wedge surface, and how rapidly the shock transitions to a stabilized oblique detonation wave. Here, we will explore the transition from the decoupled oblique shock and reaction front to a fully coupled oblique detonation wave in greater detail.

We present here results from a series of simulations spanning a range of wedge turning angles and freestream pressures. The pressure was varied as a way of changing the relative rate of energy release in the flowfield, while leaving the total energy release approximately constant. As was shown in Chapter two, the final equilibrium composition does depend on the mixture pressure. However, as our main interest here is studying the transition to oblique detonation, this factor only slightly modifies the final detonation wave angle, and does not significantly impact our interpretation of the results. Varying the wedge angle allows us to determine the impact of this variable on the transition, particularly as the angle approaches the detachment limit on the equilibrium curve.

These simulations were run using the same freestream temperature, velocity and gas mixture used in Chapter two. In each case the grid size was 260×200 cells, with the length of the horizontal domain scaled to be approximately five times the theoretical ignition length behind the initial oblique shock. This theoretical ignition length was calculated using CHEMKIN with the post-shock temperature, pressure and velocity computed using the NASA Lewis CET-89 code. Scaling the domain size in this way allows us to focus on the transition from oblique shock-induced combustion to an oblique detonation wave. In effect, this fixes $L_{\text{ign}} \simeq 0.2 \times L_{\text{flow}}$. A series of 16 test cases was studied, formed from a range of five freestream pressures (0.05, 0.1, 0.2, 0.5, and 1.0 atm) and four wedge angles (25° , 30° , 35° , and 40°). Additionally, in order to determine the effect of grid resolution on the results, extra simulations were run at both higher- and lower-resolution for those conditions selected as representative examples. The higher-resolution tests examined the same total domain size using a grid size of 390×300 , where Δx and Δy were $2/3$ of their original values. The 390×300 grid was found to be the maximum practical grid which could be run at double-precision on the machine used in this study. Similarly, the lower-resolution tests examined the same domain on a resolution of 130×100 , with Δx and Δy twice their original values.

Considering the question of how an oblique shock transitions to an oblique detonation, we would intuitively expect the issue to depend primarily on both the initial distance between shock and the reaction front, and the rate at which energy release takes place after ignition. Therefore, as a means of classifying these results, we introduce a normalized reaction parameter comparing the ratio of characteristic equilibration and ignition timescales. The ignition time, along with the angle between the shock and surface, governs the initial distance between the shock and the reaction front. The definition of ignition time adopted here is the point at which the change in temperature has reached 1% of the total temperature change from the initial to final states. That is

$$\tau_{\text{ign}} = \tau_{\Delta T=1\% \Delta T_{\text{tot}}} \quad (4.1)$$

A characteristic equilibration timescale, here defined from the 1% ignition point to the point at which the change in temperature has reached 50% of the total change, is a representative value for the rate at which energy is initially released along the surface.

$$\tau_{\text{equil}} = \tau_{\Delta T=50\% \Delta T_{\text{tot}}} - \tau_{\Delta T=1\% \Delta T_{\text{tot}}} \quad (4.2)$$

Thus, the normalized reaction parameter is simply

$$NRP = \frac{\tau_{\text{equil}}}{\tau_{\text{ign}}} \quad (4.3)$$

For our analysis here, we make use of a predicted normalized reaction parameter based on constant density ignition and combustion (modeled by CHEMKIN-II) of the gas mixture behind the initial oblique shock wave. The post-shock conditions are calculated using the NASA Lewis CET-89 code. Treating the combustion process along the wedge surface as a constant density flow is an approximation, but is done with the view of developing a simple method for predicting the nature of the transition to oblique detonation.

We first present here three example cases from the test matrix. These three cases are chosen to demonstrate relevant features of the flowfield as the normalized reaction parameter is varied. Following the examples, the full results from the test matrix are tabulated. The first test case given is stoichiometric H_2 -air flow over a $\theta = 40^\circ$ wedge. Freestream conditions are $T_1 = 280 \text{ K}$, $P_1 = 0.1 \text{ atm}$, $M_1 = 8$. Grid spacing was $\Delta x = 0.02 \text{ mm}$, $\Delta y = 0.01 \text{ mm}$. Temperature and OH mole fraction contour plots and a corresponding plot of shock wave angle for the converged CFD solution are shown in Fig. 4.2. Note that the reaction front in this case gradually converges toward the oblique shock across the flowfield. However, even at the rightmost edge of the domain, there remains a significant gap between the shock and the reaction front. The shock wave angle also increases relatively slowly across the flowfield, and does not achieve the equilibrium oblique detonation wave angle within the domain. The predicted τ_{ign} and τ_{equil} for this case are $0.45 \mu\text{s}$ and $1.35 \mu\text{s}$ respectively, corresponding to a predicted normalized reaction parameter of $NRP = 3.0$. At least for this particular condition, the relatively large equilibration time in comparison to the ignition time results in a relatively slow transition to oblique detonation.

Intuitively, it appears from the OH mole fraction plot that the reduction in induction length behind the oblique shock is coupled to the increase in shock wave angle. A comparison of local shock wave angle with the ignition length behind the shock, as a function Y-coordinate, is shown

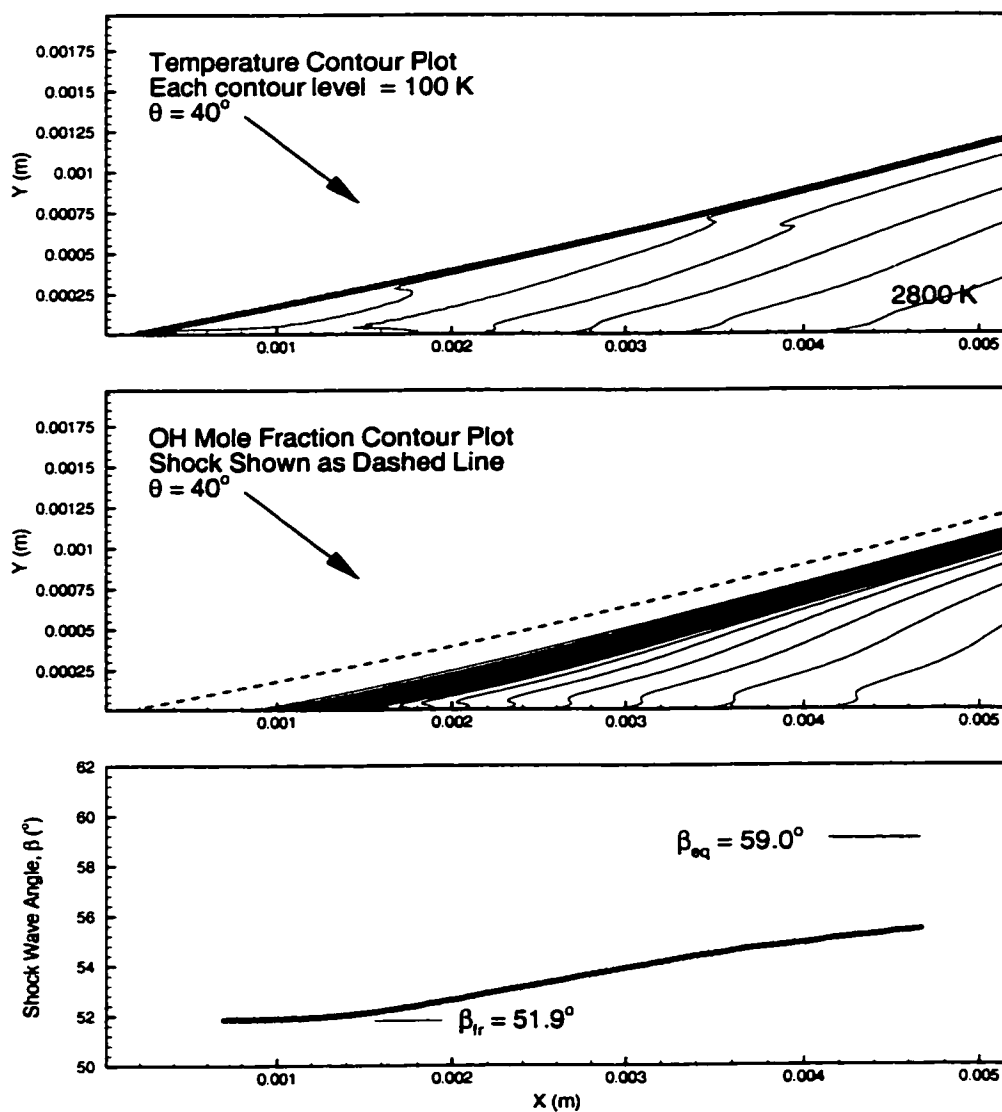


Figure 4.2: Converged CFD simulation of stoichiometric H_2 -air ($2\text{H}_2 + \text{O}_2 + 3.76\text{N}_2$) flow over a $\theta = 40^\circ$ wedge. $T_1 = 280\text{ K}$, $P_1 = 0.1\text{ atm}$, $M_1 = 8$. $\Delta x = 0.02\text{ mm}$, $\Delta y = 0.01\text{ mm}$. Upper panel: temperature contour plot. Middle Panel: OH mole fraction contour plot. Lower panel: corresponding plot of shock wave angle as a function of grid x-coordinate.

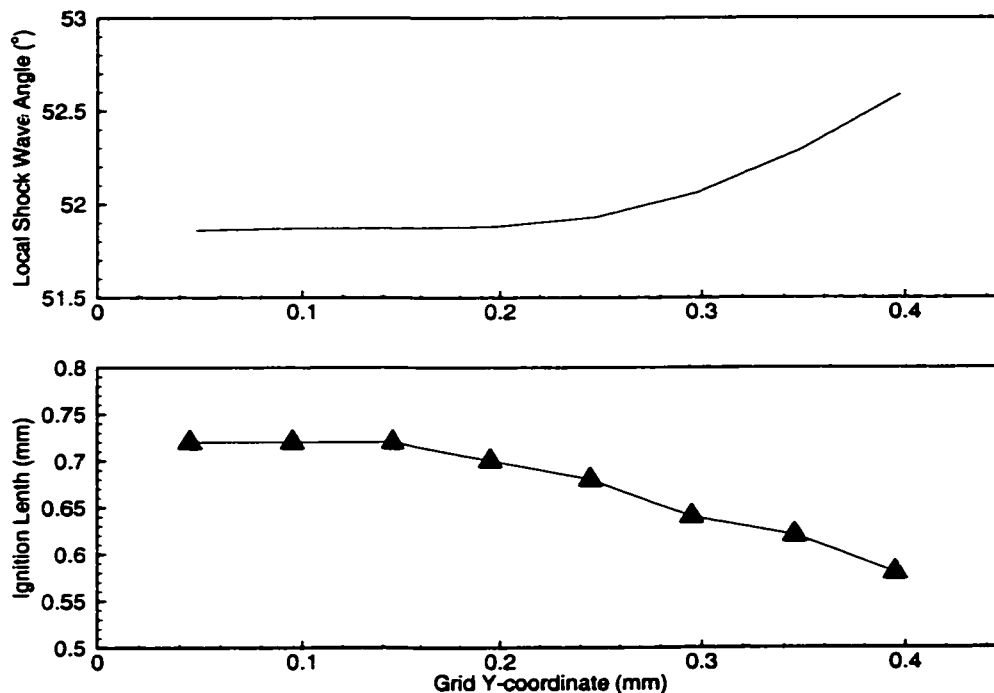


Figure 4.3: Plots comparing the local shock wave angle (upper panel) to the ignition length behind the shock (lower panel), as a function of grid Y-coordinate. The CFD calculation is based on the same test conditions as Fig. 4.2 (stoichiometric H_2 -air flow over a $\theta = 40^\circ$ wedge, $T_1 = 280$ K, $P_1 = 0.1$ atm, $M_1 = 8$).

in Fig. 4.3. The length was measured from the onset of the shock to the point where $\chi_{OH} = 0.001$. Comparison of these two curves confirms that the reduction in ignition length behind the shock indeed corresponds to the increase in shock wave angle. As the ignition length is naturally expected to decrease with increasing shock angle, it is logical to conclude that shock steepening is a significant factor in accelerating the reaction front toward the shock.

The effects of grid resolution on this test case are shown in Fig. 4.4. The baseline resolution (that used in Fig. 4.2) is shown in the middle subfigure of each panel of the figure. Lower- and higher-resolution results are shown in the top and bottom subfigures of each panel, respectively. In order to view potential differences with greater clarity, two different subdomains are shown. The left-hand panel shows the induction zone region along the wedge surface. The low- and high-temperature boundaries of the oblique shock are shown by dashed lines. The increased thickness of the oblique shock is quite evident in the lower-resolution results. All three resolutions depict a clearly-resolved induction zone between the shock and reaction front, though the induction length is slightly smaller in the lower-resolution grid. The right-hand panel depicts the induction zone region

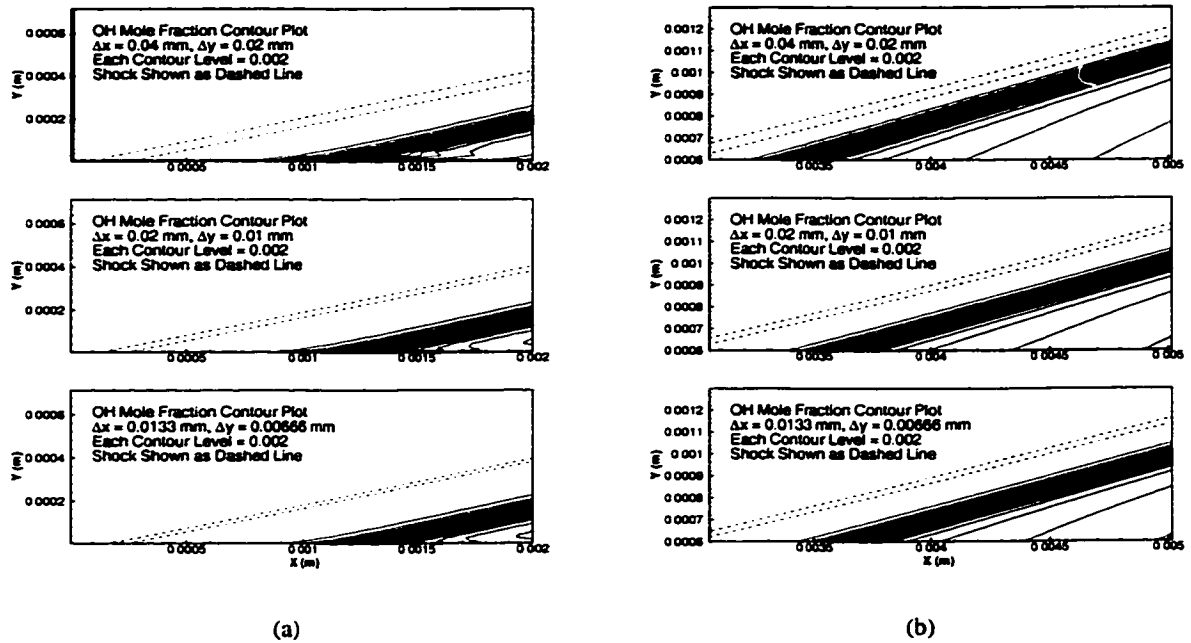


Figure 4.4: Examination of two different subdomains of the flowfield at different grid resolutions: (a) the induction zone along the wedge surface, (b) the induction zone near the right boundary of the domain. Contours of OH mole fraction are shown, with the low- and high-temperature boundaries of the oblique shock shown via dashed lines. The CFD calculations are for the same test conditions as Fig. 4.2 (stoichiometric H_2 -air flow over a $\theta = 40^\circ$ wedge, $T_1 = 280$ K, $P_1 = 0.1$ atm, $M_1 = 8$)

near the right boundary of the original domain. There is again little difference between the baseline and higher-resolution results here. However, the lower-resolution results show the reaction zone drawing significantly closer to the oblique shock than in the other two resolutions. This appears to result from the inability of the coarser grid to resolve the energy release as accurately as the baseline and higher-resolution grids. Thus, shock-steepening, and the consequent acceleration of the reaction front toward the shock, proceed more rapidly. In general, however, all three resolutions show the same physical feature of slow transition to oblique detonation.

The second test case we discuss is of stoichiometric H_2 -air flow over a $\theta = 35^\circ$ wedge. Freestream conditions are $T_1 = 280$ K, $P_1 = 0.2$ atm, $M_1 = 8$. Grid spacing was $\Delta x = 0.028$ mm, $\Delta y = 0.014$ mm. Temperature and OH mole fraction contour plots, and a corresponding plot of shock wave angle for the converged CFD solution are shown in Fig. 4.5. The oblique shock in this case smoothly transitions from the frozen shock angle to the equilibrium oblique detonation wave angle within the domain. The length of the transition region is roughly $2.6L_{ign}$. It is evident from the figure that, as in the previous case, the increase in shock wave angle throughout the

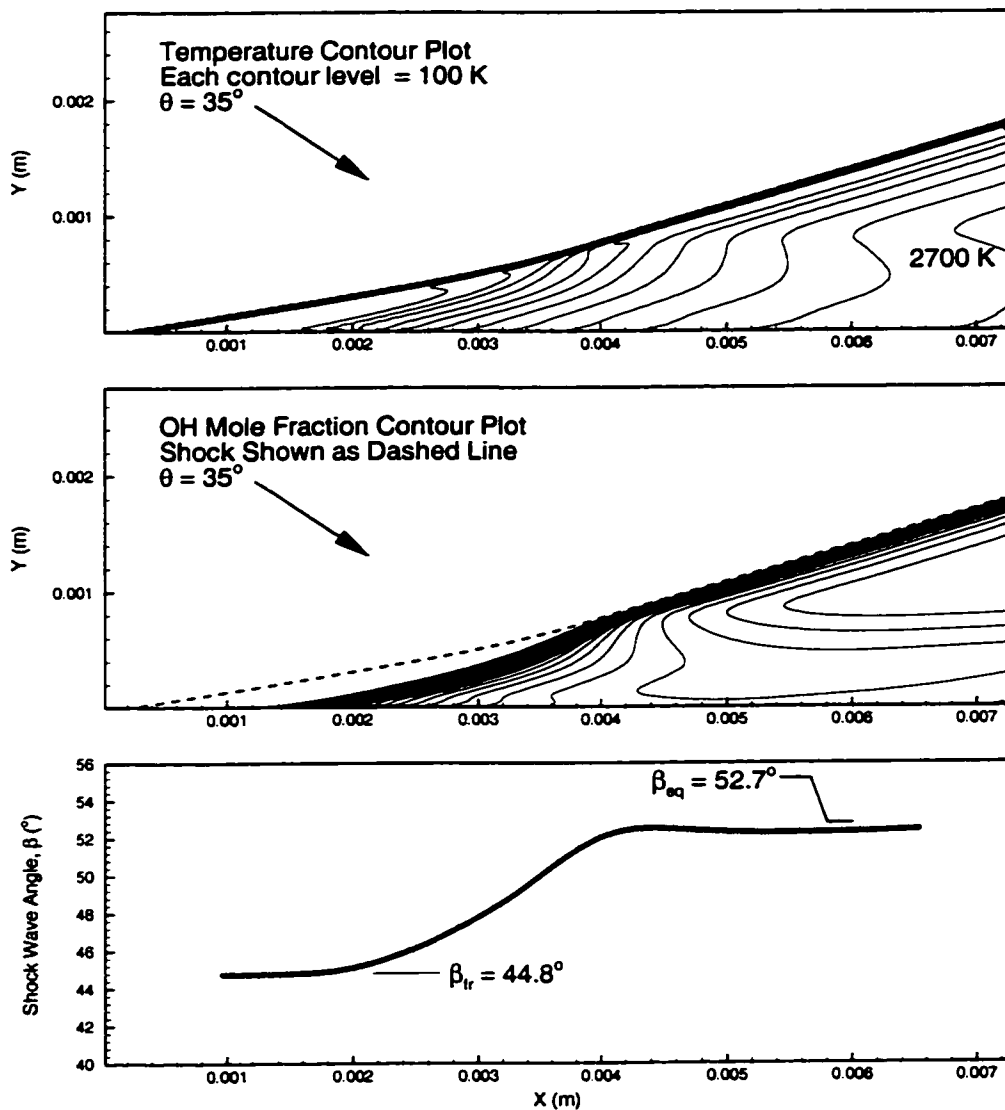


Figure 4.5: Converged CFD simulation of stoichiometric H_2 -air ($2\text{H}_2 + \text{O}_2 + 3.76\text{N}_2$) flow over a $\theta = 35^\circ$ wedge. $T_1 = 280\text{ K}$, $P_1 = 0.2\text{ atm}$, $M_1 = 8$. $\Delta x = 0.028\text{ mm}$, $\Delta y = 0.014\text{ mm}$. Upper panel: temperature contour plot. Middle Panel: OH mole fraction contour plot. Lower panel: corresponding plot of shock wave angle as a function of grid x-coordinate.

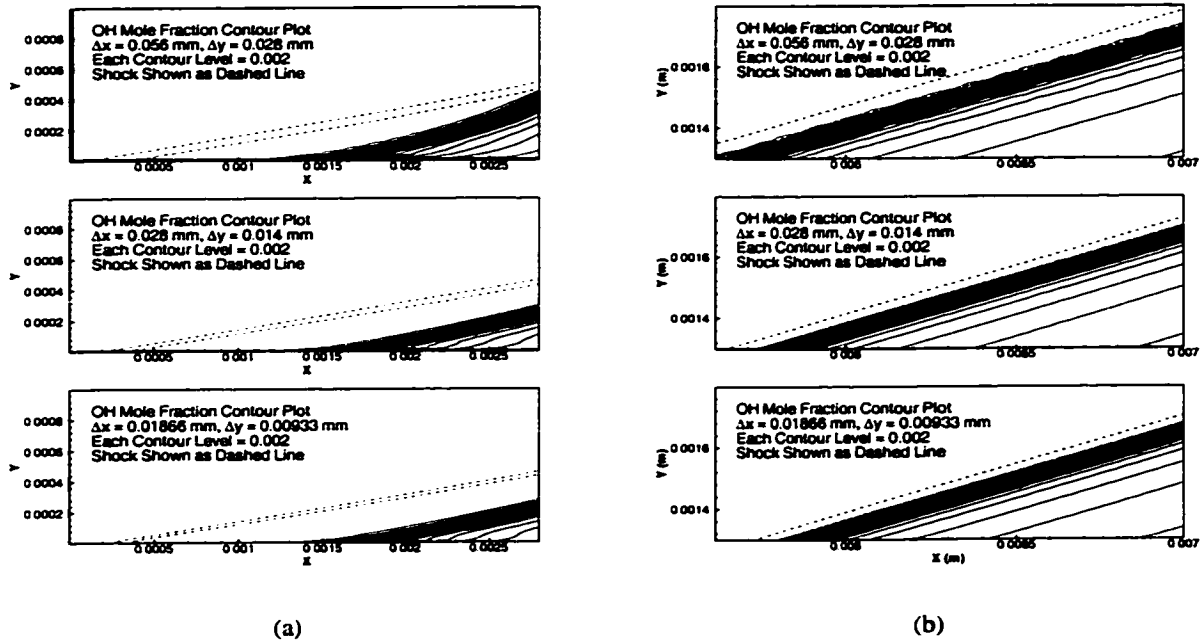


Figure 4.6: Examination of two different subdomains of the flowfield at different grid resolutions: (a) the induction zone along the wedge surface, (b) the induction zone near the right boundary of the domain. Contours of OH mole fraction are shown, with the low- and high-temperature boundaries of the oblique shock shown via dashed lines. The CFD calculations are based on the same test conditions as Fig. 4.5 (stoichiometric H_2 -air flow over a $\theta = 35^\circ$ wedge, $T_1 = 280$ K, $P_1 = 0.2$ atm, $M_1 = 8$)

transition region (a process itself driven by the energy release) has a significant impact in “pulling” the reaction front toward the shock wave. However, close inspection also reveals that the reaction front begins to close toward the shock before shock steepening can significantly affect the ignition length. Therefore, the compression waves generated by the energy release along the wedge surface also appear to play a role in reducing the ignition delay behind the shock. Note that, once the shock transitions to an oblique detonation wave, the temperature and OH contours behind the shock also draw parallel to the detonation front. This is consistent with the steady, straight oblique detonation wave model presented in Chapter two. The predicted τ_{ign} and τ_{equil} for this case are $0.54 \mu s$ and $0.53 \mu s$ respectively, corresponding to a predicted normalized reaction parameter of $NRP = 0.98$. Note that while the predicted ignition time here is little larger than that of the previous test case, the predicted equilibration time is significantly reduced. This reduction in characteristic equilibration time results in the smooth but complete transition to oblique detonation within the domain.

The impact of grid resolution on this test case is shown in Fig. 4.6. As in the previous case, the

baseline resolution used in Fig. 4.5 is shown in the middle subfigure of each panel, while lower- and higher-resolution results are shown in the top and bottom subfigures, respectively. Two subdomains of the full flowfield are shown in order to distinguish differences more clearly. The low- and high-temperature boundaries of the oblique shock are shown by dashed lines. The effect of grid resolution is more pronounced in this test case. The left-hand panel shows the induction zone along the wedge surface. Note that the coarser resolution exhibits a shorter induction zone than the baseline and higher-resolutions. Additionally, the reaction front accelerates toward the oblique shock more rapidly in the lower-resolution test. The inability of the coarser grid to resolve the energy release is consistent with the results in the previous test case (Fig. 4.4). There is significantly less difference between the baseline and higher-resolution tests in this subdomain, though the higher-resolution case does exhibit a slightly larger induction zone. Despite these differences in detail, all three resolutions show the same physical feature of smooth transition to oblique detonation within the full domain studied.

The right-hand panel of Fig. 4.6 examines the fully-formed oblique detonation structure near the right edge of the flowfield. Due to the relatively faster transition to oblique detonation in the lower-resolution grid, the position of the oblique detonation is offset to the left in those results compared to the baseline resolution. Similarly, due to a slightly slower transition at higher-resolution, the position of the detonation is offset to the right. It is noteworthy that none of the resolutions fully capture the induction zone behind the oblique shock. Rather, there is overlap between the highest-temperature oblique shock contour and the onset of energy release. Undoubtedly, this is at least partially caused by the finite thickness of the oblique shock on these grids which allows some chemistry to occur within the shock structure. The question of the minimum grid resolution needed to fully resolve the induction zone within an oblique detonation in this regime remains open.

The third test case we discuss is of stoichiometric H_2 -air flow over a $\theta = 30^\circ$ wedge. Freestream conditions are $T_1 = 280 \text{ K}$, $P_1 = 0.5 \text{ atm}$, $M_1 = 8$. Grid spacing was $\Delta x = 0.046 \text{ mm}$, $\Delta y = 0.023 \text{ mm}$. Temperature and OH mole fraction contour plots, and a corresponding plot of shock wave angle for the converged CFD solution are shown in Fig. 4.7. Predicted characteristic times are $\tau_{\text{ign}} = 0.79 \mu\text{s}$ and $\tau_{\text{equil}} = 0.27 \mu\text{s}$, resulting in a predicted $NRP = 0.35$. Thus, while the ignition time is roughly $1.5\times$ that of the previous example case, the characteristic equilibration time is $0.5\times$ of the previous value. It is immediately obvious from the figure that the relatively short equilibration time leads to a very rapid transition to oblique detonation. In this case, the reaction front converges toward the oblique precursor shock very quickly. This leads to a small increase in the angle of the precursor shock. However, when the reaction front intersects the shock, an oblique detonation wave is formed at an angle greater than the equilibrium value. The detonation eventually decays to the

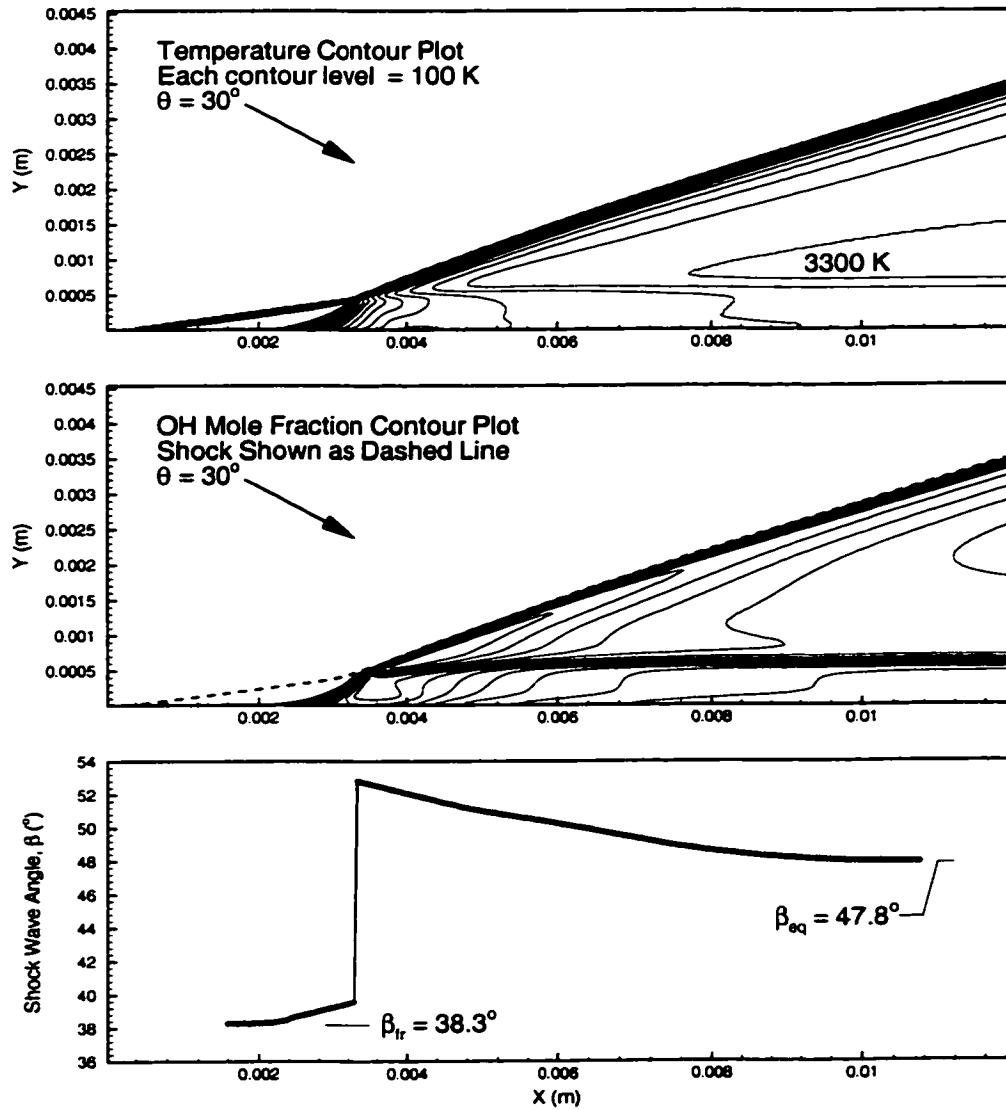


Figure 4.7: Converged CFD simulation of stoichiometric H_2 -air ($2\text{H}_2 + \text{O}_2 + 3.76\text{N}_2$) flow over a $\theta = 30^\circ$ wedge. $T_1 = 280\text{ K}$, $P_1 = 0.5\text{ atm}$, $M_1 = 8$. $\Delta x = 0.046\text{ mm}$, $\Delta y = 0.023\text{ mm}$. Upper panel: temperature contour plot. Middle Panel: OH mole fraction contour plot. Lower panel: corresponding plot of shock wave angle as a function of grid x-coordinate.

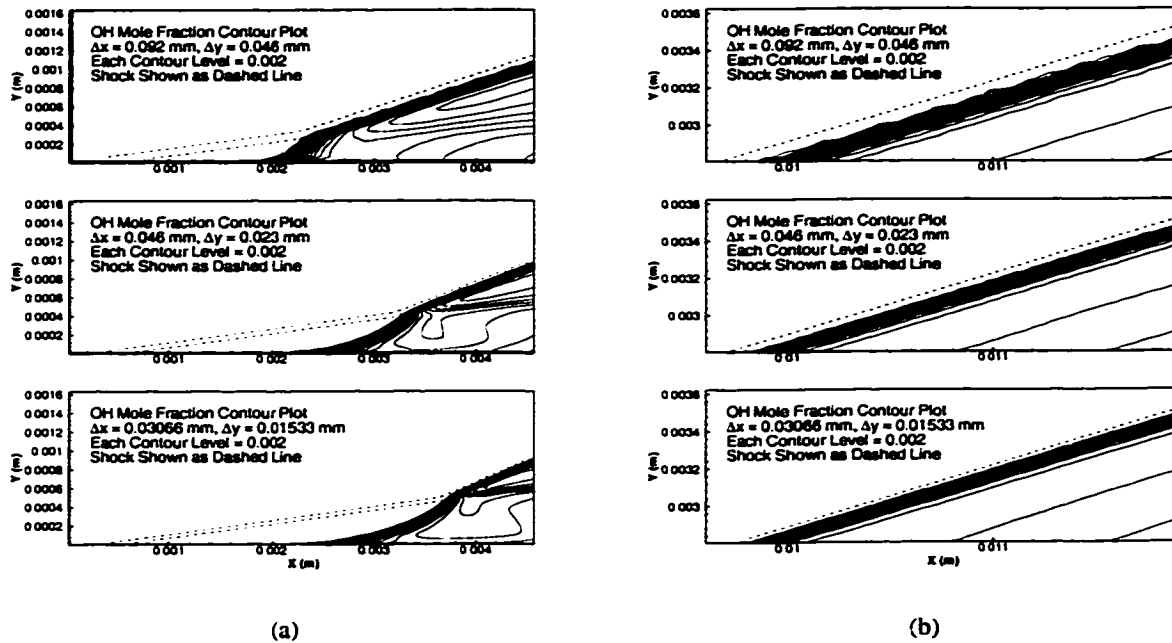


Figure 4.8: Examination of two different subdomains of the flowfield at different grid resolutions: (a) the induction zone along the wedge surface, (b) the induction zone near the right boundary of the domain. Contours of OH mole fraction are shown, with the low- and high-temperature boundaries of the oblique shock shown via dashed lines. The CFD calculations are based on the same test conditions as Fig. 4.7 (stoichiometric H_2 -air flow over a $\theta = 30^\circ$ wedge, $T_1 = 280$ K, $P_1 = 0.5$ atm, $M_1 = 8$)

equilibrium value in the far field. The discontinuous jump in shock angle leads to the formation of a contact surface separating the flow above and below the transition point.

The effect of grid resolution is pronounced in this test case, although all three resolutions show the same qualitative physical features of sudden transition to oblique detonation. As before, the baseline resolution used in Fig. 4.7 is shown in the middle subfigure of each panel, while lower- and higher-resolution results are shown in the top and bottom subfigures, respectively. Differences are particularly visible in the vicinity of the induction zone along the wedge surface (left-hand panel of Fig. 4.8). Similar to our observations in the previous test case, the lower-resolution grid exhibits a shorter induction zone and a significantly faster acceleration toward the oblique shock than the baseline and higher-resolution grids. This comparison is also true between the baseline and higher-resolution grids, although the difference is not as substantial. The right-hand panel in the figure examines the fully-formed oblique detonation wave structure near the right-edge of the domain. The oblique detonation waves are slightly offset from each other in the three resolutions

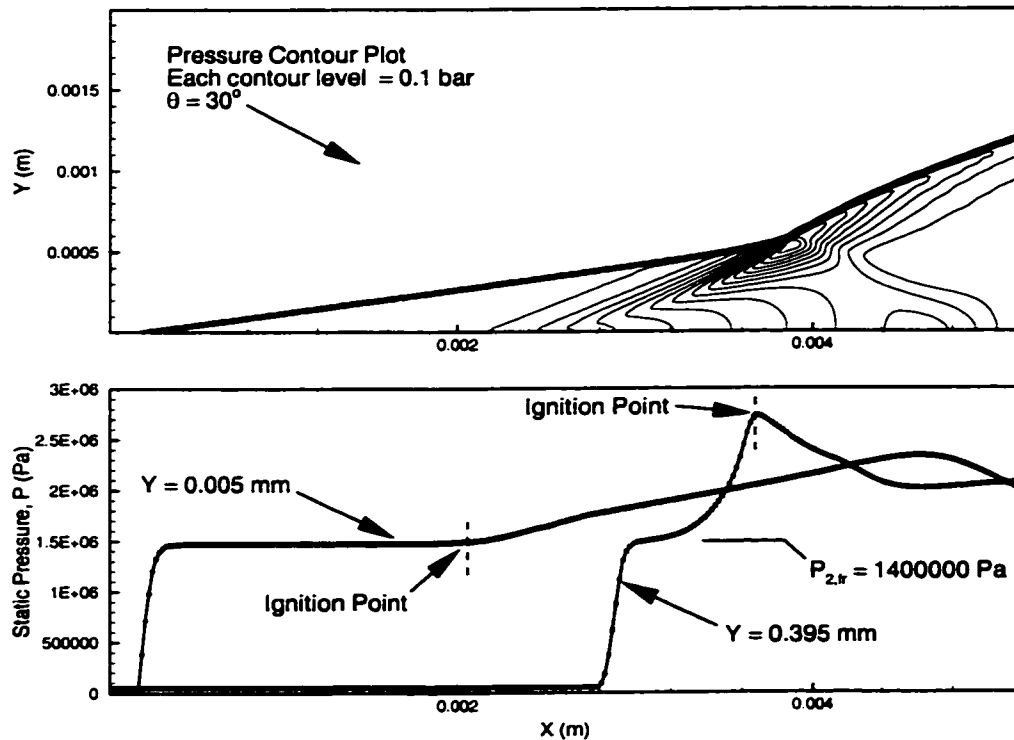


Figure 4.9: Pressure characteristics of third example case. Upper panel: pressure contour plot. Lower panel: Static pressure distribution as a function of grid x-coordinate at fixed $Y = 0.005$ mm (wedge surface) and $Y = 0.395$ mm. The CFD calculation is based on the same test conditions as Fig. 4.7 (stoichiometric H_2 -air flow over a $\theta = 30^\circ$ wedge, $T_1 = 280$ K, $P_1 = 0.5$ atm, $M_1 = 8$), though the grid resolution is greater: $\Delta x = 0.02$ mm, $\Delta y = 0.01$ mm.

due to differences in the transition point. As was true in the previous test case, none of the three resolutions is sufficient to completely capture the induction zone within the oblique detonation. There is significant overlap between the reaction zone and the shock structure.

It is clear in this case that, while there is a small increase in the precursor shock angle before the transition to detonation, this effect plays only a minor role in driving the reaction front toward the shock. In order to examine this behavior of the reaction front more closely, an additional simulation was run using identical test conditions, though over one half the domain size: 260×200 , $\Delta x = 0.02$ mm, $\Delta y = 0.01$ mm. The pressure characteristics of the resultant flowfield are shown in Fig. 4.9. The contour plot clearly shows a series of pressure contours inclined at the Mach wave angle between the reaction and shock fronts. These contours correspond to compression waves which communicate the pressure increase due to energy release to the precursor oblique shock. Note that the pressure contours corresponding to these waves draw closer together as the reaction

front closes with the shock. The impact of these waves on the precursor shock naturally leads to the increase in shock angle shown previously. The effect of these waves on the induction zone behind the shock can be seen more clearly in the pressure distribution plot in the lower panel of the figure. Pressure profiles at two different elevations in the flowfield are shown. One profile at $Y = 0.005$ mm shows the pressure distribution along the wedge surface. As expected, the pressure is constant at the frozen post-shock value in the induction region along the surface. Additionally, after ignition, the increase in pressure due to energy release along the surface is essentially linear for much of the flowfield. In contrast, the profile at an elevation of $Y = 0.395$ mm shows markedly different behavior. The pressure behind the shock at this elevation is initially at the frozen post-shock value, but then rapidly increases due to the compression waves communicated from upstream and below in the flowfield. The increase in pressure in the induction zone along this streamline is accompanied by increases in density and temperature as well. Note that the compression immediately prior to ignition on this streamline is quite rapid.

These observations confirm, for this test case, that compression waves generated by energy release propagate upward and downstream and significantly affect the induction zone of adjacent streamlines. This compression naturally reduces the ignition delay, and appears to result in the rapid acceleration of the reaction front toward the shock, until the reaction front itself approaches the Mach wave angle. The substantial increase in pressure communicated to the reaction front also explains the sudden increase in shock angle when the reaction front intersects with the shock wave. In this case, the impact of the reaction front is sufficient to drive the shock to an angle greater than the nominal equilibrium value.

A comparison of the characteristic chemical timescales for the 16 test cases studied is shown in Fig. 4.10. Three types of symbols are used to classify the results: a filled square represents a smooth transition from the oblique shock to oblique detonation, as well as a peak shock angle in the domain less than the final equilibrium detonation wave angle. An upward facing filled triangle similarly represents a smooth oblique shock to detonation transition, but with a peak angle in the domain equal to or greater than the final equilibrium detonation wave angle. A downward facing filled triangle represents a discontinuous jump from oblique shock to detonation, and a peak wave angle in the domain greater than the final equilibrium value. These three classifications correspond to the three example cases shown previously. For reference, these results are also presented in tabular form in Table 4.1.

Lines corresponding to $\tau_{\text{equil}} = \tau_{\text{ign}}$ ($NRP = 1.0$) and $\tau_{\text{equil}} = 0.5\tau_{\text{ign}}$ ($NRP = 0.5$) are also shown in the figure. The results suggest that a rough generalization can be made over the range of conditions studied in this work. We note that all of the results which exhibit a smooth

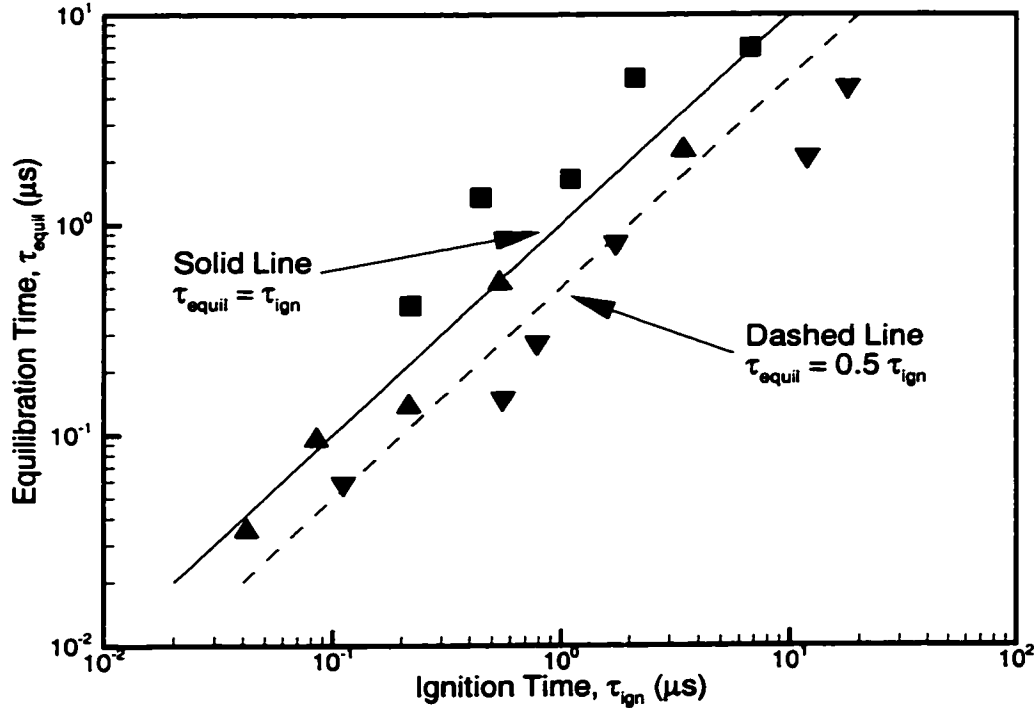


Figure 4.10: Results classified on a diagram comparing characteristic chemical timescales. Predicted characteristic times τ_{ign} and τ_{equil} are determined from constant density ignition calculations of CHEMKIN-II using calculated post-shock conditions along wedge surface. \blacksquare = smooth transition to ODW, $\beta_{peak} < \beta_{eq}$ in domain; \blacktriangle = smooth transition to ODW, $\beta_{peak} = \beta_{eq}$ in domain; \blacktriangledown = discontinuous transition to ODW, $\beta_{peak} > \beta_{eq}$ in domain.

transition to oblique detonation, and a peak wave angle in the domain less than the final equilibrium value (symbol: \blacksquare), had a longer equilibration time than ignition time ($NRP > 1.0$). All those results which exhibit a smooth transition, and also achieve the final equilibrium wave angle within the computation domain (symbol: \blacktriangle), tended to fall roughly in the range of $0.5 \lesssim NRP \lesssim 1.0$. Those results which displayed a discontinuous transition to oblique detonation, and a peak wave angle greater than the equilibrium value (symbol: \blacktriangledown), all had equilibration times significantly less than the corresponding ignition time ($NRP < 0.5$). The figure indicates that this generalization is appropriate for the H_2 -air mixture over the range of conditions studied (ignition times in an approximate range of 0.1 to 10 μs). It is important to note, however, that generalization beyond this regime would require additional studies.

The grid resolution studies show that the physical features of the flowfield do not substantially vary within resolutions $0.5\times - 1.5\times$ that of the base resolution used here. However, it is also

Wedge Angle	P_1 (atm)	τ_{ign} (μs)	τ_{equil} (μs)	NRP	OSW/ODW Transition	Peak Shock Angle
40°	0.1	0.446	1.348	3.0	Smooth	$< \beta_{eq.}$
35°	0.05	2.11	4.98	2.4	Smooth	$< \beta_{eq.}$
40°	0.2	0.219	0.413	1.9	Smooth	$< \beta_{eq.}$
35°	0.1	1.10	1.65	1.5	Smooth	$< \beta_{eq.}$
40°	0.5	0.0848	0.0952	1.1	Smooth	$= \beta_{eq.}$
30°	0.05	6.72	6.94	1.0	Smooth	$< \beta_{eq.}$
35°	0.2	0.541	0.529	0.98	Smooth	$= \beta_{eq.}$
40°	1.0	0.0415	0.0352	0.85	Smooth	$> \beta_{eq.}$
30°	0.1	3.43	2.25	0.66	Smooth	$= \beta_{eq.}$
35°	0.5	0.215	0.137	0.64	Smooth	$> \beta_{eq.}$
35°	1.0	0.111	0.059	0.53	Discontinuous	$> \beta_{eq.}$
30°	0.2	1.74	0.82	0.47	Discontinuous	$> \beta_{eq.}$
30°	0.5	0.786	0.274	0.35	Discontinuous	$> \beta_{eq.}$
30°	1.0	0.558	0.149	0.27	Discontinuous	$> \beta_{eq.}$
25°	0.1	17.8	4.5	0.25	Discontinuous	$> \beta_{eq.}$
25°	0.2	11.9	2.1	0.18	Discontinuous	$> \beta_{eq.}$

Table 4.1: Summary of results for the 16 test cases studied. Predicted characteristic times τ_{ign} and τ_{equil} are determined from constant density ignition calculations of CHEMKIN-II using calculated post-shock conditions along the wedge surface. The results are ranked in order of decreasing predicted normalized reaction parameter, $NRP = \tau_{ign}/\tau_{equil}$. Peak shock angle is the peak value within the computational domain.

clear that coarser grids tend to exhibit shorter induction zones and faster coupling of reaction and shock fronts compared to higher-resolution grids. Therefore, comparison of oblique detonation wave formation distances between different numerical and experimental studies should keep this observation in mind.

The characteristic equilibration timescale chosen here is to a certain extent arbitrary. However, in a global sense, these results clearly show the importance of energy release rates in governing the near-field transition from oblique shock-induced combustion to oblique detonation. Very fast energy release can lead to an oblique detonation which initially forms at an angle greater than the equilibrium value. While the detonation will inevitably asymptote to the equilibrium angle in the far field, the importance of detailed flowfield modeling of the near field is clear.

4.1.2 Oblique Detonation Wave Formation when $0 < \theta < \theta_{C-J}$

The discussion of shock polar theory in Chapter two showed that if the wedge angle is decreased to a value below the C-J point ($0 < \theta < \theta_{C-J}$), then an attached solution is only possible for an inert shock. Rankine-Hugoniot arguments fix the C-J speed as the lower limit for a stabilized shock wave with energy release. As the inflow velocity to an oblique shock is governed solely by the (fixed) external freestream velocity and the oblique wave angle, this limit is effectively translated into a minimum C-J wave angle on the shock polar diagram. Thus, there is a question as to the resultant flowfield when the wedge turning angle is reduced below the C-J point under exothermic conditions. Some authors (Ashford and Emanuel, 1994; Shepherd, 1994) have proposed that the flowfield would consist of an oblique C-J detonation at a wave angle of β_{C-J} , followed immediately by a steady Prandtl-Meyer expansion wave to turn the flow parallel to the wedge. This theory is based on an analogous 1-D scenario: a detonation wave driven by a piston moving at a velocity less than the C-J speed. The solution which emerges is a steady C-J detonation, followed by a rarefaction wave which expands the product gases to match the velocity of the piston (Fickett and Davis, 1979). Here, we will briefly examine this case using our numerical model, in an attempt to determine whether this theory is consistent with the observed results.

The temperature of the freestream in these results ($T_1 = 1000$ K) is considerably higher than that used previously in this Chapter. This is due to the fact that, at the small wedge angles used in this regime, the initial frozen shock is relatively weak. The higher freestream temperature allows the calculation to capture the basic features of the oblique detonation formation process in a reasonable domain size.

It is worthwhile to begin by discussing the flowfield calculated at a wedge angle designed to produce an oblique C-J detonation wave at these test conditions ($\theta = 15.03^\circ$). As this flowfield represents the upper bounding condition in this flow regime, these results form the natural reference point for comparison with calculations at wedge angles below the C-J point. Freestream conditions are $T_1 = 1000$ K, $P_1 = 1.0$ atm, $V_1 = 2500$ m/s. The domain studied was an area 72 mm \times 42 mm (360×280 , $\Delta x = 0.2$ mm, $\Delta y = 0.15$ mm). A temperature contour plot, and a corresponding plot of shock wave angle for the converged CFD solution are shown in Fig. 4.11. Also provided is a pressure contour plot, and a corresponding plot of the pressure distribution at a height of $Y = 15.07$ mm in the domain (Fig. 4.12).

There are a number of observations to note in these results. First, observe that the detonation wave initially forms at an angle below the C-J value, and then increases asymptotically toward the C-J value in the far field. Similarly, the temperature and pressure contour lines also draw increasingly parallel to the shock as the detonation reaches the C-J condition. This means that, for a certain

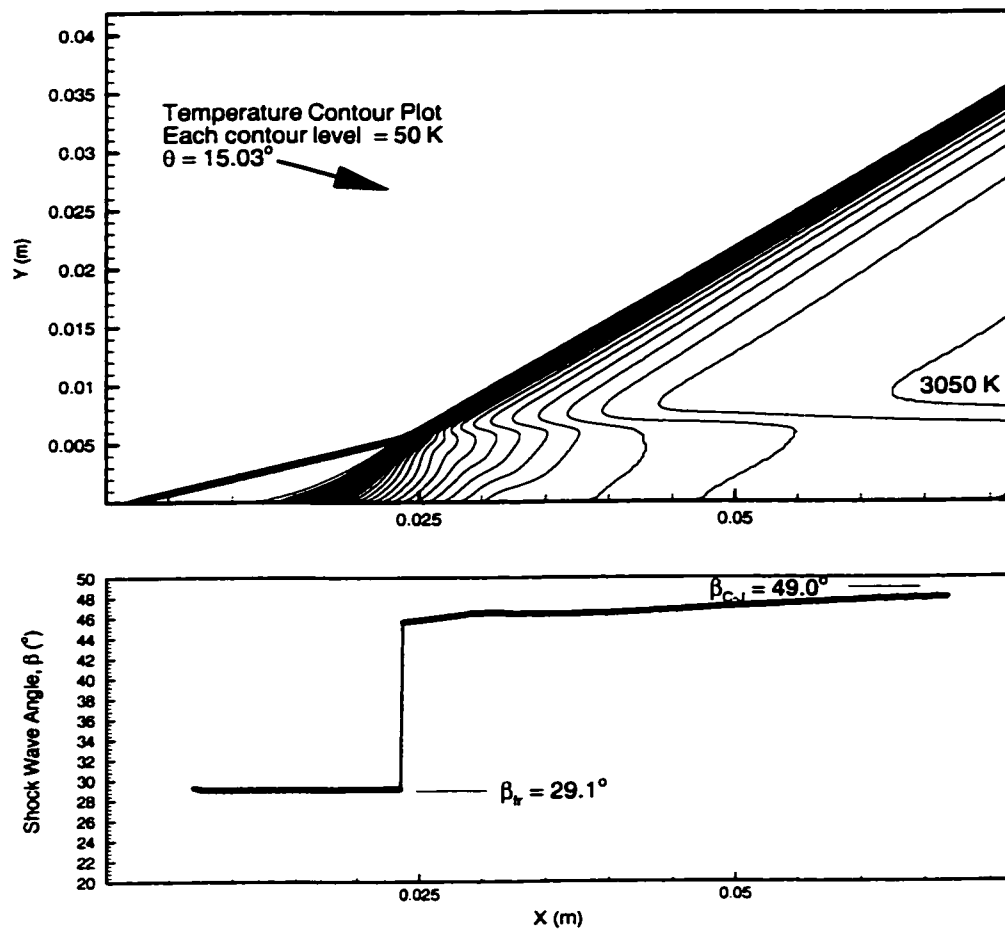


Figure 4.11: Converged CFD simulation of stoichiometric H_2 -air ($2\text{H}_2 + \text{O}_2 + 3.76\text{N}_2$) flow over a $\theta = 15.03^\circ$ wedge. $T_1 = 1000\text{ K}$, $P_1 = 1.0\text{ atm}$, $V_1 = 2500\text{ m/s}$. Upper panel: temperature contour plot. Lower panel: corresponding plot of shock wave angle as a function of grid x-coordinate.

portion of the flow, the inflow velocity into the shock is actually less than the minimum value specified for a steady, C-J solution. We know from our earlier analysis that a steady solution in one dimension is not possible below the C-J condition. However, a detonation can exist temporarily below the C-J velocity as part of an unsteady solution. Examples of this in 1-D are deflagration-to-detonation transition, and the fast galloping detonation front which forms around a blunt projectile traveling slightly below the C-J speed of the ambient combustible gas mixture. In our case here, the flow is supersonic and 2-dimensional. As a result, the energy release which influences the shock front may only do so downstream along characteristic lines. This factor, along with the finite rate of energy release behind the initial oblique detonation front, explains why the oblique detonation wave does not instantaneously form at the C-J angle, but rather adjusts to the proper angle across

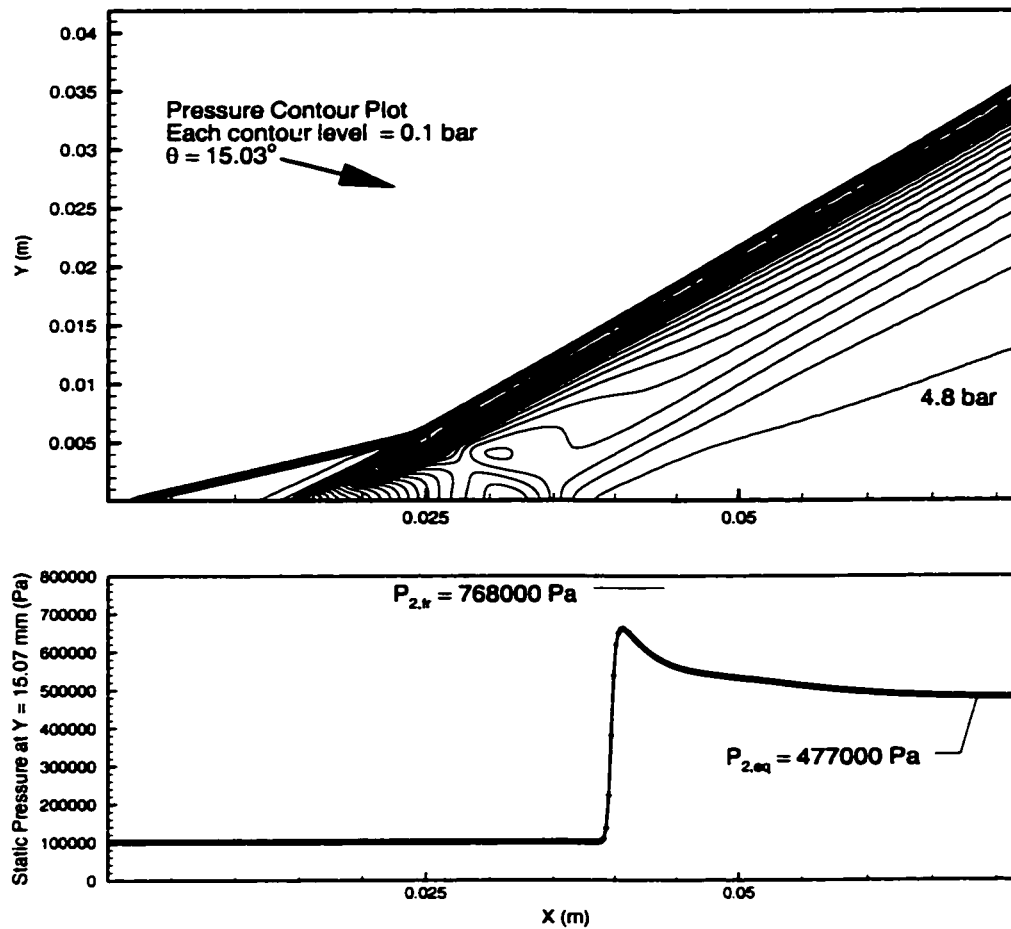


Figure 4.12: Converged CFD simulation of stoichiometric H_2 -air ($2\text{H}_2 + \text{O}_2 + 3.76\text{N}_2$) flow over a $\theta = 15.03^\circ$ wedge. $T_1 = 1000$ K, $P_1 = 1.0$ atm, $V_1 = 2500$ m/s. Upper panel: pressure contour plot. Lower panel: corresponding plot of pressure distribution as a function of grid x -coordinate at $Y = 15.07$ mm.

the flowfield. In a broader sense, this result also demonstrates the well-known similarity between 1-D, unsteady compressible flows and 2-D hypersonic flows.

The pressure distribution plot, at a fixed y -coordinate of 15.07 mm, shows a typical ZND detonation structure consisting of a peak pressure immediately behind the shock, followed by pressure decay as energy release occurs downstream. As the shock has not yet quite achieved the final C-J wave angle at this location, the peak pressure in the solution is below the value predicted (using frozen thermochemistry) for the induction zone at the C-J point. Additionally, as was evident in the grid resolution tests in the previous section, the finite thickness of the oblique shock in the model

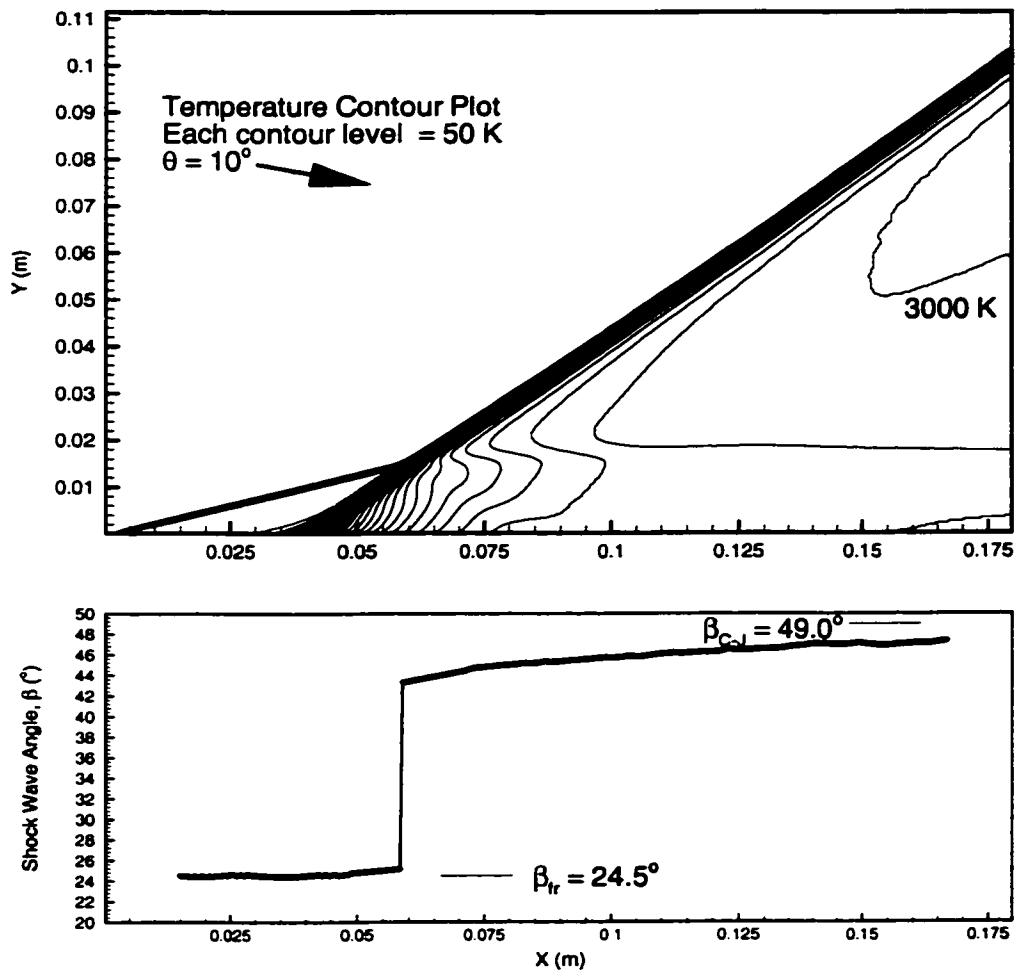


Figure 4.13: Converged CFD simulation of stoichiometric H_2 -air ($2\text{H}_2 + \text{O}_2 + 3.76\text{N}_2$) flow over a $\theta = 10^\circ$ wedge. $T_1 = 1000\text{ K}$, $P_1 = 1.0\text{ atm}$, $V_1 = 2500\text{ m/s}$. Upper panel: temperature contour plot. Lower panel: corresponding plot of shock wave angle as a function of grid x-coordinate.

allows some chemistry to take place within the shock, and makes complete resolution of the induction zone within an oblique detonation more difficult. Note, however, that the pressure behind the oblique detonation decays to the expected equilibrium C-J value.

We turn now to consider the results when $\theta < \theta_{\text{C-J}}$. The test case considered here used the same freestream conditions ($T_1 = 1000\text{ K}$, $P_1 = 1.0\text{ atm}$, $V_1 = 2500\text{ m/s}$) as the previous C-J control case, with a wedge angle of 10° . The domain studied was an area $180\text{ mm} \times 112\text{ mm}$ (360×280 , $\Delta x = 0.5\text{ mm}$, $\Delta y = 0.4\text{ mm}$). A temperature contour plot, and a corresponding plot of shock wave angle for the converged CFD solution are shown in Fig. 4.13. A pressure contour plot is shown in Fig. 4.14.

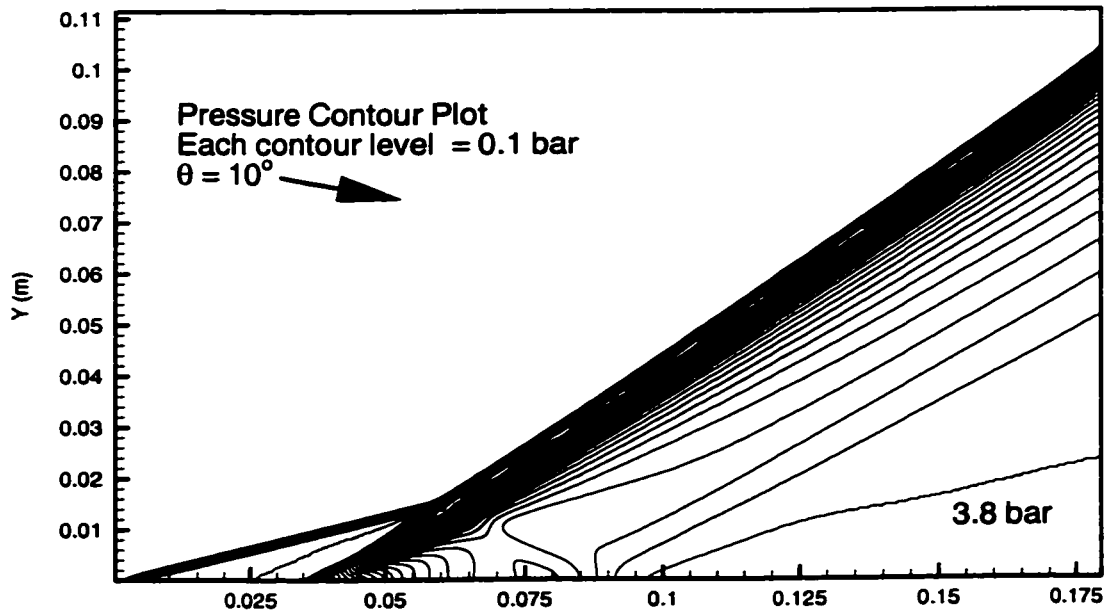


Figure 4.14: Pressure contour plot of a converged CFD simulation of stoichiometric H_2 -air ($2\text{H}_2 + \text{O}_2 + 3.76\text{N}_2$) flow over a $\theta = 10^\circ$ wedge. $T_1 = 1000\text{ K}$, $P_1 = 1.0\text{ atm}$, $V_1 = 2500\text{ m/s}$.

As in our C-J benchmark case, note that the detonation wave slowly increases toward the C-J angle throughout the flowfield. As the domain in this calculation is roughly twice the size of the previous case, the rate of adjustment to the C-J angle appears to be significantly slower. Additionally, unlike the C-J benchmark case, here the temperature and pressure contour lines well-behind the detonation front slowly diverge away from the wave. This indicates that the proposed model of an oblique C-J detonation wave followed by a Prandtl-Meyer expansion fan may be reasonably accurate. Plots of the pressure and vertical velocity component distribution for this case are shown in Fig. 4.15, at fixed y -coordinates of 30.02 mm and 50.02 mm. Both pressure profiles once again exhibit the pressure decay behavior typical of a ZND detonation structure. Note, however, that the pressure decays below the equilibrium C-J value. Careful examination of the profiles reveals that the length required for the pressure to decay to a particular value after the detonation front is greater in the higher elevation profile. This confirms that the expansion wave steadily diverges behind the detonation. A corresponding plot of the vertical velocity component at both elevations also confirms that the gas does not draw parallel to the wedge surface ($V \rightarrow 0$) until pressure has reached equilibrium. It is important to point out that, at least in the near field, the two physical processes of expansion due to energy release behind the detonation, and the Prandtl-Meyer expansion which

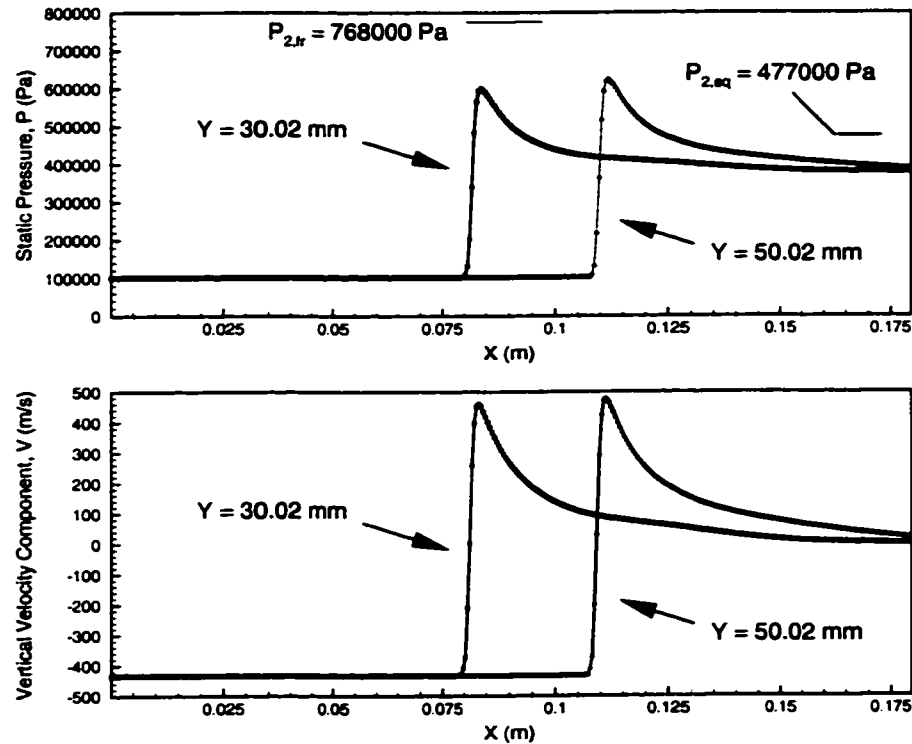


Figure 4.15: Plots of flowfield properties as a function of grid x -coordinate at fixed $Y = 48.65$ mm and $Y = 97.65$ mm (from Figs. 4.13 and 4.14). Upper panel: Static pressure distribution. Lower panel: Vertical velocity component distribution

turns the flow parallel to the wedge surface, appear to be at least partially mixed together. An additional simulation run over a larger domain of $720 \text{ mm} \times 560 \text{ mm}$ (360×280 , $\Delta x = 2.0 \text{ mm}$, $\Delta y = 2.0 \text{ mm}$) confirms that the detonation wave continues to asymptote to the C-J angle.

These results indicate, within the accuracy of the numerical model, that an oblique detonation wave can be successfully initiated and formed at wedge angles below the C-J wedge angle. The oblique detonation can potentially form at an angle less than the C-J wave angle in the near field, though the wave will steadily asymptote to the C-J angle moving into the far field. A steadily diverging expansion wave serves to turn the flow parallel to the wedge surface. Thus, the theoretical model of an oblique C-J detonation followed by a Prandtl-Meyer expansion wave for this regime appears to be approximately correct. At least in the near field, however, where the finite-rate of energy release behind the detonation front occupies a significant lengthscale in the domain, the equilibration zone and expansion wave appear to be partially mixed together.

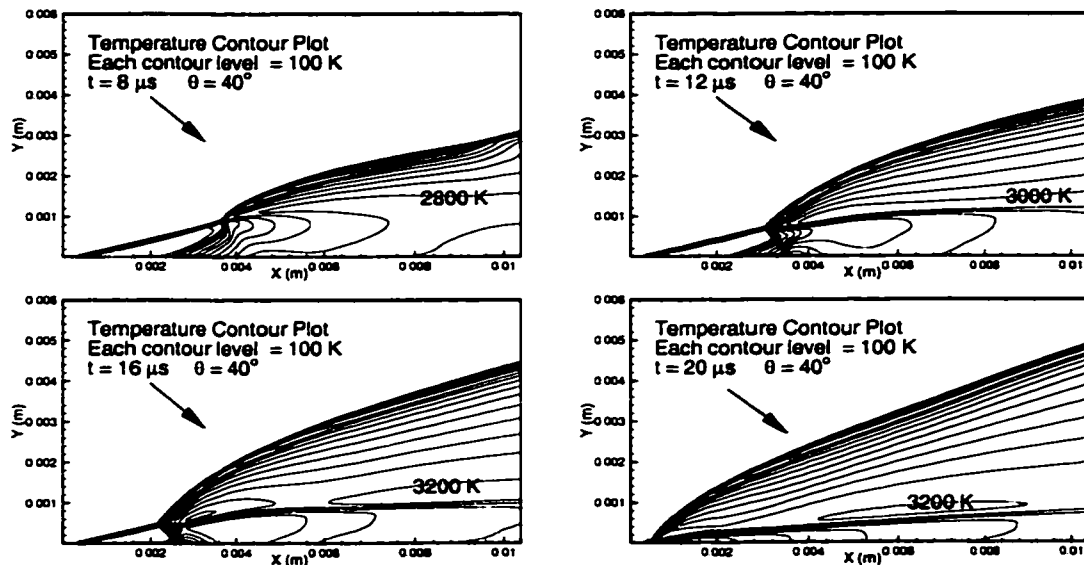


Figure 4.16: Temperature contour plots depict the time history of H_2 -air ($2\text{H}_2 + \text{O}_2 + 3.76\text{N}_2$) flow over a $\theta = 40^\circ$ wedge. $T_1 = 300\text{ K}$, $P_1 = 0.2\text{ atm}$, $V_1 = 2500\text{ m/s}$. The detachment point on the equilibrium polar curve for these conditions is $\theta_{\text{det,eq}} \simeq 32.6^\circ$.

4.1.3 Oblique Detonation Wave Formation when $\theta_{\text{det,eq}} < \theta < \theta_{\text{det,fr}}$

Our discussion of shock polar theory in Chapter two showed that when the wedge turning angle is increased above the detachment point on the equilibrium polar diagram, only a frozen shock polar solution is possible. Thus, the initial frozen shock attached to the wedge tip is followed by a locally detached detonation wave. However, as the flow behind a detached shock or detonation wave is subsonic, there is question as to whether this flow configuration is stable. Here we will briefly examine this scenario using the numerical model.

The results shown in Fig. 4.16 are typical. The figure shows the time history of the flowfield for stoichiometric H_2 -air over a $\theta = 40^\circ$ wedge. Freestream conditions are $T_1 = 300\text{ K}$, $P_1 = 0.2\text{ atm}$, $V_1 = 2500\text{ m/s}$. The domain studied was an area $10.4\text{ mm} \times 6\text{ mm}$ (260×200 , $\Delta x = 0.04\text{ mm}$, $\Delta y = 0.03\text{ mm}$). The detachment point on the equilibrium polar curve for these conditions is $\theta_{\text{det,eq}} \simeq 32.6^\circ$, clearly less than the wedge angle studied here. As expected in this case, after the reaction front intersects the shock, a locally detached detonation develops above the intersection point. However, in this case, the detonation rapidly advances toward the front of the wedge. Note that, by $t = 16\ \mu\text{s}$, the detached detonation front has advanced further forward than the original ignition point on the wedge surface. By $t = 20\ \mu\text{s}$, the detached detonation has reached the wedge tip, resulting in a detached detonation front throughout the entire flowfield. Recall from our discussion

in Chapter two that the final standoff distance and curvature of a detached shock or detonation is governed by the physical size of the wedge. Due to the simple zero-gradient outflow boundary conditions used in this study, the wedge is effectively semi-infinite for the purposes of detached flows. Therefore, the primary result of this calculation is the fact that the locally detached detonation does not stabilize, and advances to the wedge tip to dominate the entire flowfield.

Additional simulations run at lower pressures ($P_1 = 0.1$ and 0.05 atm) confirm that, if the energy release rate is sufficient to drive the reaction front into the shock and create a locally-detached detonation, the detonation will inevitably propagate forward toward the wedge tip. The time required for the detonation to reach the tip increases significantly at lower pressures. This is due not only to the greater length of the induction zone, which scales roughly with $1/P$, but also to the slower rate of energy release (equilibration time) at lower pressures. It is fair to point out that, in a scenario where the detached detonation advances relatively slowly, a numerical model accounting for the true size of the wedge forebody would be more appropriate.

4.2 Comparison with Experimental Results

In order to develop an appreciation for the accuracy of the numerical model, it is important to compare the computational results with experimental data. In this section, we will briefly review the characteristics of selected experimental results, and then compare the results with the numerical model at identical nominal freestream conditions. The experimental results are OH PLIF and schlieren flow visualization data of $H_2/O_2/N_2$ flows over a 40° wedge body. Two cases are studied, differentiated by the level of nitrogen dilution: A) $2 H_2 + 1 O_2 + 17 N_2$ and B) $2 H_2 + 1 O_2 + 12 N_2$. Both test cases are in the third regime, $\theta_{det,eq} < \theta < \theta_{det,fr}$. The detachment point on the equilibrium polar curve for case A is $\theta_{det,eq} \simeq 37.0^\circ$, and for case B is $\theta_{det,eq} \simeq 34.3^\circ$. The original schlieren and OH PLIF images for both cases are shown in Fig. 4.17a and Fig. 4.17c. The PLIF result has been overlaid on the schlieren image. The schlieren result was acquired $\sim 2 \mu s$ after the PLIF image, providing an effectively instantaneous picture of the flow field. The attached oblique shock wave is clearly shown in the greyscale schlieren images, whereas the overlaid OH PLIF results show the reaction front with a red and yellow color table. The images have been slightly clipped at the right edge of the laser sheet; a small additional area is visible in the rotated images of Figs. 4.18 and 4.19.

Although the wedge angle in case A is greater than the detachment point on the equilibrium polar for that condition, the reaction front does not intersect with the oblique shock within the length of the wedge forebody. Indeed, the imaging results show that there is a slight divergence between the reaction and shock fronts. This image was captured $\sim 140 \mu s$ after the start of the test

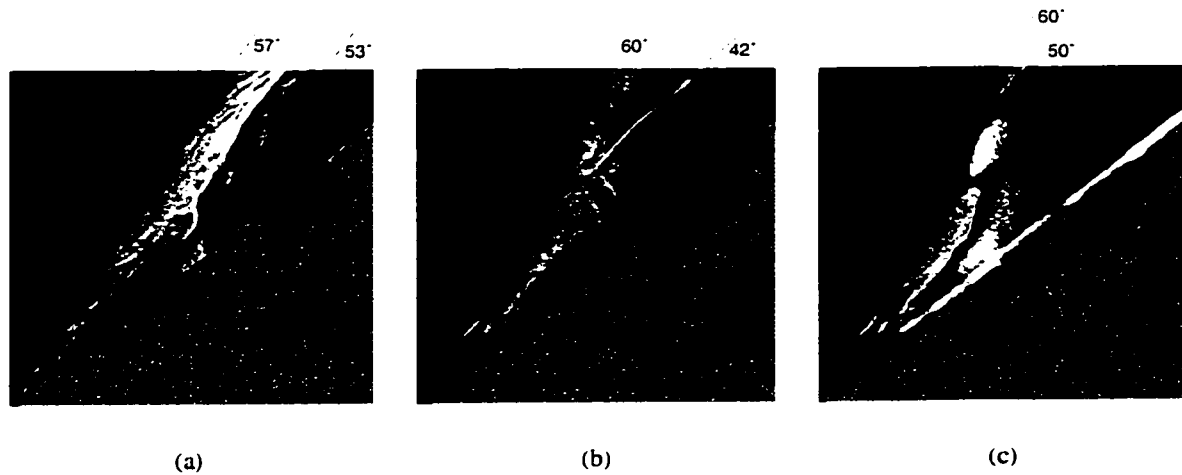


Figure 4.17: OH PLIF and schlieren images of shock-induced combustion on a 40° wedge for flow condition 1: (a) Overlaid PLIF and schlieren images of case A: $2\text{H}_2 + 1\text{O}_2 + 17\text{N}_2$, $T_1 = 292\text{ K}$, $P_1 = 0.12\text{ atm}$, $V_1 = 2130\text{ m/s}$ ($M_1 = 5.85$) (b) Schlieren image of case B: $2\text{H}_2 + 1\text{O}_2 + 12\text{N}_2$, $T_1 = 282\text{ K}$, $P_1 = 0.12\text{ bar}$, $V_1 = 2130\text{ m/s}$ ($M_1 = 5.85$) (c) Overlaid PLIF and schlieren images of case B. The total forebody length pictured in the images is 30.5 mm. The location of the pressure transducer is shown in blue. In both cases the two images were acquired nearly simultaneously ($\Delta t < 2\ \mu\text{s}$).

time in the experiment. The shock remains at a constant angle of $\beta = 57^\circ$ throughout the imaged region. While there is some oscillation in the reaction front, the average angle across the image is 53° . The relatively slow rate of energy release for this mixture and test condition evidently leads to a minimal impact from the reaction front on the observed flowfield, a conclusion supported by the fact that the measured surface pressure agrees closely with the value on the frozen shock polar at $\theta = 40^\circ$.

In case B (Fig. 4.17b and 4.17c), a more sensitive mixture was used which resulted in rapid steepening of the reaction front, and interaction with the original oblique shock. The larger rate of energy release here, compared to the previous case, leads to a significant impact from the reaction front on the flowfield. Figure 4.17b is the original schlieren image without a PLIF overlay, and divided by a background image acquired just before the test run. This procedure minimizes the effect (on the image) of pits and blemishes in the viewing section windows. This result was obtained $\sim 140\ \mu\text{s}$ after the start of the test time, and exhibits features similar to those observed in the simulations of $\theta_{\text{det,eq}} < \theta < \theta_{\text{det,fr}}$ flow in the previous section. Examination of these images reveals that there are two primary features which emerge from the interaction region: a locally detached detonation which soon splits into an uncoupled shock and reaction front, and a slip line (at 42°)

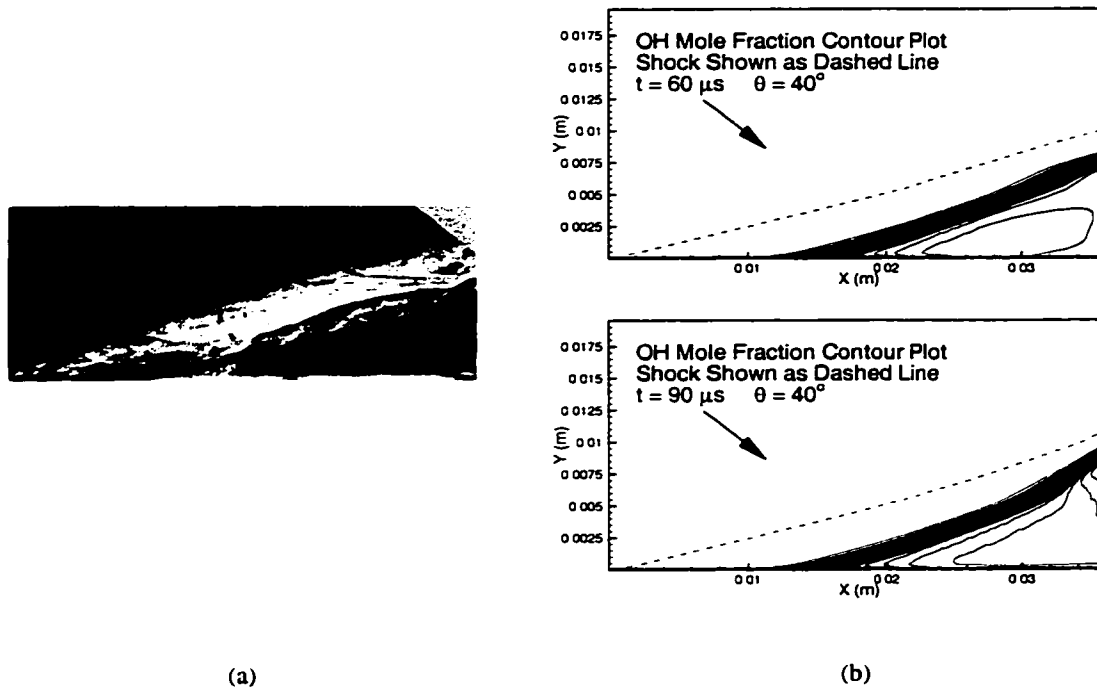


Figure 4.18: Comparison of rotated experimental OH PLIF and schlieren imaging results (a) with the numerical model (b). Gas Mixture: $2\text{H}_2 + 1\text{O}_2 + 17\text{N}_2$. Freestream conditions: $P_1 = 0.12$ bar, $T_1 = 292$ K, $V_1 = 2130$ m/s ($M_1 = 5.85$). The OH PLIF result is overlaid on the schlieren image. The two images were acquired nearly simultaneously ($\Delta t < 2 \mu\text{s}$). The grey triangle in the upper-right corner of the experimental image blocks out the blank space generated by rotation of the original image.

separating the flow above and below the interaction point.

The OH PLIF and schlieren imaging results are compared with the numerical model in Figs. 4.18 (Case A) and 4.19 (Case B). The imaging results have been rotated by 40° , and scaled appropriately to enable comparison in the reference frame of the numerical model. The domain studied was an area designed to capture the entire forebody length of the experimental wedge test body: $36 \text{ mm} \times 20 \text{ mm}$ (360×200 , $\Delta x = 0.1 \text{ mm}$, $\Delta y = 0.1 \text{ mm}$). There is generally good agreement between the imaging results and the numerical model for Case A. The numerical model converged to a steady solution by $t = 90 \mu\text{s}$. Differences in initial conditions make a direct comparison of the simulation time to the experimental time impossible. However, the $90 \mu\text{s}$ convergence time of the simulation does indicate that a steady flowfield could have been realized within the $\sim 150 \mu\text{s}$ test time of the experiment. In comparison to the experimental results, the numerical model has a slightly longer induction length along the wedge surface. Additionally, the reaction front in the model slowly draws

closer to the shock, compared to the slight divergence and oscillation of the shock and reaction front evidenced in the imaging results. In general, however, the model captures the essential features of the experimental results. It is important to recognize that the nominal freestream conditions are at best known to within 3–5% accuracy. Moreover, the freestream is assumed uniform across the entire computational domain. Therefore, the model does not account for freestream nonuniformities which may be present in the experimental results.

Comparison of the OH PLIF and schlieren imaging results with the numerical model in Case B is complicated by the unsteady nature of the numerical solution. Numerical results are shown at three different times from the start of the simulation. Again, direct comparison of the experimental imaging time (measured from the start of the test time) with the simulation time is not practical. However, we do observe that the model captures some of the essential features of the experimental result. In both sets of results a clear, locally detached detonation wave is formed after the reaction front intersects the oblique shock. The discontinuous increase in shock angle also leads to a contact surface separating the flow above and below the intersection point in both results. There are also some differences between the images and the model. Again, the induction length on the wedge surface in the model is slightly larger than the induction length in the experimental result. Additionally, there is a clear decoupling of the shock and reaction fronts a short distance above the interaction point in the images. While there is some analogous decoupling present in the simulation at $t = 60 \mu\text{s}$ and $t = 90 \mu\text{s}$, it is not as distinct as that in the experiment. In addition to the concerns regarding freestream conditions and uniformity described above, it is fair to expect the exact decoupling point to be very sensitive to accurate resolution of the induction zone within an oblique detonation wave. As we have seen previously in this study, the grid resolutions used in these simulations are typically sufficient to resolve the energy-release and equilibration process after the shock front reasonably well. However, the induction zone immediately behind the shock is typically at best only partially-resolved, and is likely insufficient to fully capture the decoupling phenomena at the same point in the flowfield as in the experiment. Aside from this last issue, however, the model captures the essential features of the experiments.

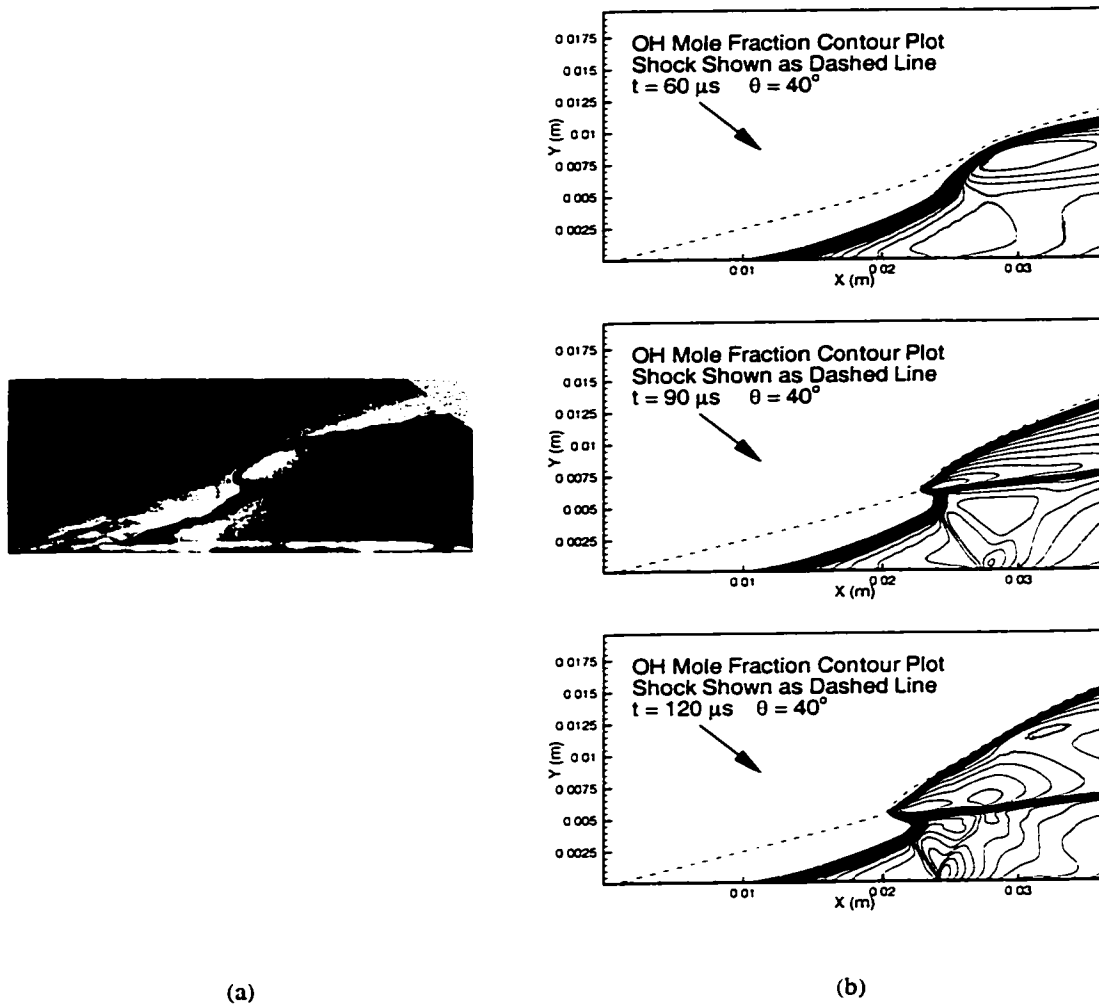


Figure 4.19: Comparison of rotated experimental OH PLIF and schlieren imaging results (a) with the numerical model (b). Gas mixture: $2\text{H}_2 + 1\text{O}_2 + 12\text{N}_2$. Freestream conditions: $P_1 = 0.12$ bar, $T_1 = 282$ K, $V_1 = 2130$ m/s ($M_1 = 5.85$). The OH PLIF result is overlaid on the schlieren image. The two images were acquired nearly simultaneously ($\Delta t < 2\ \mu\text{s}$). The grey triangle in the upper-right corner of the experimental image blocks out the blank space generated by rotation of the original image.

Chapter 5

Conclusions

5.1 Summary

This work grows out of interest in oblique detonation waves for high-speed propulsion applications. The study is primarily computational in nature, but is supplemented in one regime by experimental data. The computational results were generated by a dedicated multi-species, finite-rate chemistry CFD code developed by the author. In order to develop an appreciation for the accuracy of the model, the numerical results were compared to OH PLIF and schlieren imaging results obtained in the Stanford expansion tube facility.

Discussion of oblique detonation waves is dominated by Rankine-Hugoniot and shock polar theory, which provides oblique shock solutions in the limiting cases of frozen and equilibrium chemistry. The theory predicts that a steady, straight oblique detonation wave may be stabilized on a wedge only when the wedge turning angle, θ satisfies the condition $\theta_{C-J} < \theta < \theta_{det,eq}$. The wedge angle θ_{C-J} signifies the angle which would produce a oblique detonation with an inflow velocity equal to the Chapman-Jouguet detonation speed. The wedge angle $\theta_{det,eq}$ is the detachment point on the equilibrium shock polar. Within this regime, an actual supersonic, exothermic wedge flow will typically involve an initial frozen oblique shock attached to the tip of the wedge, which transitions to an oblique detonation wave as energy is released by combustion. The study here investigated the critical role of the energy-release rate in governing the characteristics of the transition process.

A series of 16 test cases was studied using the numerical model, for the same test gas mixture, freestream velocity and temperature throughout, but varying the wedge angle and freestream pressure in order to vary the energy release rate. The domain studied in each case was scaled to $5\times$ the calculated ignition length along the wedge surface. Predicted characteristic ignition times ($\tau_{ign} = \tau_{\Delta T=0.01\Delta T_{max}}$) and equilibration times ($\tau_{equil} = \tau_{\Delta T=0.50\Delta T_{max}-0.01\Delta T_{max}}$) were computed for

each case using calculated post shock conditions and constant density CHEMKIN-II calculations. A prediction normalized reaction parameter was also calculated from the ratio of these two timescales ($NRP = \tau_{\text{equil}}/\tau_{\text{ign}}$) for each case. The results were qualitatively classified into three categories. One category exhibited a smooth transition from oblique shock to detonation, with a peak wave angle in the domain studied less than the value predicted by equilibrium shock polar theory. In these results, the primary mechanism drawing the reaction front closer to the shock appeared to be the increase in the angle of the shock itself. The predicted characteristic equilibration time was greater than the corresponding ignition time for all results in each of these results of this regime ($NRP > 1.0$). A second category of results also exhibited a smooth transition for oblique shock to detonation, but had a peak angle in the domain equal to or greater than the equilibrium shock polar value. In cases where the peak angle was greater than the equilibrium value, the detonation wave relaxed to the equilibrium wave angle in the far field. In each case of this regime, the predicted characteristic equilibration time was between roughly one-half to equal to the corresponding ignition time ($0.5 \lesssim NRP \lesssim 1.0$). A third category of results exhibited a rapid acceleration of the reaction front toward the shock, and a consequent discontinuous transition from oblique shock to detonation. The detonation wave initially formed at an angle greater than the equilibrium wave angle in each of these cases, but relaxed to the equilibrium value in the far field. Examination of results in this regime showed that compression waves generated by energy release have a significant role in accelerating the reaction front toward the shock. Results in this regime each had an equilibration time significantly smaller than the corresponding ignition time ($NRP < 0.5$). It is important to note that these rough classifications held over the range of conditions studied in this work (stoichiometric H_2 -air, ignition times ranging from 0.1 – $10 \mu\text{s}$). Extension to a wider range of mixtures and conditions would require additional study.

The grid resolution studies in this regime show that the physical features of the flowfield do not substantially vary within resolutions $0.5\times$ – $1.5\times$ that of the base resolution used here. However, it is also clear that coarser grids tend to exhibit shorter induction zones and faster coupling of reaction and shock fronts compared to higher-resolution grids. Therefore, comparison of oblique detonation wave formation distances between different numerical and experimental studies should keep this observation in mind.

Shock polar theory gives no solution when the wedge turning angle is less than the C-J point ($0 < \theta < \theta_{\text{C-J}}$). The numerical model was used to investigate whether a solution comprising a C-J oblique detonation wave, followed by an expansion fan to turn the flow parallel to the surface, was theoretically possible. The results indicated, within the accuracy of the numerical model, that an oblique detonation wave could be successfully initiated and formed at wedge angles below the C-J

wedge angle. The oblique detonation can potentially form at an angle less than the C-J wave angle in the near field, though the wave will steadily asymptote to the C-J angle moving into the far field. A steadily diverging expansion wave serves to turn the flow parallel to the wedge surface. Thus, the theoretical model of an oblique C-J detonation followed by a Prandtl-Meyer expansion wave for this regime appears to be approximately correct. At least in the near field, however, where the finite-rate of energy release behind the detonation front occupies a significant lengthscale in the domain, the equilibration zone and expansion wave appear to be partially mixed together.

Shock polar theory also shows that when the wedge turning angle is increased above the detachment point on the equilibrium polar diagram, only a frozen shock polar solution is possible. Thus, the initial frozen shock attached to the wedge tip is followed by a locally detached detonation wave. The numerical model was used to investigate whether the detached detonation can remain stabilized on the wedge surface. The results confirmed that, if the energy release rate is sufficient to drive the reaction front into the shock and create a locally-detached detonation, the detonation will inevitably propagate forward toward the wedge tip. The time required for the detonation to reach the tip increases significantly at lower pressures. It is important to point out that the numerical model used here does not account for the finite-extent of the wedge forebody and expansion corner. An improved model which did account for these factors would enable a more detailed study of this flow regime, particularly the effect of finite wedge size on the locally detached detonation wave.

Comparisons of the numerical model with experimental OH PLIF and schlieren flow visualization results show generally good agreement. In both test cases studied, the surface ignition length in the model was slightly larger than that observed in the experiment. There were also deviations in the reaction front path in the model compared to the flow visualization results. Considering that the experimental freestream conditions are not known perfectly however, the model clearly captures the essential features shown in the experiments.

5.2 Recommendations for Future Work

The CFD code used in this study can be easily extended to model conical flows. The shock polar diagram for conical flows is quite similar to the 2-D wedge scenario. Therefore, a study of the three polar regimes in conical flows would be useful, particularly since conical flow is more applicable to some potential propulsion applications, such as ram accelerators. The conical polar diagram also permits a wider range of turning angles before detachment compared to 2-D wedge flow. This would facilitate experimental validation in the second regime, below the equilibrium detachment point.

There are a number of ways in which the numerical model could be improved. The code uses

a simple Cartesian grid aligned with the wedge surface. An adaptive polar grid, if coupled with shock-fitting of the main oblique shock front, would likely yield improved resolution of the induction zone within the oblique detonation. It would also be worthwhile to extend the numerical model to an arbitrary grid geometry in order to accurately model the expansion corner of a real test body. Extension of the code to the full Navier-Stokes equations would enable study of the impact of viscous effects on the ignition length on the wedge forebody. These effects would become increasingly important at higher enthalpy flow conditions.

Appendix A

Thermodynamic Model

This appendix provides details of the thermodynamic model used in the calculations of this work. The molecular weights, heats of formation, and curve-fit data are obtained from the McBride et al. (1993). The molecular gas constant, R , is defined as

$$R = 8314.41 \frac{\text{J}}{\text{molK}} \quad (\text{A.1})$$

The molecular weights and heats of formation of the nine species used in the calculations are given in Table A.1. These values are based on a standard reference temperature 298.15 K, and a standard pressure of 1 bar.

The specific heat, enthalpy, and entropy of each species in these calculations is computed using polynomial curve-fits in the following form:

$$\frac{C_p}{R} = a_1 + a_2T + a_3T^2 + a_4T^3 + a_5T^4 \quad (\text{A.2})$$

$$\frac{H^0}{RT} = a_1 + \frac{1}{2}a_2T + \frac{1}{3}a_3T^2 + \frac{1}{4}a_4T^3 + \frac{1}{5}a_5T^4 + a_6\frac{1}{T} \quad (\text{A.3})$$

$$\frac{S^0}{R} = a_1 \ln T + a_2T + \frac{1}{2}a_3T^2 + \frac{1}{3}a_4T^3 + \frac{1}{4}a_5T^4 + a_7 \quad (\text{A.4})$$

The curve-fit coefficients for each species are listed in Tables A.2, A.3, and A.4.

Species	Molecular Weight (kg/kmol)	$\Delta_f H^0(298.15)/R$ (K)
N ₂	28.01340	$0.00000000 \times 10^{+00}$
O ₂	31.99880	$0.00000000 \times 10^{+00}$
H ₂	2.01588	$0.00000000 \times 10^{+00}$
OH	17.00734	$0.47319052 \times 10^{+04}$
H ₂ O	18.01528	$-0.29085167 \times 10^{+05}$
H	1.00794	$0.26219462 \times 10^{+05}$
O	15.99940	$0.29968452 \times 10^{+05}$
HO ₂	33.00674	$0.15096682 \times 10^{+04}$
H ₂ O ₂	34.01468	$-1.63425145 \times 10^{+04}$

Table A.1: Molecular weight and heat of formation data for species used in this work (McBride et al., 1993).

N ₂		
Parameter	200 K ≤ T < 1000 K	1000 K ≤ T ≤ 6000 K
a ₁	0.29525763 × 10 ⁺⁰¹	0.35310053 × 10 ⁺⁰¹
a ₂	0.13969006 × 10 ⁻⁰²	-0.12366099 × 10 ⁻⁰³
a ₃	-0.49263169 × 10 ⁻⁰⁶	-0.50299944 × 10 ⁻⁰⁶
a ₄	0.78601037 × 10 ⁻¹⁰	0.24353061 × 10 ⁻⁰⁸
a ₅	-0.46075532 × 10 ⁻¹⁴	-0.14088123 × 10 ⁻¹¹
a ₆	-0.92394864 × 10 ⁺⁰³	-0.10469763 × 10 ⁺⁰⁴
a ₇	0.58718925 × 10 ⁺⁰¹	0.29674747 × 10 ⁺⁰¹

O ₂		
Parameter	200 K ≤ T < 1000 K	1000 K ≤ T ≤ 6000 K
a ₁	0.36645375 × 10 ⁺⁰¹	0.37825246 × 10 ⁺⁰¹
a ₂	0.64809452 × 10 ⁻⁰³	-0.29962626 × 10 ⁻⁰²
a ₃	-0.13493979 × 10 ⁻⁰⁶	0.98439984 × 10 ⁻⁰⁵
a ₄	0.18738921 × 10 ⁻¹⁰	-0.96778469 × 10 ⁻⁰⁸
a ₅	-0.11169387 × 10 ⁻¹⁴	0.32429006 × 10 ⁻¹¹
a ₆	-0.12171837 × 10 ⁺⁰⁴	-0.10639621 × 10 ⁺⁰⁴
a ₇	0.33959041 × 10 ⁺⁰¹	0.36569569 × 10 ⁺⁰¹

H ₂		
Parameter	200 K ≤ T < 1000 K	1000 K ≤ T ≤ 6000 K
a ₁	0.29328658 × 10 ⁺⁰¹	0.23443311 × 10 ⁺⁰¹
a ₂	0.82660797 × 10 ⁻⁰³	0.79805208 × 10 ⁻⁰²
a ₃	-0.14640234 × 10 ⁻⁰⁶	-0.19478151 × 10 ⁻⁰⁴
a ₄	0.15410036 × 10 ⁻¹⁰	0.20157209 × 10 ⁻⁰⁷
a ₅	-0.68880443 × 10 ⁻¹⁵	-0.73761176 × 10 ⁻¹¹
a ₆	-0.81306560 × 10 ⁺⁰³	-0.91793517 × 10 ⁺⁰³
a ₇	-0.10243289 × 10 ⁺⁰¹	0.68301024 × 10 ⁺⁰⁰

Table A.2: Curve fit parameters for thermodynamic model of N₂, O₂, and H₂ (McBride et al., 1993).

OH		
Parameter	$200 \text{ K} \leq T < 1000 \text{ K}$	$1000 \text{ K} \leq T \leq 6000 \text{ K}$
a_1	$0.28386463 \times 10^{+01}$	$0.39920154 \times 10^{+01}$
a_2	$0.11072555 \times 10^{-02}$	$-0.24013175 \times 10^{-02}$
a_3	$-0.29391482 \times 10^{-06}$	$0.46179384 \times 10^{-05}$
a_4	$0.42052394 \times 10^{-10}$	$-0.38811333 \times 10^{-08}$
a_5	$-0.24216888 \times 10^{-14}$	$0.13641147 \times 10^{-11}$
a_6	$0.39435215 \times 10^{+04}$	$0.36146436 \times 10^{+04}$
a_7	$0.58445255 \times 10^{+01}$	$-0.10392546 \times 10^{+00}$

H ₂ O		
Parameter	$200 \text{ K} \leq T < 1000 \text{ K}$	$1000 \text{ K} \leq T \leq 6000 \text{ K}$
a_1	$0.26757562 \times 10^{+01}$	$0.41986406 \times 10^{+01}$
a_2	$0.29753576 \times 10^{-02}$	$-0.20364341 \times 10^{-02}$
a_3	$-0.77486389 \times 10^{-06}$	$0.65204021 \times 10^{-05}$
a_4	$0.94649965 \times 10^{-10}$	$-0.54879706 \times 10^{-08}$
a_5	$-0.42837663 \times 10^{-14}$	$0.17719782 \times 10^{-11}$
a_6	$-0.29885735 \times 10^{+05}$	$-0.30294077 \times 10^{+05}$
a_7	$0.68897133 \times 10^{+01}$	$-0.84903221 \times 10^{+00}$

H		
Parameter	$200 \text{ K} \leq T < 1000 \text{ K}$	$1000 \text{ K} \leq T \leq 6000 \text{ K}$
a_1	$0.25000029 \times 10^{+01}$	$0.25000000 \times 10^{+01}$
a_2	$-0.56490204 \times 10^{-08}$	$0.00000000 \times 10^{+00}$
a_3	$0.36301780 \times 10^{-11}$	$0.00000000 \times 10^{+00}$
a_4	$-0.91944332 \times 10^{-15}$	$0.00000000 \times 10^{+00}$
a_5	$0.79487765 \times 10^{-19}$	$0.00000000 \times 10^{+00}$
a_6	$0.25474086 \times 10^{+05}$	$0.25474087 \times 10^{+05}$
a_7	$-0.44671548 \times 10^{+00}$	$-0.44669985 \times 10^{+00}$

Table A.3: Curve fit parameters for thermodynamic model of OH, H₂O, and H (McBride et al., 1993).

O		
Parameter	$200 \text{ K} \leq T < 1000 \text{ K}$	$1000 \text{ K} \leq T \leq 6000 \text{ K}$
a_1	$0.25436369 \times 10^{+01}$	$0.31682720 \times 10^{+01}$
a_2	$-0.27315581 \times 10^{-04}$	$-0.32793260 \times 10^{-02}$
a_3	$-0.41905464 \times 10^{-08}$	$0.66430541 \times 10^{-05}$
a_4	$0.49547499 \times 10^{-11}$	$-0.61280412 \times 10^{-08}$
a_5	$-0.47954106 \times 10^{-15}$	$0.21126471 \times 10^{-11}$
a_6	$0.29225764 \times 10^{+05}$	$0.29122010 \times 10^{+05}$
a_7	$0.49222771 \times 10^{+01}$	$0.20518892 \times 10^{+01}$

HO ₂		
Parameter	$200 \text{ K} \leq T < 1000 \text{ K}$	$1000 \text{ K} \leq T \leq 6000 \text{ K}$
a_1	$0.41722644 \times 10^{+01}$	$0.43018319 \times 10^{+01}$
a_2	$0.18811847 \times 10^{-02}$	$0.17618975 \times 10^{-15}$
a_3	$-0.34628095 \times 10^{-06}$	$0.61836632 \times 10^{+02}$
a_4	$0.19466650 \times 10^{-10}$	$0.29577712 \times 10^{+01}$
a_5	$0.17618975 \times 10^{-15}$	$0.43018319 \times 10^{+01}$
a_6	$0.61836632 \times 10^{+02}$	$0.29482418 \times 10^{+03}$
a_7	$0.29577712 \times 10^{+01}$	$0.37164915 \times 10^{+01}$

H ₂ O ₂		
Parameter	$200 \text{ K} \leq T < 1000 \text{ K}$	$1000 \text{ K} \leq T \leq 6000 \text{ K}$
a_1	$4.57329084 \times 10^{+00}$	$4.27613955 \times 10^{+00}$
a_2	$4.04990203 \times 10^{-03}$	$-5.43117137 \times 10^{-04}$
a_3	$-1.29482578 \times 10^{-06}$	$1.67344619 \times 10^{-05}$
a_4	$1.97287665 \times 10^{-10}$	$-2.15781233 \times 10^{-08}$
a_5	$-1.13406755 \times 10^{-14}$	$8.62495297 \times 10^{-12}$
a_6	$-1.80030753 \times 10^{+04}$	$-1.77025830 \times 10^{+04}$
a_7	$7.04524960 \times 10^{-01}$	$3.43494554 \times 10^{+00}$

Table A.4: Curve fit parameters for thermodynamic model of O, HO₂, and H₂O₂ (McBride et al., 1993).

Appendix B

Chemical Kinetics Mechanism for H₂/O₂ Combustion

Details of the chemical kinetics mechanism for H₂/O₂ combustion used in this work are shown in Table B.1 (Petersen and Hanson, 1999). The rate coefficients for reactions without pressure dependence take on the conventional Arrhenius form:

$$k(T) = AT^n \exp(-E/RT) \quad (\text{B.1})$$

All reactions are reversible. The reverse reaction rate is calculated from the forward rate (Eq. B.1) and the equilibrium constant.

Pressure-dependent reactions are modeled using the approach given by Kee et al. (1989):

$$k = k_{\infty} [P_r / (1 + P_r)] F \quad (\text{B.2})$$

where the reduced pressure, P_r , is

$$P_r = \frac{k_0[M]}{k_{\infty}} \quad (\text{B.3})$$

and the correction factor, F , is in the Troe (1979) form:

$$\ln F = \left\{ 1 + \frac{\ln P_r + c}{n - d(\ln P_r + c)} \right\}^{-1} \ln F_c \quad (\text{B.4})$$

The Troe centering parameter, F_c is given by

$$F_c = (1 - a) \exp(-T/T^{***}) + a \exp(-T/T^*) + \exp(-T^{**}/T) \quad (\text{B.5})$$

where the constants $c = -0.4 - 0.67 \ln F_c$, $n = -0.75 - 1.27 \ln F_c$, and $d = 0.14$.

Number	Reaction	Rate coefficient			Notes
		A	n	E	
1	O + H ₂ ⇌ H + OH	5.00 × 10 ⁶	2.70	6290	
2	H + O ₂ + M ⇌ HO ₂ + M	2.80 × 10 ¹⁸	-0.90	0	[a]
3	H + O ₂ + O ₂ ⇌ HO ₂ + O ₂	3.00 × 10 ²⁰	-1.70	0	
4	H + O ₂ + H ₂ O ⇌ HO ₂ + H ₂ O	9.38 × 10 ¹⁸	-0.80	0	
5	H + O ₂ + N ₂ ⇌ HO ₂ + N ₂	2.60 × 10 ¹⁹	-1.20	0	
6	H + O ₂ ⇌ O + OH	8.30 × 10 ¹³	0.00	14413	
7	H + HO ₂ ⇌ O ₂ + H ₂	2.80 × 10 ¹³	0.00	1068	
8	H + HO ₂ ⇌ OH + OH	1.34 × 10 ¹⁴	0.00	635	
9	H + H ₂ O ₂ ⇌ HO ₂ + H ₂	1.21 × 10 ⁷	2.00	5200	
10	OH + H ₂ ⇌ H ₂ O + H	2.16 × 10 ⁸	1.50	5200	
11	OH + OH + M ⇌ H ₂ O ₂ + M	7.40 × 10 ¹³ 2.30 × 10 ¹⁸	-0.40 -0.90	0 -1700	k _∞ [b,c] k ₀
12	OH + HO ₂ ⇌ O ₂ + H ₂ O	2.90 × 10 ¹³	0.00	-500	
13	OH + H ₂ O ₂ ⇌ HO ₂ + H ₂ O	1.75 × 10 ¹² 5.80 × 10 ¹⁴	0.00 0.00	320 9560	k _a [d] k _b [d]
14	HO ₂ + HO ₂ ⇌ O ₂ + H ₂ O ₂	1.30 × 10 ¹¹ 4.20 × 10 ¹⁴	0.00 0.00	-1630 12000	k _c [e] k _d [e]
15	O + O + M ⇌ O ₂ + M	1.20 × 10 ¹⁷	-1.00	0	[f]
16	O + H + M ⇌ OH + M	5.00 × 10 ¹⁷	-1.00	0	[a]
17	H + OH + M ⇌ H ₂ O + M	2.20 × 10 ²²	-2.00	0	[g]
18	H + H + M ⇌ H ₂ + M	1.00 × 10 ¹⁸	-1.00	0	[h]

^aM does not include O₂, H₂O, or N₂; all collision efficiencies = 1.0.

^bCollision efficiencies for M; H₂ = 2.0, H₂O = 6.0, all others = 1.0.

^cTroe parameters: $a = 0.7346$, $T^{***} = 94$, $T^* = 1756$, $T^{**} = 5182$.

^dRate coefficient is non-Arrhenius: $k_{13} = k_a + k_b$

^eRate coefficient is non-Arrhenius: $k_{14} = k_c + k_d$

^fCollision efficiencies for M; H₂ = 2.4, H₂O = 15.4, all others = 1.0.

^gCollision efficiencies for M; H₂ = 0.73, H₂O = 3.65, all others = 1.0.

^hCollision efficiencies for M; H₂ = 1.7, H₂O = 7.0, all others = 1.0.

Table B.1: Chemical kinetics mechanism for H₂/O₂ combustion, from Petersen and Hanson (1999). Species are N₂, O₂, H₂, H₂O, OH, H, O, HO₂, H₂O₂. All reactions are reversible. Except where noted, rate coefficients are computed via the Arrhenius expression: $k(T) = AT^n \exp(-E/RT)$. Units are in cal, mol, cm³, and s.

Bibliography

- Alpert, R. L. and T. Y. Toong (1972) "Periodicity in exothermic hypersonic flows about blunt projectiles." *Astronautica Acta* **17**:539–560.
- Ashford, S. A. and G. Emanuel (1994) "Wave angle for oblique detonation waves." *Shock Waves* **3**:327–329.
- Ashford, S. A. and G. Emanuel (1996) "Oblique detonation wave engine performance prediction." *Journal of Propulsion and Power* **12**(2):322–327.
- Bakos, R. J. and R. G. Morgan (1994) "Chemical recombination in an expansion tube." *AIAA Journal* **32**(6):1316–1319.
- Behrens, H., W. Struth, and F. Wecken (1965) "Studies of hypervelocity firings into mixtures of hydrogen with air or with oxygen." In *10th Symposium (International) on Combustion* (The Combustion Institute), pp. 245–252.
- Cambier, J.-L., H. G. Adelman, and G. P. Menees (1989) "Numerical simulations of oblique detonations in supersonic combustion chambers." *Journal of Propulsion and Power* **5**(4):482–491.
- Dabora, E. K., D. Desbordes, C. Gueraud, and H. G. Wagner (1991) "Oblique detonation at hypersonic velocities." *Progress in Astronautics and Aeronautics* **133**:187–201.
- Dabora, E. K., J. A. Nicholls, and R. B. Morrison (1965) "The influence of a compressible boundary on the propagation of gaseous detonations." In *10th Symposium (International) on Combustion* (The Combustion Institute), pp. 817–830.
- Dedebout, R., J. P. Sislian, and R. Oppitz (1998) "Numerical simulation of hypersonic shock-induced combustion ramjets." *Journal of Propulsion and Power* **14**(6):869–879.
- Fickett, W. and W. C. Davis (1979) *Detonation* (University of California Press), pp. 42–51.

- Figueira da Silva, L. F. and B. Deshaies (1998) "Numerical analysis of the self-ignition of hydrogen-air supersonic flows over a wedge." Paper presented at the 3rd Asian-Pacific International Symposium on Combustion and Energy Utilization.
- Gordon, S. and B. J. McBride (1976) "Computer program for calculation of complex chemical equilibrium compositions, rocket performance, incident and reflected shocks and chapman-jouguet detonations." Tech. Rep. SP-273, NASA.
- Grissimer, M. J. and J. M. Powers (1996) "Numerical predictions of oblique detonation stability boundaries." *Shock Waves* **6**:147–156.
- Gross, R. A. (1963) "Oblique detonation waves." *AIAA Journal* **1**(5):1225–1227.
- Gross, R. A. and W. Chinitz (1960) "A study of supersonic combustion." *Journal of the Aero/Space Sciences* **27**:517–524, 534.
- Grossman, B. and P. Cinnella (1990) "Flux-split algorithms for flows with non-equilibrium chemistry and vibrational relaxation." *Journal of Computational Physics* **88**:131–168.
- Hanson, R. K., J. M. Seitzman, and P. H. Paul (1990) "Laser-fluorescence imaging of combustion gases." *Applied Physics B* **50**:441–454.
- Herzberg, A., A. P. Bruckner, and D. W. Bogdanoff (1988) "Ram accelerator: A new chemical method for accelerating projectiles to ultrahigh velocities." *AIAA Journal* **26**:195–203.
- Higgins, A. J. and A. P. Bruckner (1996) "Experimental investigation of detonation initiation by hypervelocity blunt projectiles." Paper AIAA-96-0342 presented at the 34th AIAA Aerospace Sciences Meeting and Exhibit, Reno, NV, January 15–18.
- Jacobs, P. A. (1994) "Numerical simulation of transient hypervelocity flow in an expansion tube." *Computers in Fluids* **23**:77–101.
- Kamel, M. R., C. I. Morris, and R. K. Hanson (1997) "Simultaneous PLIF and schlieren imaging of hypersonic reactive flows around blunted cylinders." Paper AIAA-97-0913 at the 35th AIAA Aerospace Sciences Meeting and Exhibit, Reno, NV, January 6–9.
- Kaneshige, M. J. and J. E. Shepherd (1996) "Oblique detonation stabilized on a hypervelocity projectile." In *26th Symposium (International) on Combustion* (The Combustion Institute), pp. 3015–3022.

- Kee, R. J., F. M. Rupley, and J. A. Miller (1989) "Chemkin-II: A FORTRAN chemical kinetics package for the analysis of gas-phase chemical kinetics." Tech. Rep. SAND89-8009, Sandia National Laboratories.
- Larrouturou, B. (1991) "How to preserve the mass fractions positivity when computing compressible multi-component flows." *Journal of Computational Physics* **95**:59–84.
- Lasseigne, D. G. and M. Y. Hussaini (1993) "Interaction of disturbances with an oblique detonation wave attached to a wedge." *Physics of Fluids A* **5**(4):1047–1058.
- Lee, J. H. S. (1994) "On the initiation of detonation by a hypervelocity projectile." Paper presented at the Zeldovich Memorial Conference on Combustion, Voronovo, Russia, September 12–17.
- Lefebvre, M. H. and T. Fujiwara (1995) "Numerical modeling of combustion processes induced by a supersonic conical blunt body." *Combustion and Flame* **100**:85–93.
- Lehr, H. F. (1972) "Experiments in shock-induced combustion." *Astronautica Acta* **17**:589–597.
- Li, C., K. Kailasanath, and E. S. Oran (1993) "Effects of boundary layers on oblique-detonation structures." Paper AIAA 93-0450 presented at the 31st AIAA Aerospace Sciences Meeting and Exhibit, Reno, NV, January 11–14.
- Li, C., K. Kailasanath, and E. S. Oran (1994) "Detonation structures behind oblique shocks." *Physics of Fluids* **6**:1600–1611.
- Matsuo, A. and T. Fujiwara (1993a) "Numerical investigation of oscillatory instability in shock-induced combustion around a blunt body." *AIAA Journal* **31**(10):1835–1841.
- Matsuo, A. and T. Fujiwara (1993b) "Numerical investigation of standing oblique detonation supported by two-dimensional wedge." *Transactions of the Japan Society for Aeronautical and Space Sciences* **36**(111):47–56.
- McBride, B. J., S. Gordon, and M. A. Reno (1993) "Coefficients for calculating thermodynamic and transport properties of individual species." Tech. Rep. TM 4513, NASA.
- McVey, J. B. and T. Y. Toong (1971) "Mechanism of instabilities of exothermic hypersonic blunt-body flows." *Combustion Science and Technology* **3**:63–76.
- Mirels, H. (1963) "Test time in low-pressure shock tubes." *Physics of Fluids* **6**(9):1201–1214.

- Mirels, H. (1964) "Shock tube test time limitation due to turbulent-wall boundary layer." *AIAA Journal* 2(1):84–93.
- Mirels, H. (1966) "Flow nonuniformity in shock tubes operating at maximum test times." *Physics of Fluids* 9(10):1907–1912.
- Mitchell, R. E. and R. J. Kee (1982) "A general-purpose computer code for predicting chemical kinetic behavior behind incident and reflected shocks." Tech. Rep. SAND82-8205, Sandia National Laboratories.
- Montagné, J.-L., H. C. Yee, and M. Vinokur (1988) "Comparative study of high-resolution shock-capturing schemes for a real gas." *AIAA Journal* 27(10):1332–1346.
- Morris, C. I., M. R. Kamel, and R. K. Hanson (1998) "Shock-induced combustion in high-speed wedge flows." In *27th Symposium (International) on Combustion* (The Combustion Institute), pp. 2157–2164.
- Morris, C. I., M. R. Kamel, M. C. Thurber, S. D. Wehe, and R. K. Hanson (1995) "Development of an expansion tube for investigation of combustion in supersonic projectile flowfields." Presented at the 2nd International Workshop on Ram Accelerators, Seattle, WA, July 17–20.
- Oran, E. S. and J. P. Boris (1987) *Numerical Simulation of Reactive Flow* (Elsevier), pp. 131–133.
- Papalexandris, G. A. (2000) "A numerical study of wedge-induced detonations." *Combustion and Flame* 120:526–538.
- Paul, P. H. (1994) "A model for temperature-dependent collisional quenching of OH $A^2\Sigma^+$." *Journal of Quantitative Spectroscopy and Radiative Transfer* 51(3):511–524.
- Paull, A. and R. J. Stalker (1999) "Test flow disturbances in an expansion tube." *Journal of Fluid Mechanics* 245:493–521.
- Petersen, E. L. and R. K. Hanson (1999) "Reduced kinetics mechanisms for ram accelerator combustion." *Journal of Propulsion and Power* 15(4):591–600.
- Powers, J. M. (1994) "Oblique detonations: Theory and propulsion applications." In *Combustion in High-Speed Flows* (Kluwer Academic), pp. 345–371.
- Powers, J. M. and K. A. Gonthier (1992) "Reaction zone structure for strong, weak overdriven, and weak underdriven oblique detonations." *Physics of Fluids A* 4(9):2082–2089.

- Powers, J. M. and D. S. Stewart (1992) "Approximate solutions for oblique detonations in the hypersonic limit." *AIAA Journal* **30**(3):726–736.
- Pratt, D. T., J. W. Humphrey, and D. E. Glenn (1991) "Morphology of standing oblique detonation waves." *Journal of Propulsion and Power* **7**(5):837–845.
- Rubins, P. M. and R. P. Rhodes (1963) "Shock-induced combustion with oblique shocks: Comparison of experiment and kinetic calculations." *AIAA Journal* **1**(12):2778–2784.
- Ruegg, F. W. and W. W. Dorsey (1962) "A missile technique for the study of detonation waves." *Journal of Research of the National Bureau of Standards—C. Engineering and Instrumentation* **66C**(1):51–58.
- Shapiro, A. H. (1953) *The Dynamics and Thermodynamics of Compressible Fluid Flow* (John Wiley and Sons), vol. 1, pp. 529–592.
- Sharma, S. P. and G. J. Wilson (1995) "Test times in hypersonic shock tubes." Paper AIAA 95-0713 presented at the 33rd Aerospace Sciences Meeting and Exhibit, Reno, NV, January 9–12.
- Shepherd, J. E. (1994) "Detonation waves and propulsion." In *Combustion in High-Speed Flows* (Kluwer Academic), pp. 373–420.
- Siestrunck, R., J. Fabri, and E. Le Grivès (1953) "Some properties of stationary detonation waves." In *4th Symposium (International) on Combustion* (Williams and Wilkins: Baltimore), pp. 498–505.
- Srulijes, J., G. Smeets, G. Patz, and F. Seiler (1999) "An expansion-ludwig tube for accelerating combustible gas mixtures to superdetonative speeds." Paper reference under investigation.
- Srulijes, J., G. Smeets, and F. Seiler (1992) "Expansion tube experiments for the investigation of ram-accelerator-related combustion and gasdynamic problems." Paper AIAA-92-3246 presented at the 28th Joint Propulsion Conference and Exhibit, Nashville, TN, July 6–8.
- Sussman, M. (1994) *Numerical Simulation of Shock Induced Combustion*. Ph.D. thesis, Stanford University, Stanford, CA 94305.
- Trimpi, R. L. (1962) "A preliminary theoretical study of the expansion tube, a new device for producing high-enthalpy short-duration hypersonic gas flows." Tech. Rep. TR R-133, NASA.
- Troe, J. (1979) "Predictive possibilities of unimolecular rate theory." *Journal of Physical Chemistry* **83**(1):114–126.

- Vasiljev, A. A. (1994) "Initiation of gaseous detonation by a high-speed body." *Shock Waves* 3:321–326.
- Viguier, C., L. F. Figueira da Silva, D. Desbordes, and B. Deshaies (1996) "Onset of oblique detonation waves: Comparison between experimental and numerical results for hydrogen-air mixtures." In *26th Symposium (International) on Combustion* (The Combustion Institute), pp. 3023–3031.
- Viguier, C., C. Guerraud, and D. Desbordes (1994) "H₂-air and CH₄-air detonations and combustions behind oblique shock waves." In *25th Symposium (International) on Combustion* (The Combustion Institute), pp. 53–59.
- Viguier, C., C. Guerraud, and D. Desbordes (1997) "Study of critical conditions of onset of standing oblique detonation waves at hypersonic velocities in H₂-air mixtures." In *Proceedings of the 21st International Symposium on Shock Waves* (Panther Publishing and Printing), vol. 1, pp. 307–311.
- Vlasenko, V. and V. Sabelnikov (1994) "Numerical simulation of inviscid flows with hydrogen combustion after shock waves and in detonation waves." Paper AIAA 94-3177 presented at the 30th Joint Propulsion Conference and Exhibit, Indianapolis, IN, June 27–29.
- Wilson, G. and R. W. MacCormack (1992) "Modeling supersonic combustion using a fully implicit numerical method." *AIAA Journal* 30(4):1008–1015.
- Yee, H. C. (1989) "A class of high-resolution explicit and implicit shock-capturing methods." Tech. Rep. TM 101088, NASA.
- Yungster, S. and K. Radhakrishnan (1996) "A fully implicit time accurate method for hypersonic combustion: Application to shock-induced combustion instability." *Shock Waves* 5:293–303.